STUDY OF SPIN-DEPENDENT TRANSPORT PHENOMENA IN MAGNETIC TUNNELING SYSTEMS

AJEESH MAVOLIL SAHADEVAN

NATIONAL UNIVERSITY OF SINGAPORE

2012

STUDY OF SPIN-DEPENDENT TRANSPORT PHENOMENA IN MAGNETIC TUNNELING SYSTEMS

AJEESH MAVOLIL SAHADEVAN
(BSc. (Hons.), University of Delhi, India)

A THESIS SUBMITTED FOR THE DEGREE OF DOCTOR OF PHILOSOPHY

DEPARTMENT OF ELECTRICAL AND COMPUTER ENGINEERING

NATIONAL UNIVERSITY OF SINGAPORE

2012

ACKNOWLEDGEMENTS

I would like to take this opportunity to thank all my supervisors, colleagues and friends who made this work possible. First of all I thank my supervisors Prof. Charanjit Singh Bhatia and Dr. Hyunsoo Yang for their continuous support, guidance and encouragement. They gave me a topic that was very interesting physically and very relevant commercially. They always motivated me to work harder and smarter and I also thank them for entrusting me with several important responsibilities in our lab. They always kept their doors open to discuss experimental results. I am highly obliged for their trust in giving me an opportunity to work in their labs. My experience here has enlightened me both professionally and personally. Theoretical discussions with Asst. Prof. Mark Saeys have also been equally rewarding for my research and basic understanding of magnetic tunnel junctions.

I am extremely grateful to Dr. Gopi, Dr. Alan and Ravi Tiwari for collaborating with me in my research endeavors. Without the theoretical models developed by Dr. Alan and Ravi, the understanding and explanation of my experimental results would have been impossible. I also owe a lot to Kwon Jae Hyun for training me on the basics of thin film deposition and device fabrication. I would also like to thank my other colleagues with whom I had a number of interesting brainstorming sessions- Dr. Sankha, Dr. Xuepeng, Dr. Surya and Dr. Koashal. I was also fortunate to have senior members like Shin Young Jun and Dr. Samad, who encouraged and inspired me. I would also like to acknowledge the experimental support from Sagaran, Siddharth, Dr. Xuepeng, Ehsan, Li Ming, Dr. Zhang Jixuan and Mallikarjuna.

I am also very thankful to Information Storage Materials Laboratory and all its members especially- Fong Leong, Alaric Wong, Naganivetha, Sreenivasan, Megha, Goolaup, Debashish, Shikha and Shyamsunder Reghunathan for helping me out

whenever required. Both Ms. Loh and Alaric were always happy to answer my simple and sometimes silly queries.

Jung Yoon Yong Robert's role as both a lab manager and friend has been crucial for my PhD. His superlative efforts in setting up the Spin and Energy lab ensured that all our group members could work round the clock in a safe research environment. And finally I would like to thank all my friends in NUS and outside without whom the journey of PhD wouldn't have been as much fun as it was- Robert, Jae Hyun, Prashant, Rajesh, Abhishek, Sagaran, Siddharth, Sankha, Young Jun, Xuepeng, Ehsan, Taiebeh, Mojtaba, Aamir, Ayush, Ankit, Rathik, Ritika, Praveen, Karan, Li Ming, Aarthy, Reuben, Hari, Junjia, Xinming, Lu Hui, Nikita, Jaesung, Niu Jing, Sajid, Jia Wei, Baochen, Junjia, Mahdi, Xinming, Shimon, Baolei, Shreya, Shubham, Hidayat, Arkajit, Saurabh, Praveen, Amar, Rahul, Anil, Jerrin, Venkatesh, Deepika, Samanth, Xingui, Pengfei, Liu Bin, Ram, Pannir, Sujith, Lalita mam and many others.

Most importantly I would like to thank my parents and my brother for their blessings and support throughout the course of my PhD.

Finally, I would like to acknowledge the NUS research scholarship being provided by the Department of electrical and computer engineering, National University of Singapore. I would also like to acknowledge the financial support for this work by Singapore National Research Foundation under CRP Award No. NRF-CRP 4-2008-06, Singapore Ministry of Education Academic Research Fund Tier 2 (MOE2008-T2-1-105) and NUS grant # R-263-000-465-112.

ABSTRACT

The study of spin-dependent tunneling systems has stimulated both fundamental as well as commercial interest. For example, a magnetic granular system enables the study of interesting physics such as the coulomb blockade effect and higher order tunneling processes. Magnetic tunnel junctions (MTJ) are utilized for the high density storage hard disc drives and magnetoresistive random access memories. For the first part of the thesis, we have studied the magnetic field dependent hysteretic transport properties in magnetic granular Co/Al_2O_3 multilayers, experimentally and theoretically. The data show that the switching voltage can be significantly decreased with increasing the magnetic field. We also show changes in the magnetization of the Co granules with the electric fields. In the second part, we have investigated the effect of mechanical strain on MTJs using a diamond-like carbon film and magneto-capacitance in MTJs. The junction resistance as well as the tunnel magnetoresistance (TMR) reduces due to strain. Capacitance in MgO based MTJs is observed to be magnetic field dependent and the experimental results have been supported with fitting and a modified *RC* equivalent circuit.

SUMMARY

The Nobel Prize in Physics for 2007 was given to two scientists for their pioneering work in the field of data storage, which has created a new field of research called *spintronics* – controlling the spin degree of freedom in solid state systems – and also catalyzed substantial research activities across the globe. In this thesis we have studied the physics of magnetic tunneling systems, which form a part of spintronics systems in general. We started with understanding the fundamentals of spintronics device physics using the available literature and some basic experiments on anisotropic magnetoresistance (AMR) and giant magnetoresistance (GMR), which are the most basic spintronics systems. These systems are metal-based and spin-dependent scattering is the transport mechanism. However, magnetic tunneling systems (using oxide along with the ferromagnetic materials) are more interesting from a fundamental physics point of view as well as in terms of commercial applications because of its stronger effects. For example, tunneling magnetoresistance (TMR) is much higher in value than GMR and AMR since there are fewer conducting electrons but a greater percentage of these contribute to MR. This encouraged us to focus on spin-dependent tunneling phenomena as it holds greater promise both in hard disk drive (HDD) read sensors and magnetic random access memory (MRAM), as well as it being more challenging, both experimentally and theoretically.

The study of spin-dependent tunneling systems has stimulated considerable activities towards both fundamental as well as commercial interests. For example, a magnetic granular system enables the study of interesting physics such as the coulomb blockade effect and higher order tunneling processes. For the first part of the thesis, we have studied magnetic granular Co/Al_2O_3 multilayers. We investigated the effect of magnetic fields on electrical switching as well as the effect of electric fields on the

magnetic moment of this granular system. We successfully controlled the hysteretic switching characteristics using external magnetic fields experimentally. The data shows that the switching voltage can be significantly decreased with an increase in the magnetic field. We have developed a theoretical model based on carrier injection into the magnetic granules that qualitatively supports the magnetic field dependent I-V characteristics obtained experimentally. We also show changes in the magnetic moment of the Co granules with a high electric field. There are two effects of an external electric field on the magnetic granular system. One is the migration of oxygen from the oxide background into the granule that remains after the electric field is removed. The changes resulting from the oxidation of Co granules are irreversible and random in both magnitude and direction. Using theoretical calculations we have shown that depending on the number of O atoms residing in the Co granule, the magnetic moment can either increase or decrease. The other effect is the change in magnetic moment in the presence of an external electric field measured with an in-situ electric field in a SQUID. This change is both systematic and reproducible, and has been predicted in thin magnetic films as a result of changes in the 3*d* orbital occupation.

Another example of a spin-dependent tunneling system is the magnetic tunnel junction (MTJ) that has facilitated ultra-high density data storage in hard disk drives and also bolstered MRAM's claim to become the next generation ideal memory, also referred to as *storage class memory* (SCM). In the second part of the thesis, we looked at MTJs based on both Al_2O_3 and MgO tunnel barriers. The effect of substrate bias during sputter deposition of Al_2O-based MTJ layers has been studied. Though the bias improved the uniformity of the structure, the magnetic properties as well as the composition of alloy films were adversely affected. The incorporation of Ar into the tunnel barrier is another interesting observation. Optimization of the structure and the

process for the fabrication of MgO-based MTJs with TMR in excess of 250% at room temperature was also done. The MTJ devices were fabricated by a combination of Ar ion milling and the photolithography process. The TMR obtained was comparable to the maximum TMR reported by any other group in the world (for the same annealing conditions). We have investigated the effect of mechanical strain on MTJs using a diamond-like carbon film with high sp^3 content. The junction resistance and the tunnel magnetoresistance (TMR) were reduced under the effect of strain. Theoretical calculations also predicted the reduction of TMR as a result of biaxial strain on the Fe/MgO/Fe structure. The reason for the TMR reduction is the greater increase in the anti-parallel conduction as compared to the parallel state due to the appearance of hot spots close to the center of the Brillouin zone for the minority states of Fe. Finally we have studied capacitance and frequency dependent tunneling characteristics in MgO MTJs. Capacitance and *RC* time constant in MgO MTJs depends on the relative magnetization state of the FM electrodes. An equivalent circuit for the MTJs is also proposed that provides qualitative understanding of the measured capacitance values.

In summary, we have studied the device physics of spin-dependent tunneling systems in this work. In a Co/Al_2O_3 granular multilayer system, we have controlled electrical switching with the magnetic field, thus providing an important connection between spintronics and the resistive switching phenomena – a promising candidate for SCM. Electric field control of magnetization is another promising phenomenon for energy-efficient magnetic data storage that was observed in this system. In MTJs, we have shown the possibility of strain-induced reduction of the junction resistance in MgO-based MTJs, which is a requirement for high SNR in HDD read sensors along with sufficiently high MR. Substrate bias has been shown to be an interesting parameter to control the film and stack uniformity as well as the composition of the

MTJ layers. *RC* time constant – an important parameter for high speed applications in MTJs – has magnetic field dependence in MgO based MTJs.

Table of contents

Chapter 1 : Introduction and literature review 1

1.1 Introduction to memory and data storage 1

1.1.1 Storage-class memory (SCM) - an ideal memory 2

1.1.2 Magnetic memories for SCM 3

1.1.3 Beginning of data recording in magnetic systems 3

1.1.4 Current status- Fairly convincing statistics that HDDs are here to stay 4

1.1.5 Magnetic random access memory (MRAM) 5

1.2 Spintronics research and development 6

1.3 Introduction to spintronics physics – spin-dependent transport in ferromagnets (FM) 7

1.3.1 Two-current model 8

1.3.2 Discovery of Giant Magnetoresistance (GMR) 9

1.3.3 Rise of Magnetic Tunnel Junctions (MTJs) 10

1.4 Spin-dependent tunneling 12

1.4.1 Electron tunneling 12

1.4.2 Spin polarized tunneling (SPT) technique – beginning of SDT 13

1.4.3 Magnetic tunnel junctions 14

1.4.4 TMR- resistance v/s magnetic field 17

1.5 Recipe for giant TMR: crystalline barriers with coherent tunneling 17

1.5.1 Coherent tunneling v/s incoherent tunneling 17

1.5.2 Limitations and challenges 20

1.5.3 TMR over the years - MTJ experiments and barrier materials 21

1.6 Physics of TMR devices - Theoretical models to explain spin-dependent tunneling in MTJs 22

1.6.1 Julliere's model 22

1.6.2 Simmon's model 23

1.6.3 Slonczewski's model 24

1.7 Summarizing the major milestones in spintronics 25

1.8 Granular magnetic films 27

1.9 Resistive switching mechanism in magnetic systems 28

1.10 Organization of the thesis 29

1.11 Objectives 30

Chapter 2 : Experimental techniques 33

2.1 Thin film deposition processes 33

2.1.1 Magnetron sputtering 33

2.1.2 Radio frequency (RF) magnetron sputtering 34

2.1.3 Thermal evaporation 35

2.2 Structural and magnetic characterization techniques 36

2.2.1 Atomic force microscope (AFM) 36

2.2.2 Superconducting Quantum Interference Device (SQUID) 37

2.2.3 Alternating gradient force magnetometer (AGFM) 38

2.2.4 Transmission electron microscope (TEM) 39

2.3 Substrate preparation 41

2.3.1 Cleaning of the substrates 42

2.4 Device fabrication 42

2.4.1 Photolithography 42

2.4.2 Etching - Argon ion-miller 44

2.5 Electrical characterization 46

2.5.1 Four point probe measurement - probe station and He_4 based cryostat .. 46

Chapter 3 : Magnetic field control of hysteretic switching in Co/Al_2O_3 multilayers by carrier injection 49

3.1 Motivation 49

3.2 Introduction 49

3.3 Experimental methods 51

3.3.1 Film preparation 51

3.3.2 Transport properties:magnetic field dependent I-V characteristics 52

3.3.3 Effect of forming 54

3.4 Theoretical model 55

3.4.1 Model parameters and density of states (DOS) calculation 55

3.4.2 Magnetic field dependent I-V characteristics 58

3.5 Discussion 60

3.6 Conclusion 61

Chapter 4 : Electric field induced magnetization changes in Co/Al_2O_3 granular multilayers 62

4.1 Motivation 62

4.2 Introduction 63

4.3 Sample preparation 64

4.4 M-H loop measurement (SQUID) 65

4.5 Co granule oxidation state analysis using XPS 67

4.6 Theoretical model 70

4.7 Magnetic moment with in-situ electric field in SQUID 72

4.8 Conclusion 74

Chapter 5 : Effect of substrate bias on structural and compositional properties of AlO_x-based magnetic tunnel junctions 76

5.1 Motivation 76

5.2 Introduction 76

5.3 Deposition methods 78

5.4 Effect on roughness and deposition rate for different layers in MTJ structure… 78

5.5 Ge as an ultra-smooth buffer layer 79

5.6 MTJ deposited and characterization methods 80

5.6.1 TEM analysis: structures deposited with and without bias 81

5.6.2 TEM analysis: structures deposited with bias but different buffer layers….. 81

5.6.3 Switching characteristics of the multilayers using M-H loops from AGFM… 82

5.6.4 IrMn properties 83

5.6.5 AlO_x properties 84

5.7 Conclusions and suggestions 85

Chapter 6 : Fabrication strategies for magnetic tunnel junctions .. 86

6.1 Basics of MTJ fabrication 86

6.2 Fabrication strategies 87

6.2.1 Additive approach 87

6.2.2 Subtractive approach 89

6.2.3 GMR - experiments and results for spin valves 90

6.3 MTJ - experiments and TMR result 91

6.3.1 RF sputtered Al_2O_3 barrier using additive approach 92

6.3.2 Subtractive approach with MgO tunnel barrier in a new system 93

6.3.3 Underlayer roughness 93

6.4 TEM of MgO-based MTJs 94

6.5 Ion-milling process optimization for fabrication of MTJs 97

6.5.1 SIMS profile for MTJs 98

6.5.2 TMR in PSV and SV based MTJs 99

6.5.3 TMR in SAF-based MTJs 100

Chapter 7 : Biaxial strain effect of spin-dependent tunneling in MgO magnetic tunnel junctions 103

7.1 Motivation 103

7.2 Introduction 103

7.3 Experimental methods 106

7.4 DLC film properties 107

7.5 Effect of DLC film on measured TMR and its voltage and temperature dependence 108

7.6 Theoretical methods 113

7.7 Effect of strain on the calculated TMR of Fe/MgO/Fe 115

7.7.1 Transmission spectra for strained and unstrained Fe/MgO/Fe 118

7.8 Conclusions 121

Chapter 8 : Parallel-leaky capacitance equivalent circuit model for MgO based magnetic tunnel junctions 123

8.1 Motivation 123

8.2 Introduction 124

8.3 Experimental methods 125

8.4 Negative TMC in MTJs 126

8.5 Equivalent RC circuit for MTJs 128

8.6 Impedance spectroscopy 129

8.7 Frequency and bias dependence of TMR 132

Chapter 9 : Conclusions and recommendations for future work . 135

List of publications, conferences and awards……..138

References

Appendix

A. Theoretical calculation method

B. List of symbols, abbreviations and acronyms

List of figures

Figure 1.1 HDD areal density over the years and a comparison with optical disc technology 4

Figure 1.2 MRAM combines the best characteristics of DRAM, SRAM and Flash RAM 5

Figure 1.3 Historic postcard: Gerlach's postcard dated 8 February 1922 to Neils Bohr. It shows a photograph of the splitting of the e-beam with the message (translated): "Attached is the experimental proof of directional quantization. We congratulate you on the confirmation of your theory." ... 7

Figure 1.4 Spin-dependent resistivity for electrons in an FM. 8

Figure 1.5 Two-current model for GMR trilayer structure. 9

Figure 1.6 Practical importance of the discovery of GMR. 10

Figure 1.7 Tunneling in MIM structures (a) Electron wave function decays exponentially in the barrier region and non-zero transmission for thin barriers (b) Potential diagram for an M/I/M structure with applied bias eV. Blue region represents filled states, open areas are empty states, and the red region represents the forbidden gap in the insulator. 13

Figure 1.8 Schematic illustration of tunneling process: (a) and (b) show the density of states for parallel and anti-parallel magnetization configuration of an MTJ. 15

Figure 1.9 The figures displayed above help in differentiating the structural differences between amorphous and crystalline barriers both schematically and using cross-sectional TEM images. 20

Figure 1.10 A schematic summary of the work done in this dissertation. Theoretical calculations have also been performed to support the experimental results. 31

Figure 2.1 Schematic of magnetron sputtering. 34

Figure 2.2 Two AJA sputter systems used in this study. 35

Figure 2.3 (a) Digital instruments SPM (b) Schematic of an AFM. 37

Figure 2.4 (a) Quantum Design MPMS (b) Meissner effect in a superconducting ring cooled in an externally applied magnetic field and (c) dual junction DC SQUID loop. 38

Figure 2.5 Schematic diagram of an AGFM. 39

Figure 2.6 A schematic representation of TEM column. 41

Figure 2.7 Karl Suss MA6 with 350 nm UV lamp. 43

Figure 2.8 Lift-off process in detail (a) Exposure of UV light for patterning. (b) UV interaction with the resist. (c) Developing process. (d) Ion-milling for cleaning interface. (e) Metal deposition. (f) Lift-off process. The unexposed resist with the metal on top of it is removed inside acetone and/or PG remover. 44

Figure 2.9 (a) Schematic of ion-milling and (b) Intlvac ion miller 45

Figure 2.10 Lithography steps with negative resist. (a) The film coated with negative resist is exposed with the desired patterns by MA6. (b) UV beam interaction with the resist. (c) Developing the exposed patterns. (d) Ion milling process to remove the metal area not covered by resist. (e) Removal of resist in acetone or negative resist remover. 46

Figure 2.11. Equivalent circuit for (a) two-probe measurement (b) four-probe measurement. A GMR device measured using (c) two-probe (d) four-probe configuration. 47

Figure 2.12 (a) Probe station for instant TMR and I-V measurements. (b) He_4 cryostat for low temperature and high vacuum transport measurements..... 48

Figure 3.1 (a) A three-dimensional schematic of the Co/Al_2O_3 multilayer system. (b) Cross-sectional transmission electron microscope (TEM) image of Co/Al_2O_3 multilayers. The dark spots are Co islands and the white region is an Al_2O_3 insulating matrix..... 52

Figure 3.2 (a) *I-V* characteristics of the device during the forming process. (b) Threshold resistive switching behavior due to charge accumulation in the granules. 53

Figure 3.3 (a) Experimental *I-V* characteristics of threshold switching for different external magnetic fields. (b) The conductance ranges at 0.25 V, determined by connecting two conductance data which were obtained from the forward and backward bias sweeps. (c) This shows how the switching voltage (V_t) changes with the external magnetic fields. 54

Figure 3.4 TEM images of the granular structure (a) before and (b) after forming. The structure was affected by the high voltage bias application. C-AFM images (c) and (d) after forming indicates transition to a conducting state after high voltage application. The contact pad positions are indicated by Au. 55

Figure 3.5 Density of states (DOS) with different values of external magnetic field (H), for both uncharged and charged conditions at $H = 0$ (a), $H = 0.1H_s$ (b), and $H = H_s$ (c). The Fermi level was at 0 eV. The valence band was completely filled for all cases. After charging, the center of the conduction band

moved closer to the fermi level. The occupation of the conduction band depended on the magnetic field. At $H = H_s$ the conduction band was partially filled. 57

Figure 3.6 Calculated *I-V* characteristics of the RS system for different *H*. At a fixed magnetic field the system changes from a HRS to LRS when the voltage was swept from 0 to 1.5 V. 59

Figure 3.7 I-V characteristics of a NiO/Co granular multilayer system at different magnetic fields. At higher magnetic fields, the switching voltage could be reduced in this system as well. 61

Figure 4.1 (a) Cross-sectional TEM image of the Co/Al_2O_3 multilayer system (as deposited). The dark spots are Co islands and the lighter region is the Al_2O_3 insulating matrix. A schematic representation of the multilayer system is shown in the inset. (b) TEM of the multilayers after applying a high electric field along the plane of the film. 65

Figure 4.2 M-H loops using SQUID showing the changes in magnetization for different samples before and after application of electric field. (a) Net magnetic moment for the sample increased after bias application. (b) Net magnetic moment for the sample decreased after bias application. In (c) and (d), samples were divided into four regions and the M-H loop was measured after an electric field was applied to each region. The net magnetic moment of the samples fluctuated as the different regions were formed. The inset in (d) shows a reliability test of SQUID by repeating the measurement of the same sample for four times at zero bias. Note that the sample #1 had a smaller size than others. 67

Figure 4.3 (a) XPS depth profiles of the multilayer system showing alternating oscillation peaks of Co_{2p} and O_{1s}. (b) O_{1s} spectra of the layers at the first Co layer from as-deposited sample. (c) Region with enhanced magnetization. (d) Region with reduced magnetization. The inset in (b) shows a Co granule with 2 O atoms used in the calculations. Co atoms are blue and O atoms are red. 69

Figure 4.4 Magnetic moment versus applied electric field for two samples. The magnetic moment gradually reduces as the electric field increases, and the changes are reproducible (1^{st} to 4^{th} steps indicate the sequence of measurements). The contact pads are indicated in the insets. 74

Figure 5.1 (a) AFM image of Ge on SiO_2 (RMS roughness 0.3 nm) and (b) XPS data showing the characteristic Ge peak with that of Ge oxide. 80

Figure 5.2 (a) Cross-sectional TEM image for MTJ [Ge (buffer) /IrMn/Co/AlO_x/Co/NiFe/Cu/Ge] without substrate bias. (b). Cross-sectional TEM image for MTJ with substrate bias..... 81

Figure 5.3 (a) Cross-sectional TEM image for MTJ [Ge (buffer) /IrMn/Co/AlO_x/Co/NiFe/Cu/Ge] with substrate bias. (b). Cross-sectional TEM image for MTJ [Cr/Au/Cu (buffer) /IrMn/Co/AlO_x/Co/NiFe /Cu/Ge] with substrate bias 82

Figure 5.4 (a) AGFM M-H loops for the entire MTJ film structure when no bias is applied to any of the layers during deposition, (b) when bias is applied to each of the layers during deposition and (c) when bias is applied to all layers except IrMn. 82

Figure 5.5 (a) RBS data for IrMn with and without substrate bias. (b) XRD signal for IrMn with and without substrate bias. Peaks broaden with bias. 83

Figure 5.6 (a) AGFM signal showing a clear exchange bias (150 Oe) for IrMn/Co films when IrMn was deposited without bias. (b) AGFM signal showing loss of exchange bias in IrMn/Co structure when IrMn was deposited with substrate bias. 84

Figure 5.7 (a) RBS signal for AlO_x without substrate bias. (b) RBS signal for AlO_x with substrate bias. No difference except higher Ar concentration. 84

Figure 6.1 Schematic illustration of the steps involved in MTJ fabrication using additive approach (four-step lithography) 88

Figure 6.2 Schematic illustration of the additive steps (a, c) leading to sidewall shorting (d). Using a bi-layer resist (b) can be of some help though not the best choice. 89

Figure 6.3 Schematic illustration of the different stages during the fabrication of MTJ device using the subtractive approach. 90

Figure 6.4 (a) GMR structure used for current in-plane (CIP) measurement (b) GMR signal from the device 91

Figure 6.5 (a) MTJ structure used in CPP configuration (b) maximum MR of 2.6% obtained using Al_2O_3 tunnel barrier 92

Figure 6.6 (a) RMS roughness of Ta layer deposited at 60 W dc power, inset shows the AFM image. (b) Optimization of MgO deposition pressure for minimum roughness. 94

Figure 6.7 Cross-sectional TEM micrographs of MTJ structures with different IrMn configurations (a) bottom and (b) top 95

Figure 6.8 TEM images illustrating MTJ structures deposited with different underlayers (a) Ta and (b) Ta/Ru/Ta 96

Figure 6.9 TEM images showing (a) Ta/IrMn interface with Ta providing a template for good IrMn texture (b) a good IrMn surface texture ensures the growth of CoFe and MgO with (001) orientation. 96

Figure 6.10 TEM images for the MTJ structures with (a) optimized IrMn conditions providing flatter interfaces and (b) good MgO (001) texture. 97

Figure 6.11 SIMS signal for an MTJ stack – Ru/Ta/CoFe/MgO/CoFe/IrMn/Ta/Sub – showing strong peaks of the Ru cap layer, the MgO tunnel barrier and the IrMn antiferromagnet layer used for etch stop. 99

Figure 6.12 TMR loop data for (a) pseudo-spin valve MTJ with 262% TMR (b) exchange biased MTJ with 71% TMR– each with a 2 nm MgO tunnel barrier. 100

Figure 6.13 (a) MR curve for one of the MTJs (73 μm^2) at 4 K (b) temperature dependence (c) Plot of TMR versus RA product where each point corresponds to one device. 101

Figure 6.14 TMR ratio achieved by our group over the past three years. 101

Figure 7.1 DLC films used in the CMOS research. Using DLC film there is enhancement in the transconductance of the p-channel FET. 104

Figure 7.2 (a) Schematic of the device configuration with a DLC layer over the junction area. (b) A scanning electron microscope (SEM) image with a DLC film over the tunnel junction. The top electrode width was 80 μm while the DLC strip had a width of 150 μm. 107

Figure 7.3 XPS spectra of the C_{1s} core level for the DLC film indicating a very high relative sp^3 proportion (65%) of the film. 108

Figure 7.4 A plot of TMR versus junction area for the MTJs showing a reduction in the TMR of devices after the deposition of the DLC film below the junction area of 500 μm^2. 109

Figure 7.5 The loop curve for a device with the junction area of 73 μm^2 before and after DLC deposition at 300 K and 6 K..... 110

Figure 7.6 TRIM data for carbon penetration in Cu electrodes – maximum penetration depth 5 nm with a peak at 1 nm..... 111

Figure 7.7 Bias voltage dependence of resistance in the parallel and anti-parallel states with TMR, for an MTJ before (a) and after (b) DLC deposition at 300 K. Temperature dependence of resistance in the parallel and anti-parallel states as well as TMR before (c) and after (d) DLC deposition for a device with the junction area of 73 μm^2. 112

Figure 7.8 Central structure used to model the junction for six layers of MgO. The blue, green, and red circles correspond to Fe, Mg, and O atoms, respectively. In the calculations, both Fe(100) contacts extend to infinity. The x, y, and z directions are indicated. 114

Figure 7.9 Benchmarking the calculation method by comparing with (a) one of the first results in the Fe/MgO/Fe structure (b) Very recent calculations using a similar approach (c) Our calculation results..... 115

Figure 7.10 (a) Calculated conductance for a Fe(100)/MgO/Fe(100) tunneling junction as a function of the number of MgO layers. The conductance is shown for the parallel and the anti-parallel configurations for both the unstrained and the 5% biaxial *xz*-strain cases. The relative increase in the conductance after applying 5% biaxial *xz*-strain is also shown to facilitate comparison with the experimental data in Figure 7.7. For six MgO layers, the parallel

conductance increases by a factor 1.74 from 0.65 to 1.14 nS, while the anti-parallel conductance increases by a factor 22.32 from 7 to 157 pS. (b) Optimistic TMR ratio [$(G_P-G_{AP})/G_{AP}$, where G_P and G_{AP} are the conductance of the parallel and the anti-parallel states, respectively] for the unstrained and the strained tunneling junctions as a function of the MgO thickness. To facilitate comparison with the experiments, the relative change in the TMR ratio is also shown and ranges from a factor of 7 to 27. 117

Figure 7.11 TMR and factor change in TMR for unstrained (0% strain) and different levels of strain in Fe/MgO/Fe with 6-layer MgO. For 3.5% strain, the relative change in TMR (right-axis) matches the experimental change in TMR. 118

Figure 7.12 $k_{//}$-resolved transmission spectra for the various transport modes for a Fe(100)/MgO(6 layers)/Fe(100) junction. Biaxial strain decreases the lattice in the *x* and *z* directions by 3.5%, and expands the lattice in *y* direction by 1.6%. Transport for the majority channels is dominated by states near the gamma point, while states near the edge of the Brillouin zone dominate for the minority channels. Strain introduces transmission hot-spots near the k_y= 0 axis for the minority and the anti-parallel transmission spectra. Note the different scales for the various transmission spectra. 119

Figure 7.13 Effect of 3.5% biaxial *xz*-strain on the Fe(100) surface spectral density (number of states/eV/Å^2) at the Fermi energy for the minority and the majority states. While changes for the majority states are relatively minor, the minority states at (k_x, k_y)=(±0.4, 0.0) clearly moved closer to the

gamma point. As explained in the text, this is consistent with a broadening of the minority band and a decrease in the spin polarization. 120

Figure 8.1 (a) The magnetic field dependence of resistance and capacitance of an MTJ with the junction area of ~70 μm^2. The TMR is 116%, while the TMC is 17% at 1 MHz. The TMR ratio is defined by $(R_{AP}-R_P)/R_P$, where R_P and R_{AP} are the junction resistance in the P and AP alignment, respectively. The TMC ratio is defined by $(C_P-C_{AP})/C_{AP}$, where C_P and C_{AP} are the junction capacitance in the P and AP alignment, respectively. (b) The magnetic field dependence of the *RC* time constant for the same device with a relative difference of 83% between the P and AP states. (c) The dependence of TM_{RC} on the TMR shows greater asymmetry in *RC* time constant for higher TMR devices. The equivalent circuit for the MTJ with a parallel leaky capacitor across the series combination of C_g and C_i is also shown in the inset. (d) The relationship between the capacitance and the TMR of the junctions. All data are from room temperature measurements. 127

Figure 8.2 Cole-Cole plots for low and high TMR junctions (10 kHz to 2 MHz). For the high TMR (300%) junction with the junction area of ~70 μm^2 in (a) and (b), the semi-circular fits match well with the data, while for the low TMR (8%) junction with the junction area of ~70 μm^2, the data significantly deviates from semicircular fits in (c) and (d). All data are at 20 K. 130

Figure 8.3 The ΔX (Ω) values for the high TMR (300%) and the low TMR (8%) junctions are shown in (a) and (b), respectively. ΔR (Ω) is shown in the insets. For both the junctions, the fitting parameters are close to the

experimental values as shown in (c) and (d) below the corresponding figures. All data are at 20 K. 132

Figure 8.4 Frequency dependence of TMR for high TMR junctions (a) and a low TMR device (b). Normalized bias dependence of both TMC and TMR for the high TMR (300%) device (c) and the low TMR (8%) device (d) at 20 K. 133

List of tables

Table 1.1 Target specifications of future universal memory 2

Table 4.1 Magnetic moment (μ_B) of a cobalt granule for different number of oxygen impurities. 72

Table 5.1 RMS roughness and deposition rates for different materials with and without substrate bias application during the deposition 79

Chapter 1 : Introduction and literature review

1.1 Introduction to memory and data storage

Memory is a medium that enables the retention of information. Ever since the inception of human civilization, information sharing has been a key aspect of the development of the society. Man started looking for alternative approaches when he found the human brain to be inept for the task of information storage. We have come a long way from using huge bars of clay, paper and punch cards to storing information in a few atoms of magnetic materials.[1]

The electronics industry is composed of three main functions – computation (logic and memory), data storage and communication.[2] A very high density and high performance memory is imperative to enable power-efficient computing devices to work. In order to achieve a reasonable level of cost and performance, most of the computing systems today use a complex hierarchy of semiconductor-based memory (for computation and logic applications) and magnetic material-based systems (for data storage applications). Magnetic hard disk drives (HDD) provide the cheapest available memories for non-archival data storage with 10-100 times lower cost per bit compared to solid state memories. HDDs include a read/write head that moves over a rotating magnetic media. The low cost of HDDs, however, is counterbalanced with lower levels of reliability as devices with moving parts are prone to mechanical failures resulting in complete data loss. Flash – with a better performance and reliability than HDDs – is the cheapest solid state memory and has already created a niche market for itself and is displacing HDDs, mainly in compact hand-held electronics such as music players, mobile phones, ipod, ipad, etc. A flash memory element consists of a thin layer of polysilicon in the gate dielectric of a transistor that is isolated from the control gate as

well as the transistor channel. Still, even flash memory is not an ideal memory, and is prone to endurance issues that are inherent in devices using high electric fields. The high voltage applied to the polysilicon gradually degrades it, resulting in data loss after approximately 10^5 to 10^6 write cycles. Flash is also a slow memory with data access times of the order of a few μs.[3] Hence, there is a persistent quest for an ideal memory that blurs the gap between memory (fast, solid state) and storage (high density, non-volatile, low cost).

1.1.1 Storage-class memory (SCM) - an ideal memory

SCM combines the benefits of a solid-state memory, such as high performance and robustness, with the archival capabilities and low cost of conventional hard-disk magnetic storage [Table 1.1]. The goal is to develop a solid state memory with a better performance than flash in terms of non-volatility, cost, speed and endurance as well as a storage density that is superior to HDDs.

Parameter	Ideal value
Access time	50–1,000 ns
Data rate	100 MB/s
Endurance (cycles)	10^9–10^{12}
Hard error rate (bits/terabyte)	10^{-4}
Mean time between failures	2×10^6 hours
Data retention	10 years
On power	100 mW
Standby power	1 mW
Cost	<<$5/GB
Annual compound growth rate	35%

Table 1.1 Target specifications of future universal memory.[4]

1.1.2 Magnetic memories for SCM

In order to develop any memory system there are some basic requirements. With ferromagnetic (FM) materials, detection of the signal is possible sensing either fringe fields as in HDDs or spin polarized itinerant electrons as in magnetoresistance-based devices. This signal is converted to a voltage or current using a detector FM similar to an optical analyzer for polarized light. The source for this signal can either be an external magnetic field or a spin polarized electric current (which will be discussed later). There are several inherent benefits of using magnetic materials for memory such as non-volatility, fast switching speed, low energy switching, long endurance, high durability, abundant and common metallic materials, and radiation insensitivity, along with some process-related advantages such as scalability and standard fabrication approaches. Still, there exist some limitations using magnetic materials since they have no power gain and also some challenges related to integration with the conventional CMOS process.[3] In the next section we give an account of some of the data storage approaches using magnetic materials.

1.1.3 Beginning of data recording in magnetic systems

Non-volatility is an indispensable requirement for any memory technology and is intrinsic to the natural bistability of magnetic materials. Magnetic materials were first used for storage in 1878 for audio recording by Oberlin Smith.[5] Vladimir Poulsen was acknowledged with the first public demonstration of a device for recording a signal on a wire wrapped around a drum. The first magnetic tape, made up of metal strips on paper, was patented by Fritz Pfleumer. Progress in magnetic recording was slow and it was not until 1932 that the first magnetic recording devices were commercialized. Most of the initial developments in magnetic recording were for

audio applications but by 1940s, video recording also gained momentum. In the early 1950s floppy disks (IBM) and hard disk drives (HDD) became prominent in the memory market. Today, HDDs have a huge market in both desktop and laptop personal computers with the primary competitive advantage being the low cost per bit. The areal density of HDDs over the past few decades is shown in Figure 1.1.

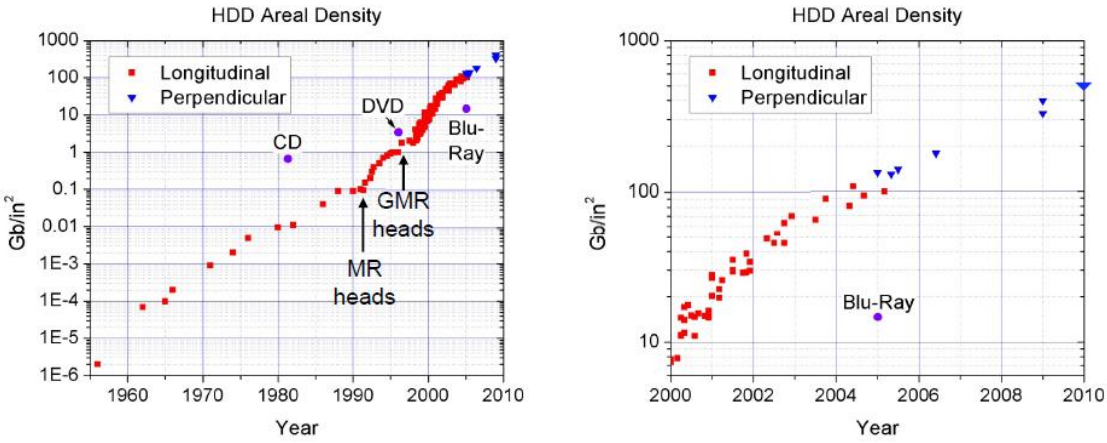

Figure 1.1 HDD areal density over the years and a comparison with optical disc technology.[6]

1.1.4 Current status- Fairly convincing statistics that HDDs are here to stay

The popular perception is that solid state drives (SSDs based on NAND) are ready to replace HDDs in the laptop market. However, a recent statistical analysis by Seagate reveals that HDDs are far from being obsolete. NAND flash memory has a stronghold for consumer devices such as SD cards, tablets and smart phones but only 7% of it is being used in the solid state drives.[7] With increasing memory demand for laptop PCs, NAND memory is nowhere close to posing a threat to HDDs. Even if we assume that all the NAND were to be used for solid state drives, only 4% of the market demand would be met. Hard disk drives will continue to serve the bulk of the data storage requirements for the laptop market for years to come. Magnetic random access memory (MRAM), another technology based on magnetic materials, is one of the

frontrunners to replace dynamic random access memory (DRAM) and non-volatile flash memory.[7]

1.1.5 Magnetoresistive random access memory (MRAM)

Despite the performance and reliability related limitations (in HDDs), magnetic memory is still the primary choice for the long-term storage of information with technologies such as hard drives and tape drives that have been around for over 50 years. In the 1970s static and dynamic RAMs based on thin film semiconductor materials were introduced and immediately they overtook the magnetic technologies, by virtue of their better performance in terms of speed, costs and miniaturization.[2]

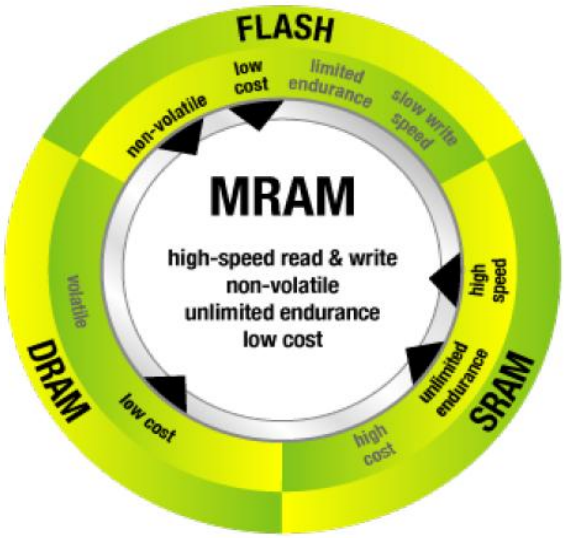

Figure 1.2 MRAM combines the best characteristics of DRAM, SRAM and Flash RAM.[8]

MRAM is the SCM candidate representing magnetic materials with its speed comparable to SRAM (static RAM), a density close to DRAM density per transistor, and the non-volatility of flash, schematically shown in Figure 1.2.[9] The concept of MRAM was proposed after the discovery of giant magnetoresistance (GMR)-based

spin valves in 1988, as competition to semiconductor memory. At the same time MTJs with high TMR were also realized. The combination of huge investments and the discovery of MR-based spin valve technologies catalyzed an intense research effort in MRAM development. The basic memory element or bit in an MRAM is a magnetic tunnel junction (MTJ). The first commercial MRAM was introduced by Freescale Semiconductor in 2006 and since then many other major semiconductor companies such as Samsung, Toshiba, TSMC, Micron, etc. have also ventured into the MRAM business.[2] The initial MRAM technologies were based on magnetic field switching of magnetization and suffered from limitations such as scalability and reliability. Spin-transfer torque switching based MRAM (STT-RAM) is the answer to these issues; however, there still exist concerns related to high switching current and low thermal stability, which researchers are trying to overcome. All the above developments have created a new direction in physics called spintronics, wherein the spin degree of freedom of the electrons is manipulated in materials and devices. The fundamental physics of electron transport in ferromagnetic (FM) materials and spintronics devices will be discussed in detail in the following sections.

1.2 Spintronics research and development

Although magnetism is very old, spintronics is relatively new. Quantum mechanics laid the foundation for spintronics with the pioneering experiment carried out by Stern and Gerlach in 1921 about a century ago [Figure 1.3].[10] This discovery proved the quantization of spin angular momentum and the discoverers were awarded the Nobel Prize in physics (1943) for their contribution. A decade later in 1936, Sir Nevill Mott's proposal of a two-current model was instrumental in understanding the significance of the electron's spin in controlling the transport properties, especially in

transition metals and alloys. The following sections will provide in detail the physics of these discoveries as well as the implications in revolutionizing the data storage market and fundamental research in nanotechnology.[2]

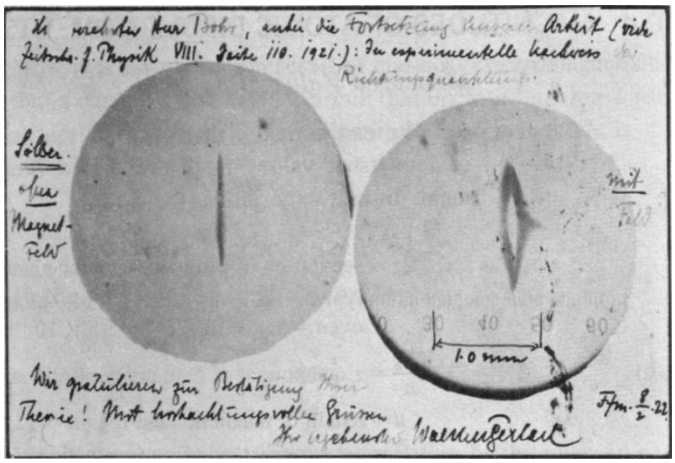

Figure 1.3 Historic postcard: Gerlach's postcard dated 8 February 1922 to Neils Bohr. It shows a photograph of the splitting of the e-beam with the message (translated): "Attached is the experimental proof of directional quantization. We congratulate you on the confirmation of your theory."[10]

1.3 Introduction to spintronics physics – spin-dependent transport in ferromagnets (FM)

The foundation of spintronics is based on the influence of the spin of an electron on its transport properties in FM metals. With the band structure of the FM in mind, it becomes very easy to understand the spin dependence of the electrical current through the FM. The majority and minority bands split at the Fermi level [Figure 1.4 (a)], resulting in asymmetric contributions to the total electrical current generally referred to as the spin polarized current. A model based on this was proposed by Mott in 1936 and is known as the two-current model, which forms the basis of spintronics today. The model considers the mixing of spins by exchange of electrons between the two channels, though a simplified version of this model is more popular which considers two independent channels for the two spins and overlooks any spin mixing.

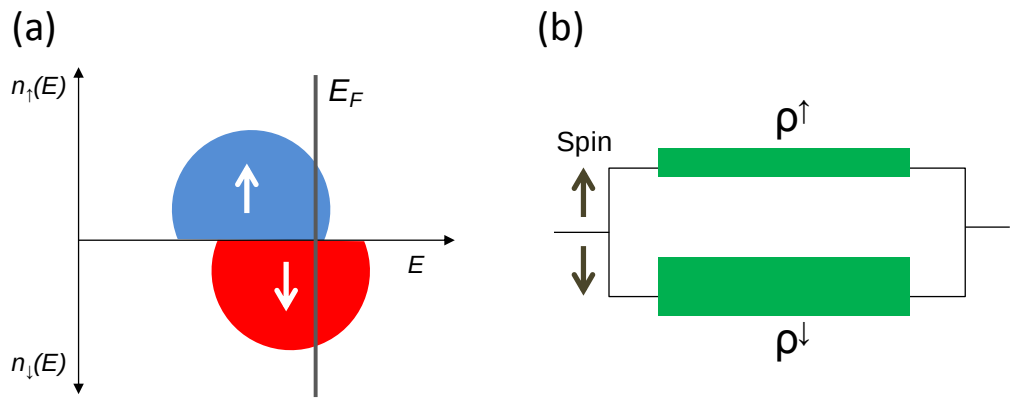

Figure 1.4 Spin-dependent resistivity for electrons in an FM.

1.3.1 Two-current model

Mott and Jones proposed a theory explaining that in simple ferromagnetic transition metals (TM) such as Fe, Co, and Ni, the current is carried by spin-polarized electrons because of a significant spin-dependent scattering of the majority ('up') and minority ('down') spin-polarized electrons. For these elemental FMs, the difference arises due to the spontaneous splitting of the d-bands at the Fermi level, leading to a differential density of states (DOS) for the two spins. The energy required for this spontaneous magnetization is provided by the "Weiss field", as explained by the Stoner's criteria for ferromagnetism in Fe, Co and Ni.[2]

Many of the magnetotransport properties of these elements and their alloys can be understood with the help of a 'two-current' model in which the electrical current is comprised of two independent channels of spin-up and spin-down [Figure 1.4(b)].[11] However, it took more than half a century (Fert and Gruenberg, 1988), before it was acknowledged that these currents can be manipulated in inhomogeneous magnetic systems comprising magnetic and nonmagnetic regions so as to modify the flow of current in these systems and thereby their resistance as shown in the schematic in Figure 1.5.

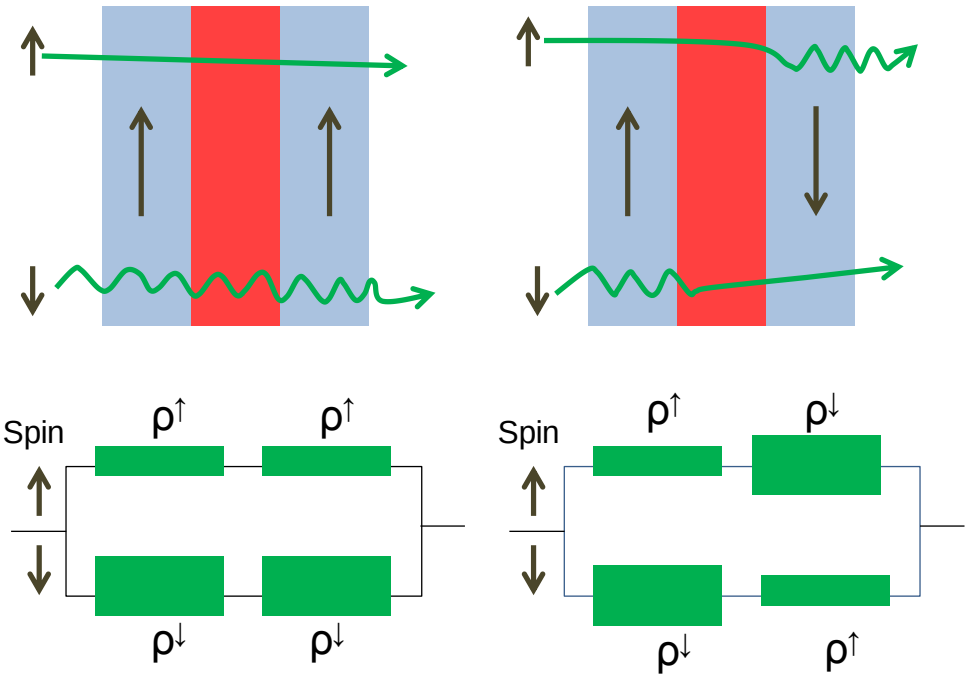

Figure 1.5 Two-current model for GMR trilayer structure.

1.3.2 Discovery of Giant Magnetoresistance (GMR)

Around 20 years before its discovery, Albert Fert had already conceived the idea of GMR using FM metals doped with different metallic impurities based on spin-dependent scattering by the impurities and two-current model.[12] The only roadblock that delayed the realization was the absence of technology to fabricate multilayer films with thickness of the order of electron mean free path (few nanometers).

In the 1980s, with breakthrough developments in ultra high vacuum thin film deposition technologies such as molecular beam epitaxy (MBE), it became possible to deposit multilayers of ultra-thin magnetic films and realize the idea of a magnetic switch – GMR. Along with the initial experiments by Fert's group using transition metal doped FMs, Brillouin scattering experiments conducted by Grünberg and co-workers revealing the presence of anti-ferromagnetic coupling in Fe/Cr multilayers were equally crucial, enabling P and AP states in adjacent FM layers separated by

NMs.[13] Finally, both groups independently demonstrated the concept of GMR in Fe/Cr/Fe trilayers as well as Fe/Cr multilayers – the explanation of which was based on the spin-dependent scattering mechanism described by Fert. It was also observed later that the scattering at the FM/NM interfaces are spin-dependent and the contribution of bulk and interfaces can be separated.[14] They were awarded the Nobel Prize in physics (2007) for the discovery of GMR as the GMR based devices are considered revolutionary both in the field of spintronics (for combining the two most fundamental properties of electrons – charge and spin) and nanotechnology (for being the first application of nano-science in a widely used commercial product [Figure 1.6]).

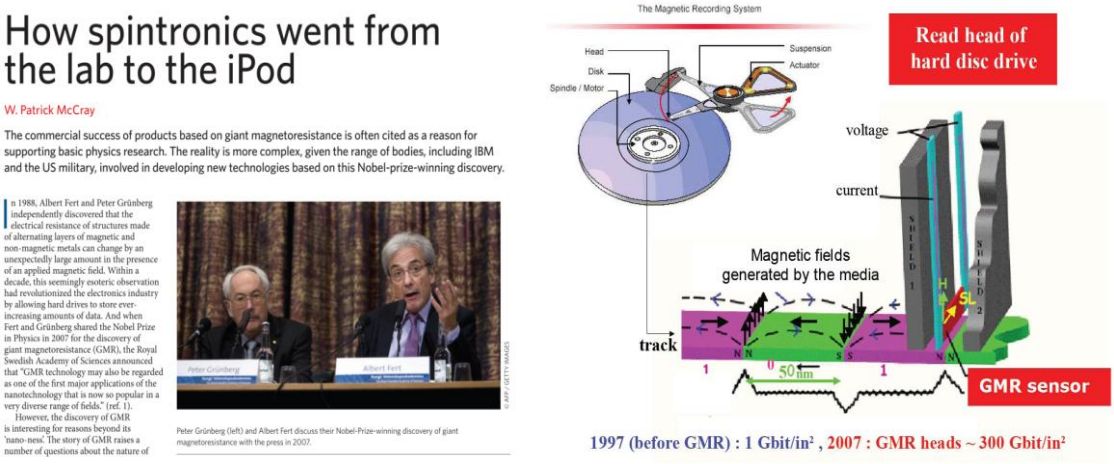

Figure 1.6 Practical importance of the discovery of GMR.[15, 16]

1.3.3 Rise of Magnetic Tunnel Junctions (MTJs)

In the past two decades since the discovery of GMR and oscillatory interlayer coupling in transition metal systems, the magnitude of the GMR signal exhibited by spin-valve structures has changed very little. The resistance of such structures is typically about 10–15% higher when the sensing and reference magnetic moments are anti-parallel (AP) as compared to when they are parallel (P) to one another. Mainly

because of this low ΔR, the interest in MTJs has been renewed in the past decade, though the first MTJ structure was fabricated well before the GMR discovery. But recently, Heusler alloys based CPP-GMR structures have shown promise with demonstration of ~40% GMR at room temperature.[17]

The core part of an MTJ is a sandwich of two thin ferromagnetic layers separated by a thin insulating spacer layer which forms a tunnel barrier. Application of a bias voltage across the barrier results in the flow of a finite current through the junction because of quantum-mechanical tunneling. This means that a distinctive property of an MTJ, compared to spin valves, but common to any tunneling device, is the exponential dependence of the tunneling current on the thickness of the tunnel barrier.[18]

The potential of MTJs for devices is quite intriguing, since the resistance of an MTJ can be varied over many orders of magnitude simply by varying the thickness of the dielectric spacer layer. Also, a small variation in the deposition parameters may further lead to large variations in the barrier resistance. Moreover, for many device applications, it is the signal-to-noise ratio in the frequency range of interest that determines the sensitivity of the MTJ device. The main sources of noise in an MTJ are Johnson noise, which scales with the square root power of the resistance of the device, and shot noise, which increases with the square root power of the current through the device. [19]

The reason for the higher sensitivity of spin-dependent tunneling (in MTJs and granular films) compared to spin-dependent scattering in metallic GMR structures is because the number of carriers is smaller in tunneling systems; however, a greater percentage of these carriers contribute to MR. The following sections will elaborate on

the fundamentals of spin-dependent tunneling (MTJs and granular films) that forms the crux of this work.

1.4 Spin-dependent tunneling

The essence of an MTJ is spin-dependent tunneling wherein electrons tunnel between two FMs separated by a tunnel barrier that may be an insulator or vacuum. The most important aspect of an MTJ is the dependence of tunneling current on the relative orientations of the FMs as in a GMR device. The era of spin-dependent tunneling was spurred by Meservey and Tedrow[20, 21] and the first demonstration by Julliere in 1975.[22] Reliable and stable data of high TMR (~10%) were reported only in 1995 by two groups independently.[23, 24] One of the reasons for the delay in realization of tunnel junctions was the demanding technology required for the fabrication. The report of TMR of about 10% by two groups created a renewed interest in the research of MTJs and triggered its commercialization in products such as hard disk drives and MRAMs.

1.4.1 Electron tunneling

A metal-insulator-metal (MIM) structure is referred to as a tunnel junction and in order to explain the tunneling phenomena realistically, the electronic structure of the entire trilayer system has to be considered since the decay constant of the electron wave function depends on both the complex electronic structure of the insulator as well as its coupling to the electrodes.[2] Figure 1.7 is a pictorial representation of MIM structure. The tunnel current depends on the product of DOS in the left $\rho_l(E)$ and the right $\rho_r(E)$ electrode at the same energy, multiplied with the transmission probability through the tunnel barrier represented by the tunnel matrix elements $|M|^2$. In order to take into account the occupied states in the left and the available states in the right

electrode, *f(E)* and *f(E-eV)* should also be included in the equation to calculate the net tunnel current, where *f(E)* is the Fermi-Dirac function.

$$G = \frac{dI}{dV}\alpha|M|^2 \int \rho_l(E)\rho_r(E - eV)\frac{df(E - eV)}{dV}dE$$

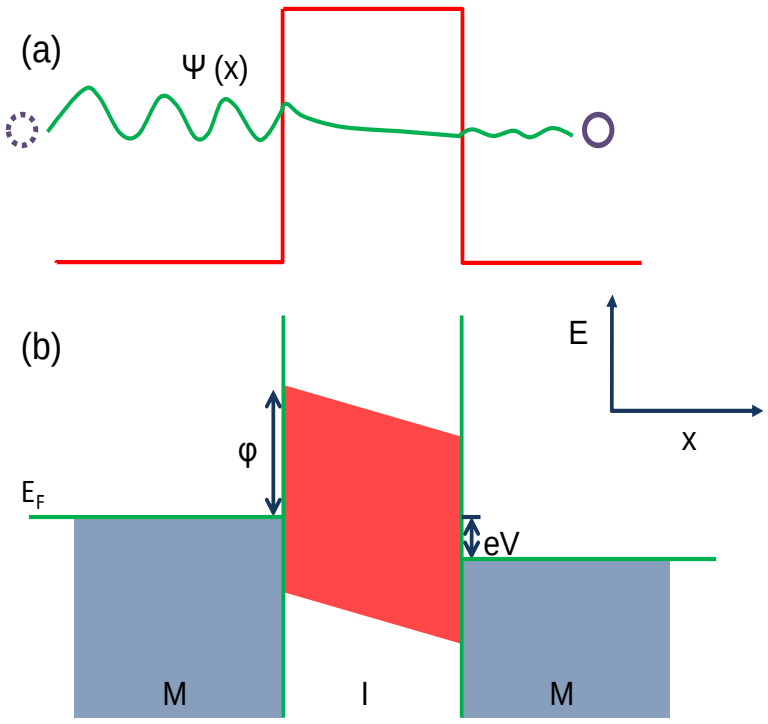

Figure 1.7 Tunneling in MIM structures (a) Electron wave function decays exponentially in the barrier region and non-zero transmission for thin barriers (b) Potential diagram for an M/I/M structure with applied bias eV. Blue region represents filled states, open areas are empty states, and the red region represents the forbidden gap in the insulator.

1.4.2 Spin polarized tunneling (SPT) technique – beginning of SDT

Considering two theories – tunnel current being proportional to the DOS and the two-current model for current flow in an FM metal – one would expect that a FM-I-M structure would give a spin polarized tunnel current. Using this postulate and Al superconducting electrodes as spin detectors, Meservey and Tedrow conducted pioneering experiments that laid the foundation of spin-dependent tunneling as well as the concept of MTJs. Using this technique, spin polarized tunneling (SPT), the tunnel

spin polarization of all the FMs (Ni, Co, Fe, CoFe, NiFe, LSMO, CrO_2) was positive, except for $SrRuO_3$. For Fe, Co and Ni, this result led to more confusion since all of these have a DOS dominated by a minority carrier near the Fermi level. A simple explanation was given by Stearns: d-like electrons carrying the majority of the magnetic moment have a higher effective mass, hence resulting in a very high decay rate in the tunnel barrier while s-electrons that are itinerant contribute little to the moment but mostly to the current.[25] Hence, although the minority channel dominates the DOS at the Fermi level, the tunnel current is dominated by the majority channel. Still, the effect of the barrier electronic structure as well as the FM-barrier interface has been overlooked.

The interfacial DOS of the FM will inevitably be affected by the interfacial bonding with the barrier, which in turn will change the spin polarization as explained by Tsymbal and Pettifor.[26] Experimentally, both positive and negative spin polarization have been demonstrated for the same FM, with different types of insulator barriers. Hence, either barrier or FM alone is inadequate to explain the spin transport mechanism in MIM structures realistically and the FM-barrier interface structure plays a very important role.[27]

1.4.3 Magnetic tunnel junctions

Instead of using the Zeeman-induced split in the DOS in a superconductor as the spin detector, exchange split DOS of FM can also be used and Julliere was the first to realize this in 1975.[22] He proposed a model for tunneling between to FMs. This MIM structure with M as FM is referred to as an MTJ. The tunnel current equation itself manifests a potential magnetic switch in an MTJ. As the relative orientations change from P to AP, the available DOS in the second electrode changes which alters

the tunnel current, and hence leading to the difference in the conductance values as illustrated in the schematic below.

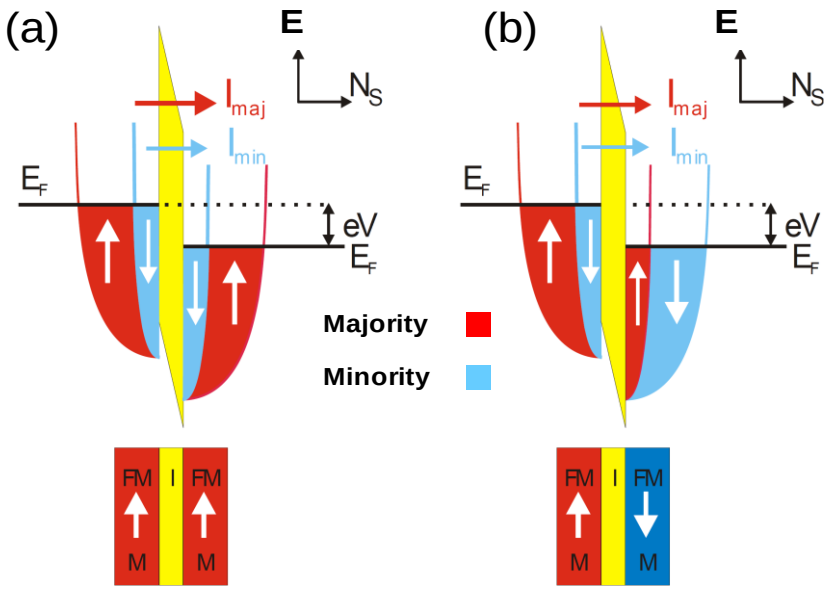

Figure 1.8 Schematic illustration of tunneling process: (a) and (b) show the density of states for parallel and anti-parallel magnetization configuration of an MTJ.

The DOS of each electron spin in the ferromagnetic electrode is shifted against the other because of the exchange splitting caused by the internal magnetic field. A bias voltage is applied across the barrier to generate a tunneling current; here, the voltage is applied such that the electrons tunnel through the barrier from the left electrode to the right one. The tunneling current is predominantly carried by the electrons whose states are closer to the Fermi energy. In order to conserve the spin during the tunneling process, the electron that travels from one spin state on the left electrode must be accepted by the same unfilled spin state on the right electrode [Figure 1.8]. Consequently, the number of electrons that can tunnel through the barrier is limited by the number of filled states on the left electrode and the number of unfilled states on the right electrode.

The performance of an MTJ is usually gauged by its TMR (%), which is a measure of the relative conductance difference of the P and AP orientations of the two magnetic layers in the structure. TMR depends on various parameters, primarily applied bias, measurement temperature and choice of materials for the barrier and FM. Julliere's model provides a quantitative analysis for the TMR as well as the current in the P and AP states.

Julliere's assumptions are as follows (explained in detail later):

- Spin is conserved during the tunneling process.
- Two-current model is applicable.
- Tunneling occurs between the bands of same spin orientation.
- Tunneling probability $|M|^2$ is spin-independent so that only the DOS determined the TMR.

One of the limitations – or rather, a missing link in this model – is that the tunneling probability is spin- as well as energy-independent, and hence the symmetry-based spin filtering is ignored which became very important in crystalline and textured barriers later. The spin polarization of the tunnel current depends on the effective masses of the different band electrons (which in turn control the decay rate inside the tunnel barrier) and also the interface bonding with the tunnel barrier.[27, 28]

The first-ever MTJ fabricated by Julliere (Fe/Ge/Co structure) showed a TMR of 14% at zero bias dropping rapidly with the bias. However, Julliere's results were never reproduced by any other group and the interpretation remains a subject of debate. Nevertheless, the findings were groundbreaking and triggered some research activity. However, it was only in 1995 that the true potential of MTJs was realized after experimental demonstration by two groups independently – Moodera and Miyazaki.[2]

1.4.4 TMR- resistance versus magnetic field

One can achieve independent electrode magnetic states by using two ferromagnetic metal films with different coercivity fields. Different coercive fields can be achieved by either using different film thicknesses or by choosing different metals for the two electrode layers. In an MTJ structure the layer with a smaller H_c is referred to as the free layer and the one with higher H_c is called the fixed or the reference layer. However, for commercial applications as sensors, a higher sensitivity is required which is accomplished by using an exchange biased structure where the H_c is increased using an antiferromagnet layer. Despite the technological advantage of using an AFM layer which allows one to study MTJs with identical FM electrodes[29], it also creates issues with TMR degradation, especially after annealing.[30]

1.5 Recipe for giant TMR: crystalline barriers with coherent tunneling

1.5.1 Coherent tunneling v/s incoherent tunneling

1.5.1.1 Incoherent tunneling through an amorphous barrier

Various Bloch states with different symmetries of wave functions exist in the electrode. In an incoherent tunneling process, Bloch states with various symmetries can couple with evanescent states in Al–O and therefore have finite tunneling probabilities. This is due to the amorphous (nonsymmetrical structure) nature of the tunnel barrier, as a result of which there is no crystallographic symmetry in the tunnel barrier [Figure 1.9 (a) and (c)]. However, the actual tunneling process through the amorphous Al–O barrier is an intermediate process between the completely incoherent tunneling represented by Julliere's model. Julliere's model assumes that tunneling probabilities are equal for all the Bloch states in the electrodes. This corresponds to a state of complete incoherency. However, for Al-O barriers, this is not valid as

experimental polarization for FM metals such as Co and Ni has been found to be positive as opposed to what Julliere's model predicts. However, with Al-O barriers the net spin polarization is limited (60%) since along with Δ_1 states (large and positive polarization), Δ_2 states (small and negative polarization) also contribute to the tunneling current. High spin polarization is possible with epitaxial or textured MTJ crystalline MgO (001) barrier [Figure 1(b)].[31]

Aluminium oxide – because of its suitability for forming a thin (~10 Å), smooth, and dense barrier layer, along with its relatively high bonding energy with oxygen (>3 eV) – has been the most extensively studied amorphous tunnel barrier layer. Another one is Titanium oxide TiO_x which has a band gap of 100meV, enabling a low RA product with a thick enough barrier, which is important in achieving low noise hard disk drive playback heads. Both of these can be fabricated by commonly used sputtering techniques, which enable robust manufacturability and are thus are used in commercial products. Nevertheless, the maximum value of TMR is limited, with 70% being the maximum demonstrated using CoFeB electrodes.[32] This is due to the incoherent tunneling of electrons through the barrier that limits the spin polarization of the structure.

1.5.1.2 Crystalline MgO (001) as the tunnel barrier

MgO has a direct band-gap at Γ point and for thicker barriers, carriers coming from the Γ point ($k_{\|}=0$) dominate tunneling. The state with the minimum decay rate k_{min} has Δ_1 symmetry. Hence if the electrodes possess electrons with this symmetry, they will tunnel through the MgO barrier efficiently. The Fe band structure is one such example where the Fermi surface has Δ_1 symmetry, but only for the majority spin. Thus, a Fe/MgO system can effectively filter out electrons based on their symmetry

[Figure 1.9(b)]. This is the reason for the high and positive spin polarization of this system, although Fe has a negative spin polarization based on DOS at the Fermi energy. This high TMR for the Fe/MgO/Fe system has been demonstrated both theoretically[33, 34] and experimentally[35, 36] over the last decade. Depending on the relative orientation of the second Fe layer, the Δ_1 symmetry electrons may propagate or get blocked resulting in the low and high resistance states for the P and AP configurations respectively. In addition to bcc Fe, bcc Co and bcc CoFe also have the Δ_1 symmetry bands only for the majority band.[31]

Ideally, the TMR should be infinite for k||=0. But due to various experimental limitations, the maximum TMR yet achieved is only around 1000%.[37] Very large TMR is theoretically expected not only for the MgO (001) barrier but also for other crystalline tunnel barriers such as ZnSe (001) and $SrTiO_3$ (001). Large TMR observation is, however, mainly limited by experimental difficulties in fabricating high-quality MTJs without pin-holes and inter-diffusion at the interfaces.

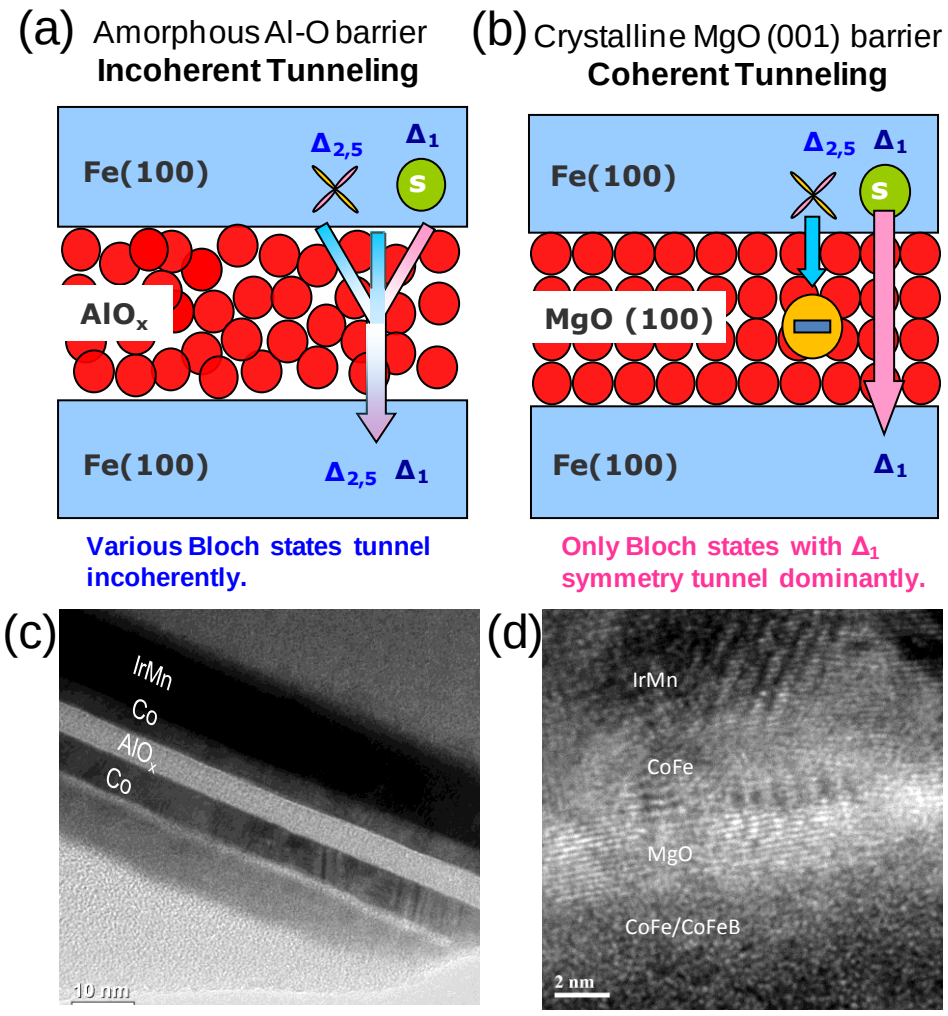

Figure 1.9 The figures displayed above help in differentiating the structural differences between amorphous and crystalline barriers both schematically and using cross-sectional TEM images.[31]

1.5.2 Limitations and challenges

- Annealing of the MTJ stack is very important for achieving crystallization of the MgO and FM electrodes and hence a high TMR. However, side-effects such as diffusion of various species such as Mn, Ru and B may create problems.[30]
- Exact concentration of impurity species such as B or Ru in an ultrathin MgO film remains very challenging.[38, 39]
- Experimentally it is very difficult to obtain an exact epitaxial relation between the MgO and the FM electrodes.[36]

- Ultra-thin MgO barriers cannot be stoichiometric due to vacancies and defects.[40]
- At present, one of the biggest challenges to overcome is the high resistance-area (RA) products of MTJs.[41] A possible solution has been presented in one of the chapters.

1.5.3 TMR over the years - MTJ experiments and barrier materials

- The first successful MTJ was prepared by Julliere (1975). The MTJ consisted of Fe/Ge/Co, where the semiconducting Ge acted as an insulating barrier. A conductance change as high as ~14% was observed at 4.2 K.[22] Primarily due to fabrication difficulties, not until 20 years later was a large TMR effect observed.
- In 1995, Moodera's group achieved 11.8% TMR in a CoFe/AlO_x/Co MTJ[24] and Miyazaki's group achieved 18% TMR in a Fe/AlO_x/Fe MTJ for AlO_x-based MTJs.[23]
- In 2001, the theoretical studies performed by Mathon *et al.* and Butler et al. showed that higher TMR values could be obtained with an MgO crystalline barrier.[33, 34] Soon after that, giant TMR of up to 200% at RT was obtained in CoFe/MgO/CoFe[35] and epitaxial Fe/MgO/Fe systems.[36]
- By adopting the metastable bcc Co as the ferromagnetic layers, up to 410% was achieved at RT.[42]
- The maximum reported TMR at room temperature in a single barrier MgO-MTJ is 604%, by Ikeda *et al.*[37]

The rapid increase in TMR in a short period has encouraged researchers all over the world to study this interesting field of spin-dependent tunneling in order to develop the next generation MR read heads and Magnetic Random Access Memory (MRAM).

1.6 Physics of TMR devices - Theoretical models to explain spin-dependent tunneling in MTJs

1.6.1 Julliere's model

Julliere proposed a model based on the spin polarization of ferromagnetic electrodes. One of his assumptions was that electron spin is conserved during the tunneling process and thus the currents due to spin up and spin down electrons were independent. He also considered the tunneling current to be comprised mainly of the electrons at the Fermi level (E_F) and so he took the tunneling probability of each channel proportional to the product of the density of states ($D_{1(2)}$) of the two electrodes at their respective Fermi levels.

$$T_{\uparrow(\downarrow)} \alpha D_1(E_{F1})_{\uparrow(\downarrow)} D_2(E_{F2})_{\uparrow(\downarrow)} \tag{1.1}$$

When magnetizations of both electrodes are parallel, the spin up (or down) electrons at E_F of the first electrode tunnel to the spin up (or down) states available at the E_F of the second electrode and the tunneling probability based on the two-current model and Julliere's model will be given as:

$$T_{\uparrow\uparrow} \alpha D_{1\uparrow} D_{2\uparrow} + D_{1\downarrow} D_{2\downarrow} \tag{1.2}$$

However, in the anti-parallel (AP) configuration, the spin up (or down) electrons tunnel to the spin down (or up) state of the second electrode. The tunneling probability here is given as:

$$T_{\uparrow\downarrow} \alpha D_{1\uparrow} D_{2\downarrow} + D_{1\downarrow} D_{2\uparrow} \tag{1.3}$$

If we define the tunnel magnetoresistance (TMR) as the conductivity difference between the P and AP magnetization states, normalized by the AP conductivity, we obtain Julliere's formula as:

$$TMR = \frac{\sigma_{\uparrow\uparrow} - \sigma_{\uparrow\downarrow}}{\sigma_{\uparrow\downarrow}} \tag{1.4}$$

The conductivity σ can be calculated using the Landauer-Büttiker (LB) formula, according to which for a two-terminal device:

$$\sigma \alpha \frac{e^2}{h} \sum T_{\uparrow(\downarrow)} \tag{1.5}$$

The TMR in terms of the density of states and spin-polarization of the two electrodes can be defined as

$$TMR = \frac{2P_1P_2}{1 - P_1P_2} \tag{1.6}$$

where P_1 and P_2 are the spin-polarizations of the two electrodes defined as

$$P = \frac{D_\uparrow - D_\downarrow}{D_\uparrow + D_\downarrow} \tag{1.7}$$

With conventional 3d ferromagnets, Julliere's model estimates a TMR value between 20-70% and a polarization (P) of approximately 0.3~0.5. This model can be used to back calculate the spin polarization of the FM electrodes in alumina based MTJs as the TMR matches the experimental values. However, the model fails to explain the giant TMR observed with MgO tunnel barriers. Also the above equation gives a negative value of spin polarization for Co, in conflict with the measured values by Tedrow-Meservey.[20] The realistic band structure of the structure needs to be considered in the calculations for quantitative understanding of the TMR. An interesting observation is that for 100% spin-polarization (half-metallic FMs), the TMR value diverges.

1.6.2 Simmon's model

While Julliere's model provides an estimate of the TMR value, it gives no information about the barrier itself. In 1963 Simmon proposed a model that allows

experimentalists to extract properties such as the barrier height (U) and width (w) from the current versus voltage curve. In his model he considered the tunnel junction as consisting of two metals with similar Fermi levels on either side of an insulating barrier of arbitrary shape. Application of an external voltage led to the bending of Fermi levels, resulting in the flow of a net current.[18]

For MTJs the most useful case is when the barrier height exceeds the bias voltage, i.e. eV<<U. The tunneling current density in this case is given by:

$$J = [(2m)^{0.5} / w](e/h)^2 U^{0.5} e^{-AU^{0.5}} V \tag{1.8}$$

The junction response in this region is ohmic. Using this model the typical barrier height for an alumina barrier has been found to be about 0.7 to 1 eV.[43]

1.6.3 Slonczewski's model

In 1989 Slonczewski came up with a model that incorporated the spontaneously split the band structure of *3d*-ferromagnets directly into the tunneling framework of Simmon's model.[44] The net result of this model was that he could not only derive the expressions for the tunneling current like Simmon's model, it also allowed him to extract the expressions for TMR like Julliere's model. By solving the wave equations and matching appropriate boundary conditions, he derived the following relations for the conductivity and TMR:

$$\sigma = \sigma_0[1 + P_{1eff} P_{2eff} \cos\theta] \tag{1.9}$$

$$TMR = \frac{2P_{1eff} P_{2eff}}{1 - P_{1eff} P_{2eff}} \tag{1.10}$$

where θ is the angle between the magnetization of the magnetic electrodes. Both the conductivity and the TMR values depend on the effective spin polarization P_{eff}. P_{eff} is related to the polarization defined in Julliere's model as:

$$P_{eff} = P\frac{k^2 - k_\uparrow k_\downarrow}{k^2 + k_\uparrow k_\downarrow} \tag{1.11}$$

where k is the absolute value of the wave-vector inside the barrier and $k_{\uparrow(\downarrow)}$ is the Fermi wave-vector in the FM electrodes.

It is still extremely difficult to predict the TMR ratio or polarization precisely in a quantitative way, since the tunneling current depends on defects and impurities inside the barrier as well as on the roughness of the interface layer, which are difficult to include even in numerical calculations. The details of the calculation methods used in this dissertation for MTJs are explained in the appendix.

1.7 Summarizing the major milestones in spintronics

In this section some of the major milestones in the field of spin electronics or magnetoresistance (MR – change in the value of resistance with external magnetic field) have been compiled of which some are only of historical importance while others set the foundations for the latest cutting-edge technology in the electronics industry. This will be followed by the detailed explanations for some of the important milestones relevant to this work.

1. **Anisotropic magnetoresistance:** On the Electro-dynamic Qualities of Metals: Effects of Magnetization on the Electric Conductivity of Nickel and of Iron by Professor W. Thomson, 1857.[45]

   MR effects are not new, and have been known since the discovery of anisotropic magnetoresistance (AMR) in ferromagnetic metals by William Thomson in 1857,

where the resistance depends on the direction of the current with respect to the materials magnetization. The AMR effect, though small compared to the newer effects (GMR and TMR), was significant in increasing the areal density of hard disk drives (HDD) by replacing the inductive readers as the magnetic sensors.

2. **Two-current model:** The Resistance and Thermoelectric Properties of the Transition Metals by N. F. MOTT, F.R.S., H H. Wills Physical Laboratory, University of Bristol (1936).[11]

   This model describes the electrical current in a ferromagnet to be comprised of two independent channels of spin-up and spin-down. The main postulates of the model were that the spin of the charge carriers (electrons) is conserved during the scattering processes and each spin contributes independently to the net resistance and thus can be represented by a parallel resistance circuit.

3. **Magnetic Tunnel Junctions (MTJs):** Tunneling between ferromagnetic films by M. Julliere, (1975).[22]

   Julliere was the first to demonstrate an MTJ. He obtained sufficiently high MR in ferromagnetic films separated by an insulator at low temperature. No other group was able to reproduce his results and even today his results are not clear. Finally in 1995, two independent groups observed high TMR values in MTJs with alumina barrier.[23, 24]

4. **Giant Magnetoresistance (GMR):** This discovery won for the groups of Albert Fert and Peter Gruenberg[46, 47] the 2007 Nobel Prize in Physics. In its most basic realization, a GMR device consists of two thin magnetic metal films, separated by non-magnetic metal. Anti-parallel and parallel configurations of the magnetic orientation of the two magnetic layers give a high and low resistance respectively with the relative difference as high as 20-30% at room temperature. GMR is based on the spin-dependent scattering of the electrons at the interfaces and the bulk of the layers.

5. **Spin Transfer Torque:** Another breakthrough was the prediction in 1996 that the magnetization of the layers could be controlled by direct transfer of spin angular momentum by a spin polarized current.[48, 49] Finally in 2000, the first experimental demonstration that a Co/Cu/Co current perpendicular to the plane (CPP) spin-valve nano-pillar can be reversibly switched by this 'spin-transfer' effect between its low (parallel) and high (antiparallel) magnetoresistance states was presented.[50, 51] The ability to use current to switch magnetic layers will provide a big advantage over field-induced magnetic switching for storage applications.[52]
6. **MgO Barrier:** In 2001, a series of theoretical calculations predicted extremely high TMR ratios for Fe/MgO/Fe MTJs, where the tunnel barrier is a crystalline MgO layer with (001) texture.[33, 34] According to these papers, a coherent lattice matching between the (001) plane of body-centered cubic (bcc) Fe and the (001) plane of MgO results in a spin-dependent match between the evanescent states within the tunnel barrier and the electronic states of the Fe electrodes. Finally in 2004, two independent groups proved the theory right by demonstrating TMRs in excess of 100% at room temperature, not achieved anytime before in MTJs.[35, 36]

1.8 Granular magnetic films

Previous sections have discussed spin-dependent tunneling systems based on MTJs where both the tunnel barrier and the FM layer are continuous thin films. Another example of a similar tunneling system is a magnetic granular system whereby magnetic granules are embedded in an insulating matrix. Such a system is equivalent to a complex network of many nano-MTJs and exhibit MR similar to GMR and TMR systems. The tunnel current is small when the magnetization vectors of the granules are randomly oriented and increases as the moments align in the presence of an

external magnetic field. The Inoue-Maekawa model[53] describes the theory of tunneling magnetoresistance in granular magnetic films where the transmission coefficient |T| depends on the relative orientation θ of the magnetization vectors $\mathbf{M_1}$ and $\mathbf{M_2}$ of two adjacent granules.

$$|T| \propto (1 + P^2 cos\theta) e^{-2\kappa s}, \tag{1.12}$$

$$P = \frac{D_\uparrow - D_\downarrow}{D_\uparrow + D_\downarrow}, \quad \kappa = \sqrt{2m^*(V - E_F)/\hbar^2} \tag{1.13}$$

where D is the density of states [for up (↑) and down (↓) spins] and *s*, *m** and *V* are the thickness of the barrier, effective mass of the electrons and barrier height, respectively.

Though a granular magnetic system is more complex compared to an MTJ, it enables observation of interesting physical effects such as magneto-coulomb blockade, and some recent theoretical reports predict giant TMR in these systems.[54]

1.9 Resistive switching mechanism in magnetic systems

Resistive random access memory (ReRAM) is another strong candidate for ideal memory particularly due to its structural simplicity, scalability and speed. The ReRAM cell is a simple structure composed of an insulating layer sandwiched between two metal electrodes. This memory is based on a phenomenon called resistive switching (RS)[55] where the resistance of the structure changes (>1000%) on application of voltage across the device. The changes in the resistance are attributed to various mechanisms including formation and rupturing of conducting filaments, and electromigration of oxygen vacancies or carrier injection (discussed in detail later). The critical issues related to the large-scale commercialization of ReRAM[56, 57] include data retention and endurance. As mentioned earlier, magnetic materials-based memories like MRAM are known for their endurance and data retention. Addition of

magnetic elements may help to overcome the above issues. At the same time it will also provide an additional degree of freedom in the ReRAM. The development of a new memory system combining the benefits of two independent candidates for the next generation[4] (ReRAM and MRAM) will be an interesting strategy to overcome the current challenges- for example combining high speed and reliability with low cost.

With the fundamental understanding of the spintronics device concepts, we have carried out several experiments in magnetic tunneling systems. The outline and the objectives of this thesis are presented in the following section. The next chapter will provide the details of the experimental methods that were adopted and the following chapters will cover the experimental results and discussion in detail.

1.10 Organization of the thesis

Chapter 1 provides an introduction to the pros and cons of current memory and data storage technologies and emphasizes the need for an ideal memory. MRAM, which is fundamentally based on spintronics, is a strong contender for that role. The chapter introduces the fundamentals of spintronics with a detailed discussion of systems and devices based on spin-dependent tunneling. Magnetic granular films and magnetic tunnel junctions have been selected as the material systems to be studied in this dissertation. Chapter 2 will elaborate on the experimental methods and strategies adopted in this work. All the deposition (magnetron sputtering, thermal evaporation), fabrication (lithography, lift-off and ion-milling) and characterization techniques (structural, magnetic and electrical) used have been briefly covered. Granular magnetic films are studied in detail in Chapters 3 and 4 using both experiments and theoretical modeling. Chapter 3 presents the resistive switching characteristics of the magnetic granular magnetic films and the control of the switching characteristics using an

external magnetic field while Chapter 4 examines the effects of a high electric field on the magnetic moment of the magnetic granules. The tunneling characteristics of MTJs are examined from Chapter 5 onwards. In Chapter 5, the effect of substrate bias during deposition of Al_2O_3-based MTJs is investigated based on changes in the structural, chemical composition and magnetic properties. The optimization of the CPP-MTJ fabrication process has been described in detail in Chapter 6 and TMR ratio in excess of 250% has been demonstrated. Chapter 7 presents the effect of strain using diamond-like carbon (DLC) films on the tunneling properties of MgO-based MTJs. The experimental results are supported by theoretical calculations that have a qualitative agreement. The magnetic field dependence of the capacitance (tunnel magnetocapacitance TMC) and the frequency dependence of TMR in MgO based MTJs will be reviewed in Chapter 8. An *RC* equivalent circuit for MTJs will also be proposed. The final chapter summarizes all the findings of this thesis and provides some suggestions and recommendations for future work.

1.11 Objectives

Our aim was to study the characteristics of spin-dependent tunneling systems in order to develop new device concepts and suggest improvements in the existing technologies. The detailed objectives of the thesis are as follows:

1. To investigate the electrical and magnetic properties of an optimized Co/Al_2O_3 granular multilayer structure.
    a. To tune the resistive switching characteristics of the system using an external magnetic field and to explain the mechanism using a theoretical model.

b. To analyze the effect of a high electric field on the magnetic moment of the Co granules and understanding the changes with the help of theory.

2. To fabricate high quality MTJ structures and realize high TMR.
   a. To study the effect of substrate bias during deposition on the structural, chemical and magnetic properties of Al_2O_3-based MTJs.
   b. To optimize a process to achieve a high TMR MTJ using an MgO tunnel barrier.
   c. To study the effect of strain on the spin-dependent tunneling characteristics of MTJs using a highly stressed DLC film (cap layer) and to support the experiments with theoretical studies.
   d. To characterize temperature dependence of the tunneling features at high frequency using capacitance measurements.

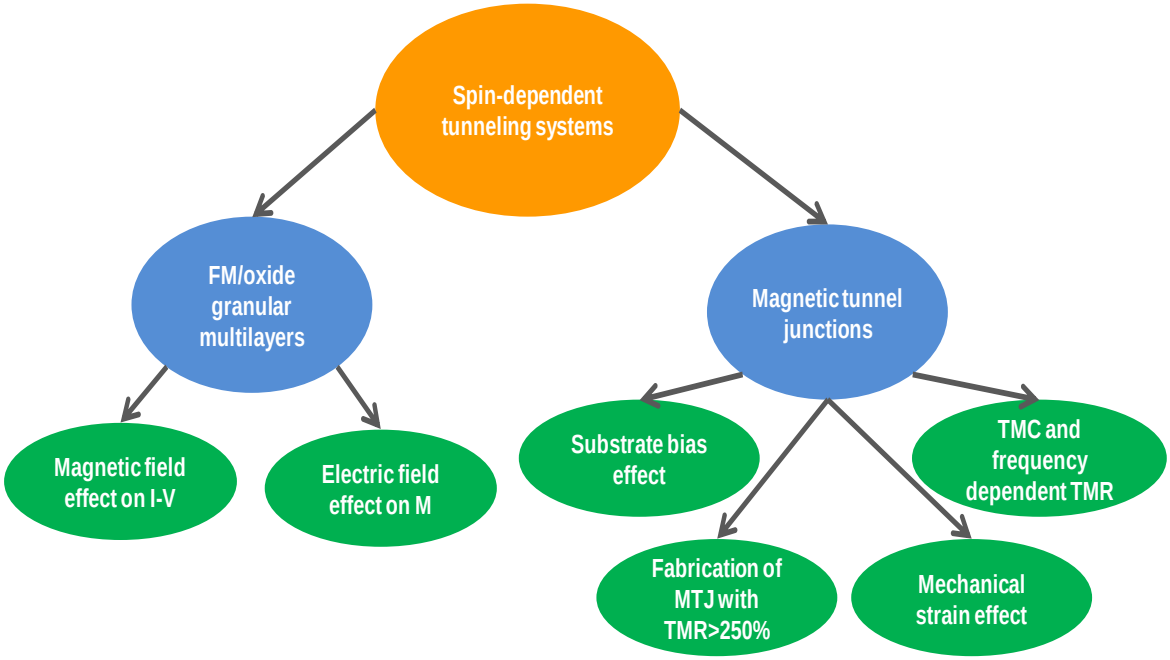

Figure 1.10 A schematic summary of the work done in this dissertation. Theoretical calculations have also been performed to support the experimental results.

In magnetic granular multilayers, a resistive switching phenomenon was demonstrated and the switching voltage was gradually reduced by increasing magnetic field applied parallel to the film surface. This is the first report of a controlled magnetic field control of resistive switching process. The switching characteristics are a function of the magnetic and oxide material and the granule concentration. Direct and controlled electric field induced magnetization changes in magnetic granular systems are also demonstrated for the first time. In magnetic tunnel junctions, strain induced by a DLC cap layer was shown to reduce the junction resistance. Similar experiments have been performed in semiconductor based devices however this was the first demonstration of control of spin transport in a spintronics device. The results have been explained using theory. A model for equivalent capacitance has also been proposed for MTJs that provides a clearer understanding of the experimental results.

Chapter 2 : Experimental techniques

This chapter will present an overview of all the experimental techniques that have been used in the work. The first part will cover the techniques used for thin film deposition. This will be followed by the methods adopted for device fabrication – from bare Si wafers to final devices. The final part will discuss the various characterization techniques that have been adopted for device and film analysis – micro-structural, chemical, magnetic as well as electrical.

2.1 Thin film deposition processes

2.1.1 Magnetron sputtering

Sputtering is among the most popular deposition techniques used in the industry as well as academic research. The basic approach is to eject atoms to be deposited from the source target by physical ion (argon) bombardment. The source of the ions can either be the plasma of an inert gas or an ion beam. Plasma-based sputtering is more popular and depends on the interrelationship between various parameters such as discharge voltage, current and the gas pressure, the understanding of which can be very challenging. In order to sustain the plasma discharge, a high working pressure is required (few Pa). A high working pressure is not an ideal condition for film growth as the energy of the sputtered particles is reduced, resulting in poor adhesion as well as granular films. One of the ways to avoid such a situation is to increase the number of available electrons at the cathode. The classical approach for this is to apply a magnetic field to trap the electrons in the discharge, causing more ions to be generated from the target with the same electron density. In the presence of a magnetic field, electrons describe helical paths around the lines of the magnetic force

and the deposition rate increases compared to simple diode glow discharge systems. This approach is referred to as magnetron sputter deposition. Figure 10.1 shows a schematic representation of magnetron sputtering. For metallic film deposition like the ferromagnetic metals and the electrodes, a DC power supply is used and the process is referred to as direct current (DC) magnetron sputtering.[58, 59]

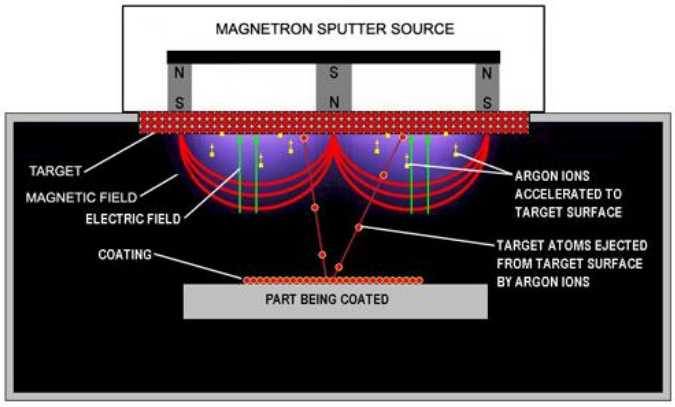

Figure 2.1 Schematic of magnetron sputtering.[60]

2.1.2 Radio frequency (RF) magnetron sputtering

Oxide films as tunnel barrier form the most important part of this work and hence the method of deposition of the tunnel barrier and its effect on its properties as well as the interface properties is very crucial. For insulators, using a DC power supply is not possible due to a consequent build-up of surface charge of positive ions on the insulator target surface which prevents further ion bombardment. Hence, for the deposition of tunnel barrier (oxides) in our study, we used an RF power supply instead of a DC supply. This process is known as RF magnetron sputtering. The primary disadvantage of using RF power supplies is the inherently low deposition rate.

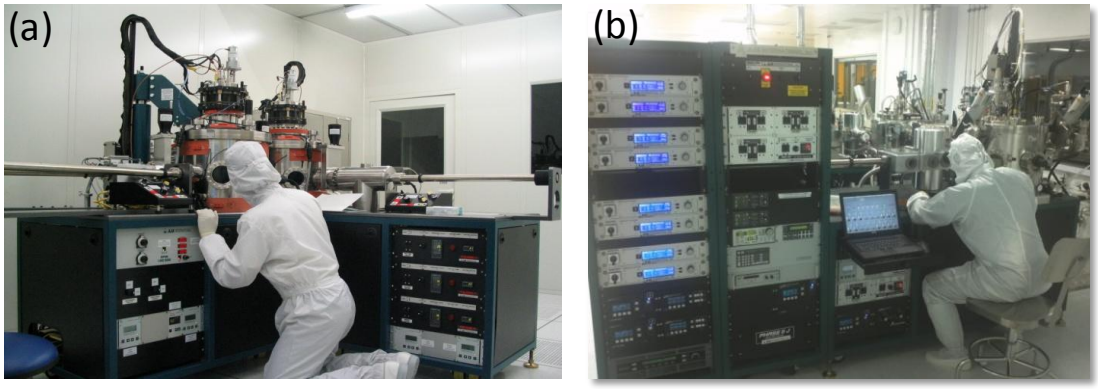

Figure 2.2 Two AJA sputter systems used in this study.[61]

Magnetron sputtering was predominantly used in this study for the thin film deposition – DC for metallic and RF for insulating targets. Two sputtering systems were used. For the initial part (first three years), we used a dual chamber system with four and six targets respectively [Figure 2.2(a)]. For the final year, we used another chamber system with 11 targets [Figure 2.2(b)]. The base pressure of this chamber could go as low as 1×10^{-9} Torr. The chamber was also equipped with an RGA analyzer that helped to analyze the background gases and moisture before deposition of films and a baking of the chamber was done whenever required. In some cases an in-situ magnetic field was applied during the deposition of the films to induce anisotropy, especially for spin valves and exchange biased-MTJs.

2.1.3 Thermal evaporation

During the evaporation process, vapors are produced from a material located in a source which is heated by either direct resistance, radiation, eddy currents, electron beam, laser beam or an arc discharge. A high vacuum ensures that the evaporated atoms undergo an essentially line-of-sight transportation prior to condensing on the substrate. Thermal evaporation was used for the deposition of Cr/Au contact pads for

some of the devices. A combined electron and thermal evaporation system from Korea Vacuum Technology with a base pressure of 1×10^{-6} Torr was used for this purpose. The system had two thermal boats and the deposition rates were monitored by a crystal oscillator which utilized the piezoelectric properties of quartz. The resonance frequency induced by an alternating current (AC) field was inversely proportional to crystal thickness. The change in frequency of a crystal exposed to the vapor beam was compared to the frequency of the reference crystal and the thickness detected.[58]

2.2 Structural and magnetic characterization techniques

2.2.1 Atomic force microscope (AFM)

AFM was introduced in 1986 to examine the surface of insulating samples (along with conducting samples). AFM can generate atomically resolved three-dimensional topographical images based on the interaction (forces) between a very sharp cantilever tip and the sample surface. Other than the sample topography, many material parameters can be studied using different versions of AFM, including friction, capacitance, electrostatic potential, magnetization, doping profile, strength, etc. This force depends on the nature of the sample, the distance between the probe and the sample, the probe tip geometry and material, and sample surface contamination. The instrument consists of a cantilever with a sharp tip mounted on its end. The cantilever is commonly made from Si, SiO_2 or SiN. For imaging, the tip is brought in constant contact (contact mode imaging), intermittent contact (tapping mode) or very close to the sample surface (non-contact mode) and scanned across the sample. The deflection of the cantilever at every data point is sensed and the force between the tip and the sample is calculated (the stiffness of the cantilever should be known). The most

common implementation measuring deflection uses a laser spot reflected from the top surface of the cantilever into an array of photodiodes.

Tapping mode AFM was used for the surface analysis (RMS surface roughness and thickness in some cases) of all the films using a Bruker system [Figure 2.3(a)] - with area scans as small as 0.5 μm^2 and a spatial resolution of less than 50 nm. This mode of AFM has several advantages over the contact mode including higher lateral resolution, lower forces and less damage to soft samples scanned in ambient conditions. In this mode, variations in topography were detected from changes in the cantilever oscillation frequency or amplitude.[62] A schematic of AFM is shown in Figure 2.3(b).

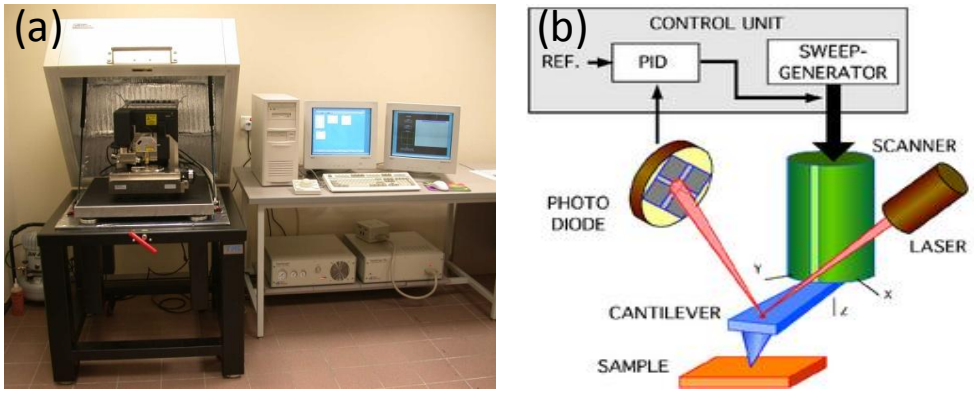

Figure 2.3 (a) Digital instruments SPM (b) Schematic of an AFM.[63]

2.2.2 Superconducting Quantum Interference Device (SQUID)

SQUID uses Josephson junctions to sense the magnetic field. In the superconducting state of materials, the magnetic flux is expelled. Hence, in a superconductor ring, the interior flux gets trapped in the ring. On turning off the magnetic field, a current will be induced which circulates around the ring, keeping the magnetic flux inside the ring constant. The current continues to circulate as long as the ring is kept in a superconducting region because R=0 Ω. In 1962, Josephson predicted

the possibility of electrons tunneling from one superconducting region to another through a resistive barrier with no voltage drop. Typically, a SQUID is a ring of superconductor interrupted by one or more Josephson junctions which uses the Josephson effect to measure extremely small variations in magnetic flux. When an external magnetic flux is coupled into the Josephson loop, the voltage drop across the Josephson junction will change. Monitoring the change in voltage allows determination of the magnetic flux that has been coupled into the SQUID loop. A Quantum design [(SQUID-MPMS) with sensitivity as low as 1×10^{-8} emu and a maximum field of 2 T], was used for the magnetization loops of different samples at room temperature as well as lower temperatures [Figure 2.4(a)].[64]

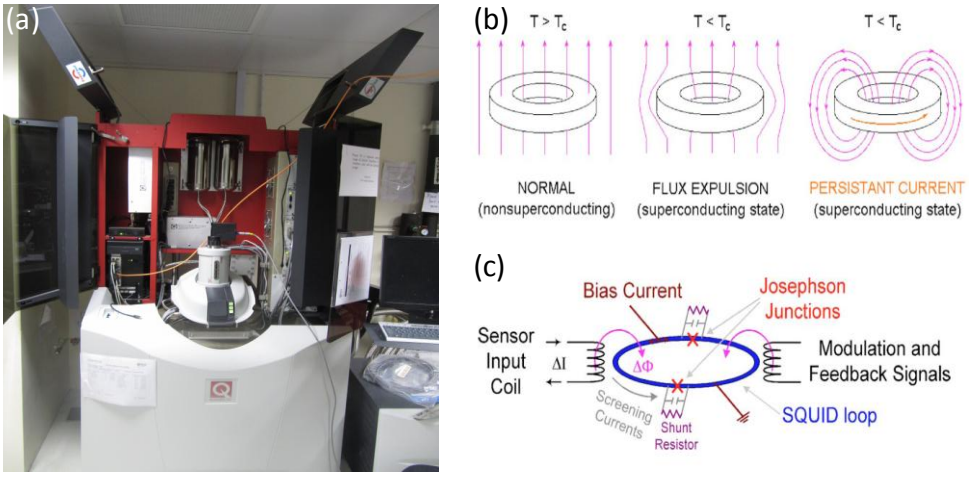

Figure 2.4 (a) Quantum Design MPMS (b) Meissner effect in a superconducting ring cooled in an externally applied magnetic field and (c) dual junction DC SQUID loop.[64]

2.2.3 Alternating gradient force magnetometer (AGFM)

AGFM is a popular technique for the measurement of M-H loops due to its high sensitivity, but great caution must be exercised in order to avoid large errors in the measurement results. In an AGFM, the sample is mounted onto a piezoelectric transducer which oscillates when the sample is subjected to an alternating magnetic field gradient superimposed on the DC field of an electromagnet. The AGFM has a

noise floor of 10^{-8} emu, as opposed 10^{-6} emu for vibrating sample magnetometer (VSM). AGFM was used for some initial studies as it has the advantage of being very fast. A standard Ni sample was used for calibration purposes with a size similar to the samples to be measured. The M-H loops were observed to be similar to the ones obtained using SQUID.[65]

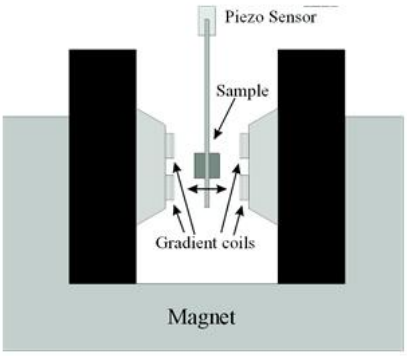

Figure 2.5 Schematic diagram of an AGFM.[65]

2.2.4 Transmission electron microscope (TEM)

A TEM uses an extremely high energy electron beam for micro-structural characterization of materials with atomic resolution. The electrons are emitted using an electron gun by thermal, Schottky or field emission. The electrons travel through vacuum in the column of the microscope and a three-four stage condenser lens system allows variation of the illumination region on the specimen. Instead of glass lenses focusing the light in the light microscope, the TEM uses electromagnetic lenses to focus the electrons into a very thin beam. The electron beam then travels through the specimen under study. The electron intensity spectrum of the transmitted beam is imaged using a lens system and recorded digitally via a fluorescent screen coupled by a fiber-optic plate to a CCD camera. The resolution of TEM is high because the elastic scattering of the electrons is highly localized to the region occupied by the screening potential of an atomic nucleus. One of the downsides of TEM is the tedious sample

preparation procedures using mechanical polishing and ion-beam milling as extremely thin samples of the order of 5-100 nm are required for 100 keV electrons to be transmitted through.[66]

Sample preparation- a thin slab of the material is cut from the area of interest in the sample and mechanically polished as thin as possible (< 50μm). The sample material is then mounted on a half-grid and inserted into a ion milling chamber. The thickness after polishing should be less than 50 μm in order to ensure short milling times. Using an Ar ion milling system the polished sample is the etched to extremely thin region- to get a hole. The region around the hole is finally the region that is imaged. Higher angle and higher energy beam etching is then followed by a low angle low energy etching for fine etching.

In this work, field emission TEM- JEOL-JEM 2010F (200 keV) was used for cross-sectional micrographs of the granular system as well as the MTJs. The samples were first mechanically polished down to a thickness of 50 μm followed by ion-beam milling.[67]

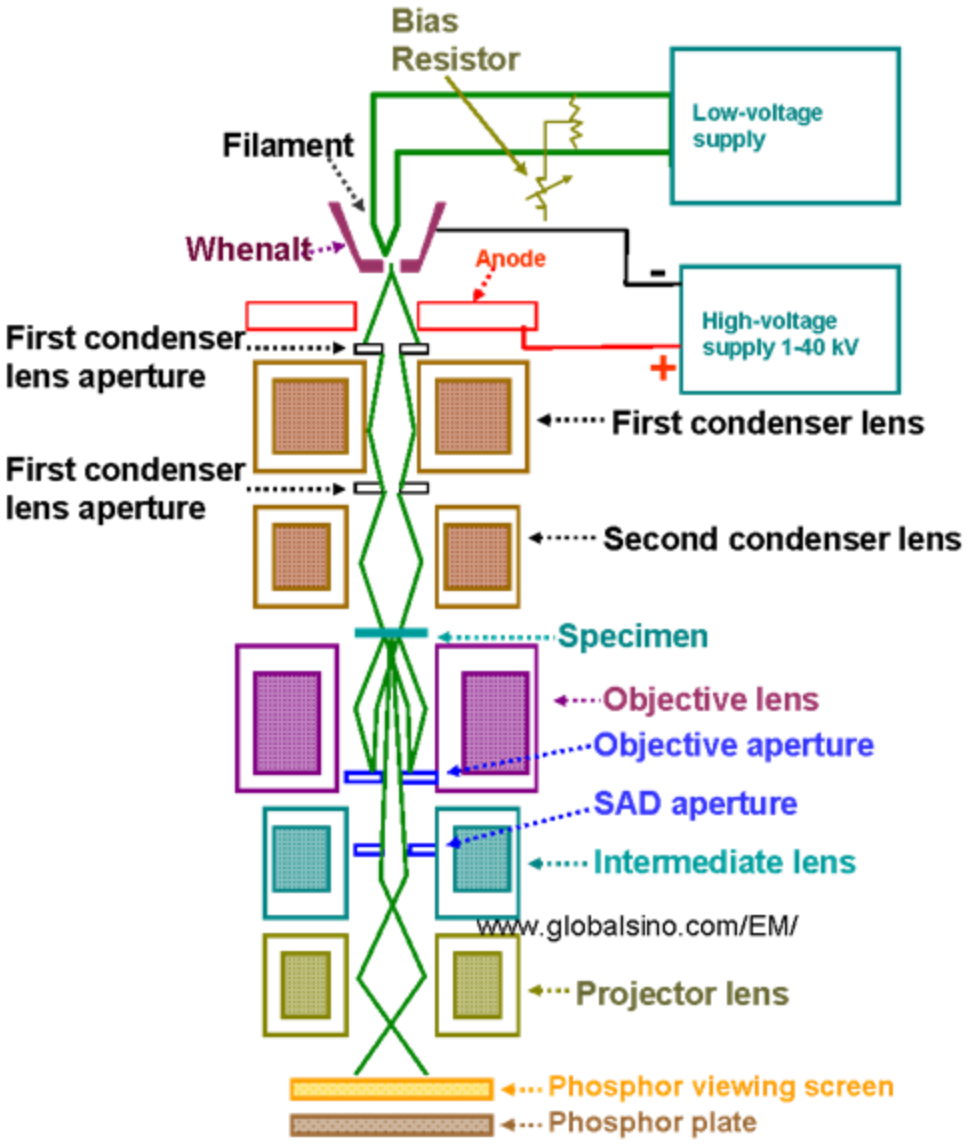

Figure 2.6 A schematic representation of TEM column.[68]

2.3 Substrate preparation

Silicon substrates (700 μm thick) with a 400 nm thick thermally oxidized SiO_2 were used for all the samples and devices in this work. The Si wafers were cut into 5 mm, 10 mm and 15 mm square samples using a Disco automatic dicing saw, depending on the requirements.

2.3.1 Cleaning of the substrates

The substrates were cleaned before being used for device preparation as the shipping, handling, dicing etc. might have contaminated them. The following steps were performed in order to ensure a clean and smooth surface for the deposition of films for device fabrication:

- Ozone stripper (10 minutes at 150 ˚C)
- Acetone (10 minutes in ultrasonic bath)
- Isopropanol (IPA) (10 minutes in ultrasonic bath)
- De-ionized (DI) water (10 minutes in ultrasonic bath)
- Isopropanol (IPA) (10 minutes in ultrasonic bath)
- Nitrogen blow dry
- Baking (5 minutes at 120 ˚C)

During transfer between different solvents, it was ensured that the sample did not dry up and leave stains on the sample.

2.4 Device fabrication

2.4.1 Photolithography

Photolithography is a process used for micro fabrication of thin film and devices. Ultra-violet light is used to transfer patterns from a photomask (hard mask) onto a photo-sensitive material called resist. A developer is used to dissolve away the exposed (unexposed) regions of the positive (negative) resist in order to obtain the patterns. For this work, a Karl Suss mask aligner (MA6) was used for the transfer of patterns onto the substrates for device fabrication – micro-pillars as well as electrode pad definition.[69]

Figure 2.7 Karl Suss MA6 with 350 nm UV lamp.

Positive photoresists – AZ-7200 (Clariant Corporation) and PFI (Sumitomo) – were used for lift-off purposes. Negative resists – maN 2401 and 2405 (Microresist) – were used for etching purposes. AZ-300MIF and ma-D developers were used to dissolve the exposed and unexposed regions in the positive and negative resists respectively.[70] The AZ-300MIF and ma-D 525 are TMAH-based while ma-D331 and 332 are NaOH-based. A bilayer resist structure was also used with lift-off resist (LOR) from Microchem under the main resist to aid in the lift-off process. Acetone was usually used to lift off the resist while the PG remover was very useful when LOR was used as an underlayer in the bi-layer resist configuration.[71] A minimum resolution of around ~1 μm was achieved using the system. The following are the steps [Figure 2.8] and specific conditions that were used:

- Spin coating 6000 rpm for 40-50 s
- Pre-baking: 95 ˚C for 90 s
- UV exposure: for AZ and PFI positive resists 12-13 s, and for ma-N resists – 19-23 s using 8 mW/cm^2 lamp intensity and a power of 350 W.
- Development time: 20-30 s for positive resists and 30 s for negative resists when using ma-D 331 or 332 and 90 s when using ma-D 525.

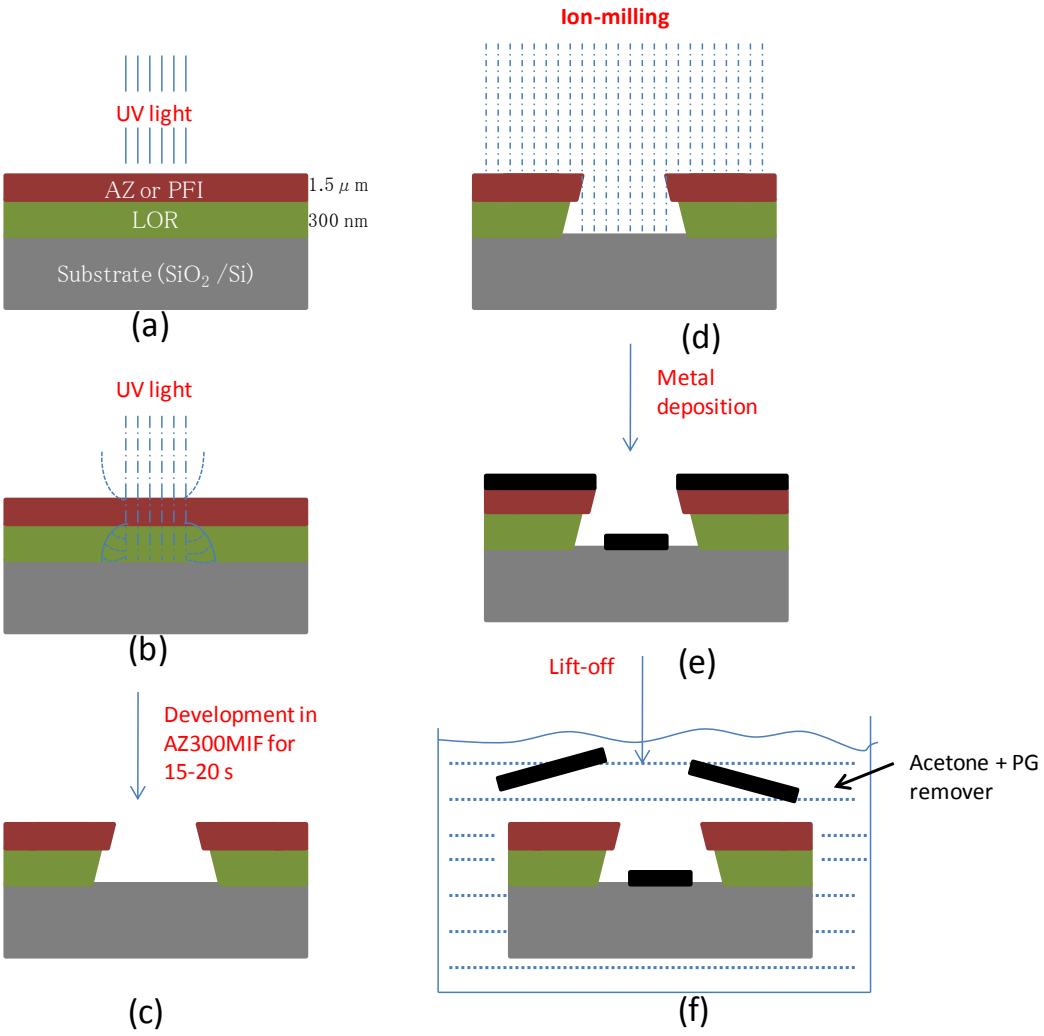

Figure 2.8 Lift-off process in detail (a) Exposure of UV light for patterning. (b) UV interaction with the resist. (c) Developing process. (d) Ion-milling for cleaning interface. (e) Metal deposition. (f) Lift-off process. The unexposed resist with the metal on top of it is removed inside acetone and/or PG remover.

2.4.2 Etching - Argon ion-miller

After the device regions have been defined by the resist, the unprotected region has to be etched away. One way is to use wet or chemical etching; however, as it is isotropic, the undercut developed cannot be controlled and this makes the process unreliable. A simpler and more reproducible process is dry etching using an ion beam [Fig 2.9(a)]. It is equivalent to an atomic level sand blaster. Before starting the etching process in an ion miller, a photolithography step is used to define a resist pattern that

acts as a protective layer for the region that is not to be etched. The etch rate of the photoresist is lower and its thickness much higher than that of the material that is being etched. Rotation of the substrate holder during etching ensures uniform removal of any unwanted parts of the structure, resulting in straight side walls in all features with near zero undercutting. This leads to a perfectly repeatable pattern time after time. Other methods of etching or cutting such as a chemical process or laser simply does not deliver the same level of precision of an ion beam etch. Furthermore, some noble metals such as Pt cannot be etched effectively using a chemical process. Argon ions contained within plasma formed by an electrical discharge are accelerated by a pair of optically aligned grids producing a highly collimated beam. A neutralization filament prevents the buildup of positive charge on the work plate.[72]

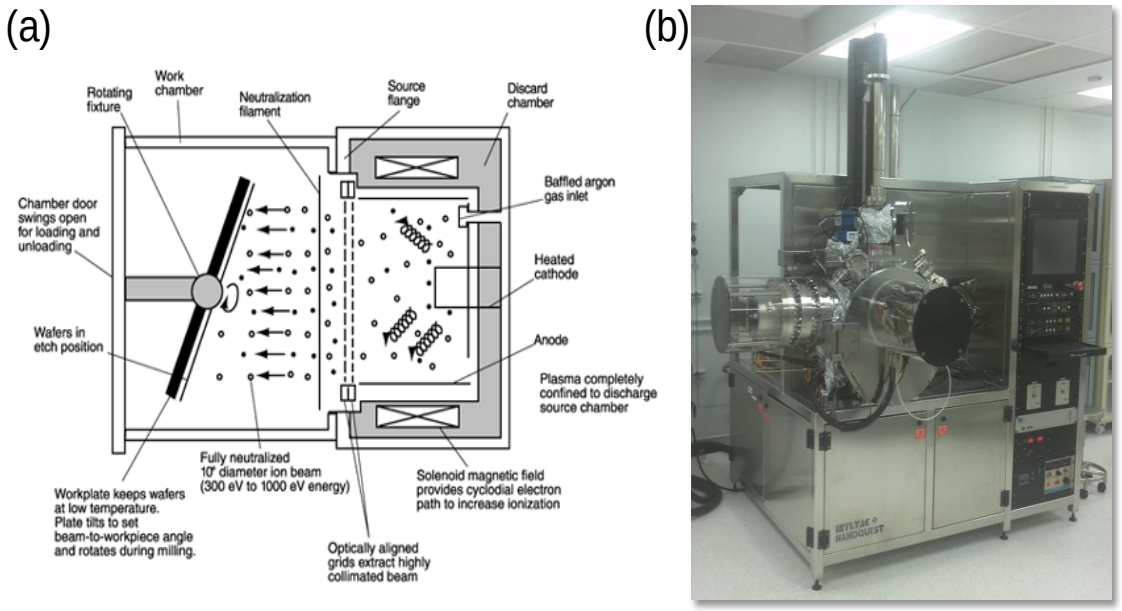

Figure 2.9 (a) Schematic of ion-milling and (b) Intlvac ion miller.[72]

Argon-ion miller was used to transfer the patterns defined by the photolithography process onto the films on the substrate as well as for cleaning the interfaces before the deposition of electrode pads [Fig 2.9(b)]. The base pressure of the system was 9 $\times 10^{-8}$ Torr. For the fabrication of magnetic tunnel junctions, the etching

parameters (etching angle, etching time, rotation speed and beam current) were optimized to achieve high TMR. The details will be discussed in later chapters. The ion-miller was equipped with four sputter guns that enabled deposition of insulating capping layers without breaking the vacuum as well as secondary ion mass spectroscopy (SIMS) with an end point detector, that allowed for the stopping of the etch process at any specific layer with nanometer accuracy. Figure 2.10 schematically illustrates the patterning process using ion-milling. Etching approach is a more reliable and clean process compared to the lift-off approach as issues like sidewall shorting (for multilayer MTJs) and substrate resist residue can be minimized.

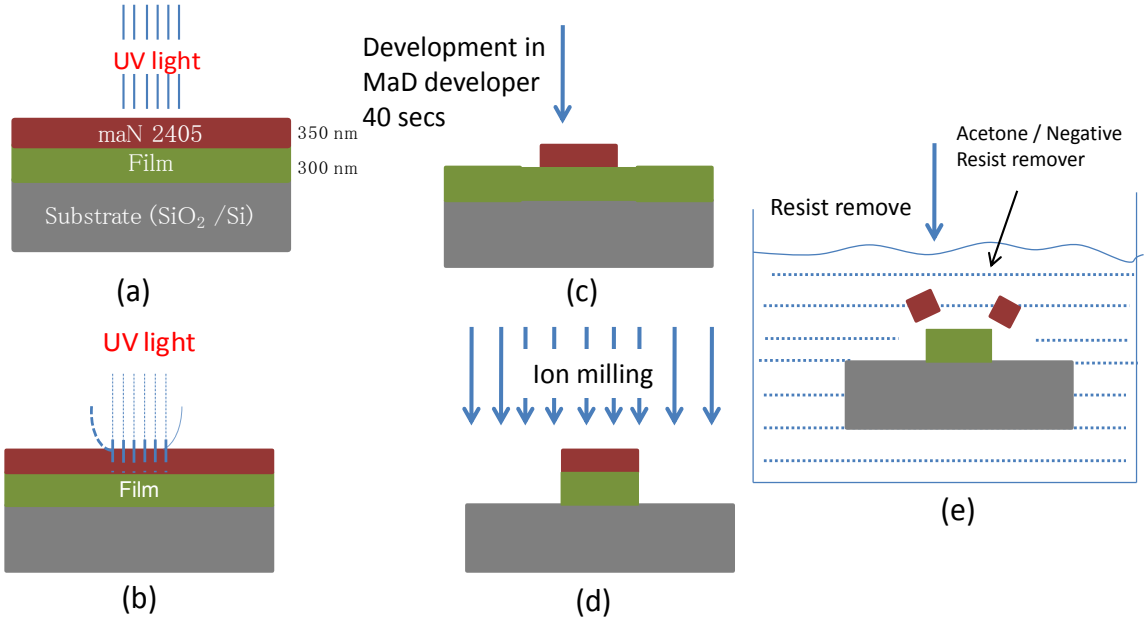

Figure 2.10 Lithography steps with negative resist. (a) The film coated with negative resist is exposed with the desired patterns by MA6. (b) UV beam interaction with the resist. (c) Developing the exposed patterns. (d) Ion milling process to remove the metal area not covered by resist. (e) Removal of resist in acetone or negative resist remover.

2.5 Electrical characterization

2.5.1 Four point probe measurement - probe station and He_4 based cryostat

Two-probe measurement appears to be faster and simpler but the analysis becomes more difficult due to the additional effect of wire (R_w) and contact resistance

(R_c). The measurement error is high mainly when the resistance of the device under test (R_{DUT}) is comparable to the parasitic resistances like an all-metallic CPP-GMR device. In a four-point measurement configuration, two additional probes of the voltmeter were placed across the device in order to measure the resistance of the device accurately. Though the parasitic resistances also contributed to the voltage path [Figure 2.11 (b)], the voltage drop across these resistances was negligible. This is due to the very low current flowing through the voltage measurement path due to a very high input impedance of the voltmeter (10 TΩ or higher). Thermal effects were also observed to be more prominent in the two-probe measurement [Figure 2.11(c)], probably a result of a higher current through the voltage measurement probes.[73]

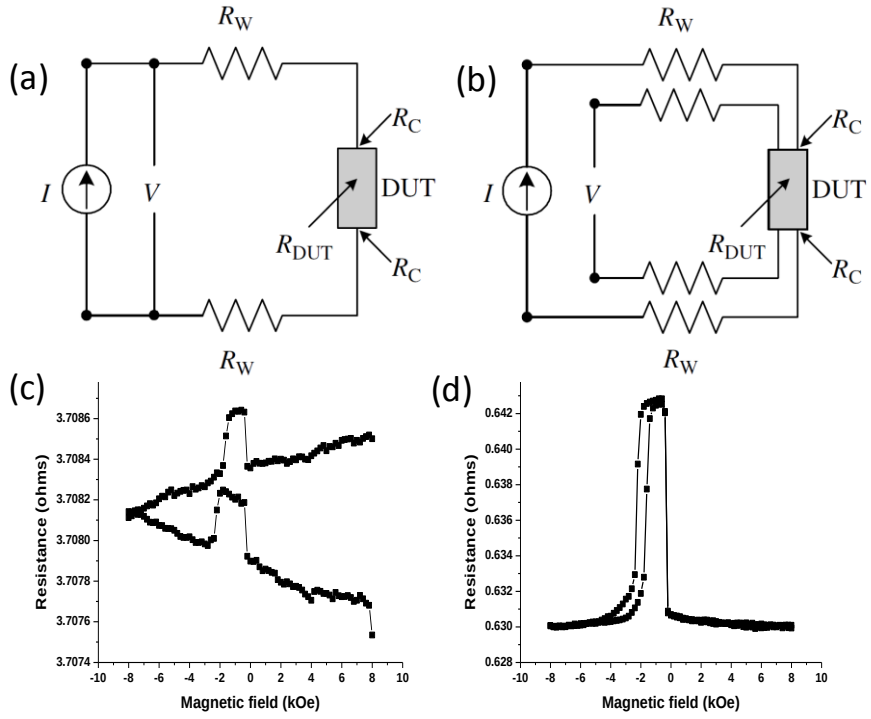

Figure 2.11. Equivalent circuit for (a) two-probe measurement (b) four-probe measurement. A GMR device measured using (c) two-probe (d) four-probe configuration.

In this study two systems were used for the transport studies of the devices. A probe station was used for instant measurements at room temperature and ambient pressure [Figure 2.12(a)]. A maximum field of 800 Oe can be applied in this system. For a temperature-dependent study, a He_4 cryostat within the pole tips of an electro-magnet was used, with a high vacuum of 10^{-6} Torr, maximum field of 7 kOe and temperature as low as 6 K [Figure 2.12(b)]. Electrical contacts were prepared using a wire bonder. A Keithley 2400 sourcemeter and 2002 multimeter were used as the current source and voltmeter respectively.

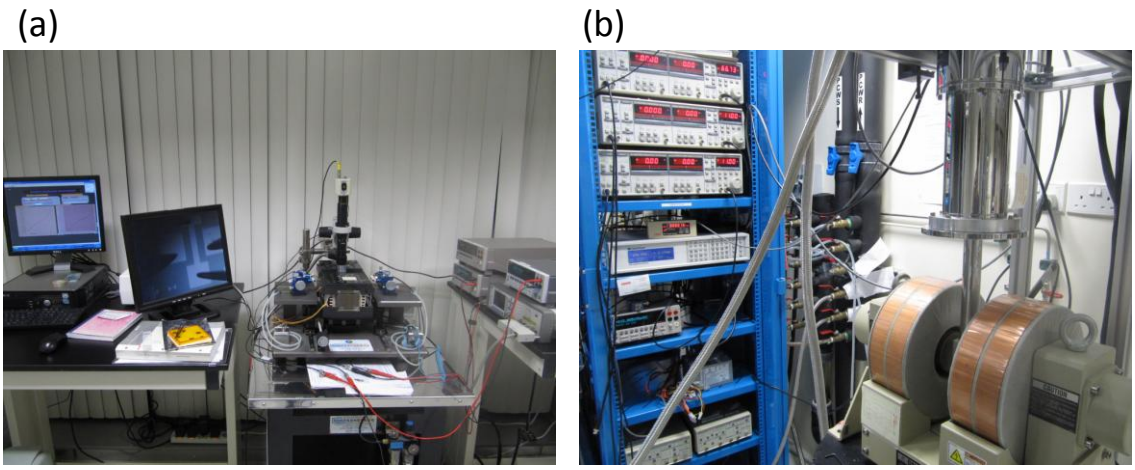

Figure 2.12 (a) Probe station for instant TMR and I-V measurements. (b) He_4 cryostat for low temperature and high vacuum transport measurements.

Chapter 3 : Magnetic field control of hysteretic switching in Co/Al_2O_3 multilayers by carrier injection

3.1 Motivation

Combining resistive switching (RS) with spintronics is an interesting idea worth exploring as RS is one of the next generation non-volatile memory technologies that the industry as well the research community worldwide is looking forward to. With some literature available on RS in Al_2O_3, we try to introduce Co granules to it and study its electric switching properties as a function of the magnetic field.

In this chapter we investigate the hysteretic switching behavior in Co/Al_2O_3 granular multilayers, in which the switching voltage significantly decreases with an increase in the magnetic field. We also propose a theoretical model of magnetic field dependence of resistive switching in the magnetic granular system based on the self-trapped electrons mechanism. The underlying mechanism is the influence of the magnetic field on electron occupation of the conduction band, which depends on the materials used in the magnetic granular system, concentration of magnetic granules in the insulating matrix, applied voltage, and charge accumulation in the granules.

3.2 Introduction

RS is a dramatic change in resistance of various metal-insulator systems induced by the electric field. Threshold RS is a switching between high resistance states (HRS) and low resistance states (LRS) where only one stable resistance state is preferable with no applied voltage. The RS phenomenon has attracted a lot of attention

due to its potential applications in memory devices. For instance, the resistive random access memory (ReRAM), based on the RS effect, is a potential candidate for the next generation of memory devices.[55, 56] Features such as high scalability, high speed, and low power operation provide an advantage over flash memory technology, which is prone to endurance issues and low speed. Structural simplicity and a higher ON/OFF ratio also gives ReRAM an edge over other promising technologies such as phase change RAM and spin transfer torque RAM. Binary oxides such as TiO_2, NiO, ZnO, CuO, TaO_2, HfO_2, etc,[56, 57] have been popular choices for RS studies. The incorporation of magnetic components into an RS system provides an additional degree of freedom and may allow control of the switching voltage with external magnetic fields.

The RS phenomenon has been extensively studied both experimentally and theoretically for over 40 years. Most of the existing theories of the RS phenomenon are widely based on the dynamic percolation model, e.g. forming and rupturing of conduction filaments [74-77] or on the migration of oxygen vacancies.[78-80] Recently, a mechanism of RS based on self-trapped electrons and holes has been proposed.[81-83] For example, Chen et al. showed evidence of current injection modulation of saturation magnetization in their RS system.[83] In this work, we have proposed a self-trapped electrons-based RS mechanism in magnetic granular multilayers and the magnetic field dependence of the electron injection. We measured *I-V* characteristics in Co/Al_2O_3 granular multilayers and demonstrated experimentally that the switching voltage can be controlled with the external magnetic field. Our theoretical calculations also suggested that the switching voltage can be significantly decreased by increasing the magnetic field.

3.3 Experimental methods

3.3.1 Film preparation

We fabricated a Co/Al_2O_3 magnetic granular system in order to study the resistive switching behavior in the magnetic granular system. Figure 3.1(a) shows a schematic of the system used in this study. A thermally evaporated Cr (5 nm)/Au (45 nm) bottom layer was deposited on Si (100) substrates with a 400 nm thick thermally oxidized SiO_2 layer. Ten layers of [Al_2O_3 (4 nm)/Co (0.5 nm)] were subsequently deposited and the structure was capped by a 4 nm Al_2O_3 layer. Co and Al_2O_3 were deposited in an ultra-high vacuum (10^{-9} Torr) magnetron sputtering chamber using dc and rf sources, respectively. Electrical contact pads (80 μm × 80 μm) were formed by thermally evaporated Cr (5 nm)/Au (45 nm) and the distance between two adjacent contacts for measurements was 50 μm. Figure 3.1(b) shows the cross-sectional transmission electron microscope (TEM) image of Co/Al_2O_3 granular multilayers. The Co nanoparticles were clearly visible, embedded in an Al_2O_3 insulating matrix. The Co formed a discontinuous layer of nanodots with a diameter considerably larger than the nominal layer thickness of 0.5 nm.[84, 85] X-ray photoelectron spectroscopy (XPS) depth-profile analysis showed alternate peaks of [Al (2p), O (1s)] and Co (2p).

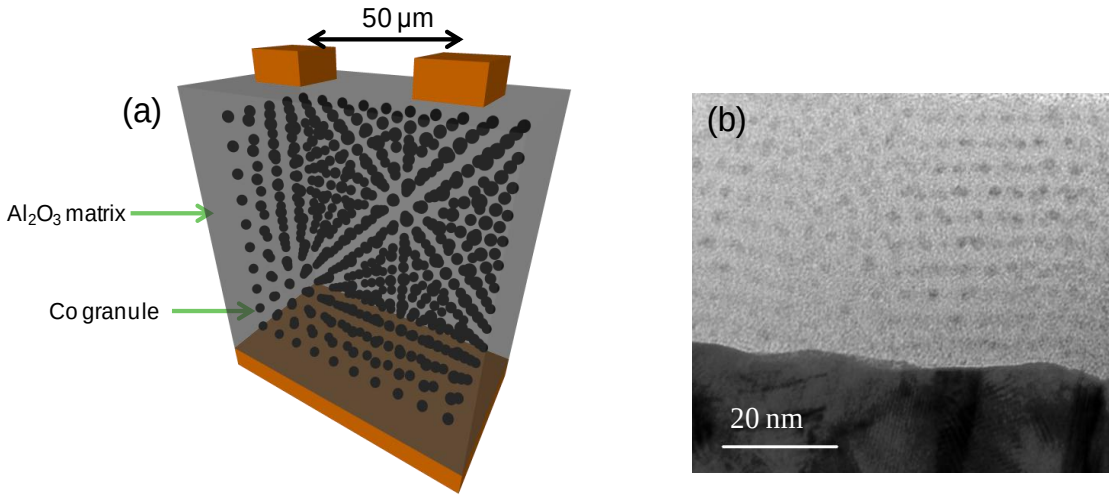

Figure 3.1 (a) A three-dimensional schematic of the Co/Al_2O_3 multilayer system. (b) Cross-sectional transmission electron microscope (TEM) image of Co/Al_2O_3 multilayers. The dark spots are Co islands and the white region is an Al_2O_3 insulating matrix.

3.3.2 Transport properties:magnetic field dependent I-V characteristics

The *I-V* measurements were carried out in ambient conditions. The initial state of the Co/Al_2O_3 was an insulator. In order to change the device from a non-conducting to a conducting state it is essential to apply a high voltage causing soft breakdown of the tunnel barrier and this process is known as forming. Without the forming process, switching behavior was not observed between the 0 and 2 V range. The forming process is necessary for most RS devices to show reproducible switching behavior.[55, 86] The forming voltage for the system was around 12 V as shown in Figure 3.2(a), with a current compliance of 35 mA. Applying a high voltage induced ionic motion, leading to non-reversible structural changes in oxides and making granular multilayers conductive. The current compliance was required to prevent the device from non-reversible ionic motion. Immediately after the forming process, the *I-V* characteristics were obtained in the voltage range of 0 to 2 V, keeping the current compliance at 35 mA. The range of measured currents was larger than that from theoretical calculations

(shown later) because of the larger size of the electrodes. The system demonstrates a typical characteristic of threshold RS, as shown in Figure 3.2(b). The interesting part was that only a small part of the structure might be contributing to the switching process as had been reported in similar systems where electrons flow between nanodots separated by insulating barriers.[85, 87, 88]

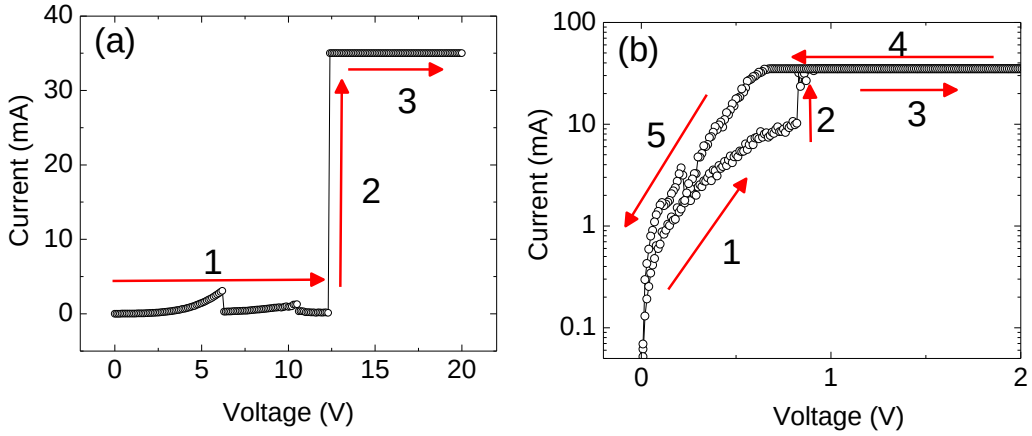

Figure 3.2 (a) *I-V* characteristics of the device during the forming process. (b) Threshold resistive switching behavior due to charge accumulation in the granules.

The effect of magnetic field on switching behavior was studied by applying the magnetic field parallel to the direction of the average current in the film plane. It was clear from Figure 3.3(a) that the switching voltage (V_t), at which the resistance state changed from a HRS to a LRS, decreased with an increase in the magnetic field. For example, V_t decreased from 0.83 V at zero field to 0.42 V at 52 mT, as shown in the Figure 3.3 (c). This field-dependent modulation of the junction current had not been observed in the magnetic granular system, but was reported in a 83 nm NiO film.[89] With the presence of oxygen vacancies in NiO, the Ni rich centres act as magnetic granules in an oxide environment of NiO and our proposed theory below may be used to explain the observed magnetic field dependence.

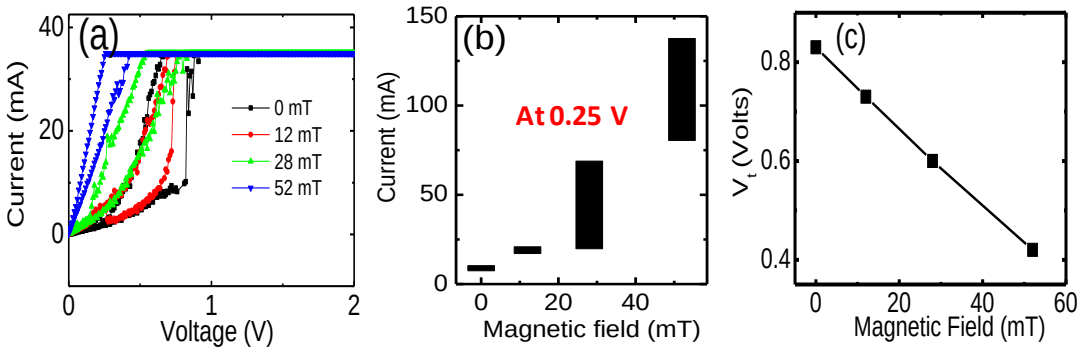

Figure 3.3 (a) Experimental *I-V* characteristics of threshold switching for different external magnetic fields. (b) The conductance ranges at 0.25 V, determined by connecting two conductance data which were obtained from the forward and backward bias sweeps. (c) This shows how the switching voltage (V_t) changes with the external magnetic fields.

3.3.3 Effect of forming

In order to see the changes in the structure of the film after the high voltage forming process, we used TEM images. Although we could see structural differences in the images as shown below in Figure 3.4(b), it was very difficult to tell if these changes are responsible for the transition to the conducting state. The C-AFM images were clearer though, with very sharp changes in the current scale after the foming process as well as the appearance of conducting channels in the current-map image, as shown below in Figure 3.4(d).

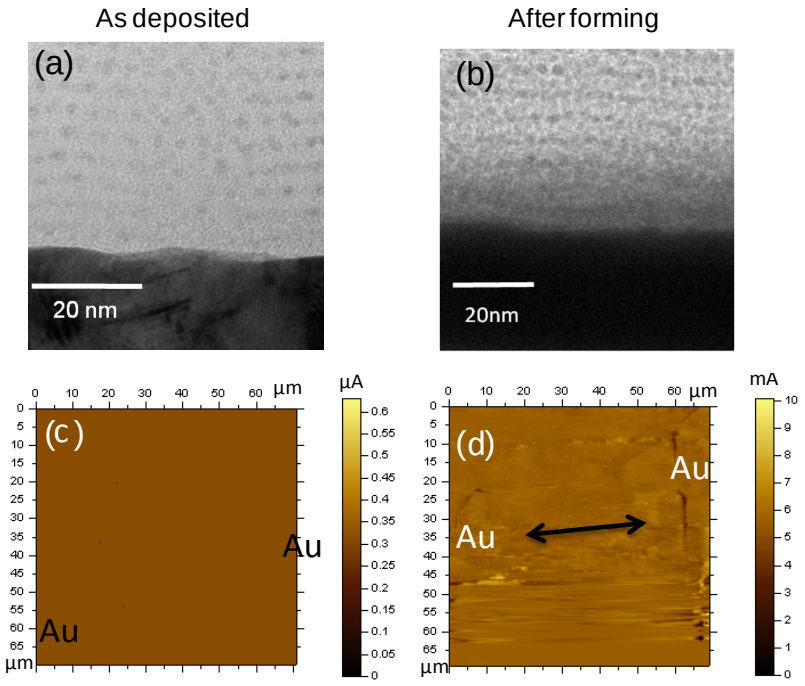

Figure 3.4 TEM images of the granular structure (a) before and (b) after forming. The structure was affected by the high voltage bias application. C-AFM images (c) and (d) after forming indicates transition to a conducting state after high voltage application. The contact pad positions are indicated by Au.

3.4 Theoretical model

3.4.1 Model parameters and density of states (DOS) calculation

In order to observe the RS in granular multilayers, it was required to apply high voltages of about 10-20 V. This is the so-called forming process without which the device remains an insulator. Therefore, we describe a formed granular multilayered structure by considering a simple tight-binding like model of a two-dimensional (20 by 15) cluster with classical localized moments $\boldsymbol{M}_i$ which mimic magnetic granules. A magnetic granule was represented by a single site. Since the device was formed and was in a conducting state, there was an overlap between the wave functions of the nearest-neighbour granules; therefore, conduction electrons can flow between the nearest-neighbour sites. We described the transport properties of

magnetic granular multilayers with a two-dimensional model because the main contribution to the current through the magnetic granular multilayers came from the first layer of magnetic granules. We modeled the field dependence of the directions of the localized moments with the Langevin function. The magnetic moments were randomly oriented in the absence of the external magnetic field and became aligned towards the direction of the field at high magnetic fields close to the saturation field H_s. The localized moments were coupled with conduction electrons through the local exchange interaction, J. The two-dimensional granular cluster was coupled with two non-magnetic leads. The Hamiltonian of the system had the form:

$$\hat{H} = \hat{H}_C + \hat{H}_L + \hat{H}_R + \hat{H}_{CL} + \hat{H}_{CR} + H.c., \tag{3.1}$$

where $\hat{H}_C$ was the Hamiltonian of the uncoupled cluster, $\hat{H}_{L/R}$ was the Hamiltonian of the left/right lead, and the term $\hat{H}_{CL/CR}$ described the coupling of the granular cluster to the left/right lead. $\hat{H}_C$ had the form:

$$\hat{H}_C = U\sum_{i,\sigma}\hat{c}_i^{\dagger\sigma}\hat{c}_i^{\sigma} + t\sum_{i,j,\sigma}\hat{c}_i^{\dagger\sigma}\hat{c}_j^{\sigma} - J\sum_{i,\alpha,\beta}\hat{c}_i^{\dagger\alpha}(\sigma_{\alpha\beta}\cdot M_i)\hat{c}_j^{\beta}, \tag{3.2}$$

where U was the electrostatic potential which was equal to $U_{0(ch)}$ if the granules were uncharged (charged), t was the spin-independent effective hopping integral between the nearest-neighbour granules, $\hat{c}_i^{\dagger\sigma}$ and $\hat{c}_i^{\sigma}$ were the creation and annihilation operators of the conduction electron with spin σ on site i, and $\sigma_{\alpha\beta}$ was the vector of Pauli matrices.

We calculated the electric current I through the system when a voltage V was applied across the device. Our calculations were based on Non-Equilibrium Green Functions formalism. The details of the approach could be found elsewhere.[90] First we diagonalized $\hat{H}_C$ and found the retarded Green function of the uncoupled cluster g^r.

Next we found the retarded Green function of the coupled system by solving the Dyson equation:

$$G^r = g^r + g^r \Sigma_L^r G^r + g^r \Sigma_R^r G^r, \tag{3.3}$$

where $\Sigma_{L/R}^r$ was the retarded self-energy due to connection of the cluster to the left/right lead. We assumed that $\Sigma_{L/R}^r$ was independent of energy. The final expression for the charge current became:

$$I = \frac{e}{h}\int d\varepsilon [f_L(\varepsilon) - f_R(\varepsilon)] Tr[G^a \Gamma_R G^r \Gamma_L], \tag{3.4}$$

where G^a was the advanced Green functions of the coupled system, $\Gamma_{L/R} = i(\Sigma_{L/R}^r - \Sigma_{L/R}^a)$ and $f_{L/R}$ was the Fermi-Dirac distribution functions in the left/right lead.

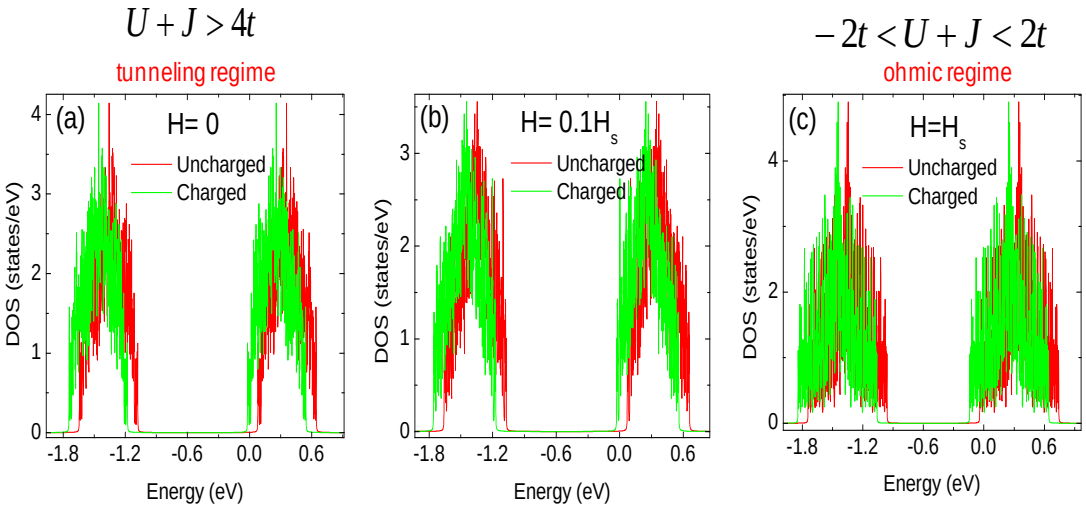

Figure 3.5 Density of states (DOS) with different values of external magnetic field (H), for both uncharged and charged conditions at H = 0 (a), $H = 0.1H_s$ (b), and $H = H_s$ (c). The Fermi level was at 0 eV. The valence band was completely filled for all cases. After charging, the center of the conduction band moved closer to the fermi level. The occupation of the conduction band depended on the magnetic field. At $H = H_s$ the conduction band was partially filled.

In the calculations we used the parameters U_0 = -0.5 eV, U_{ch} = -0.6 eV, t = 0.1 eV, J = 0.85 eV, and $\Gamma_L = \Gamma_R$ = 0.1 eV. The ratio of J/t was an important parameter in

our calculations. We chose $J/t >> 1$ because the concentration of magnetic granules in granular multilayers was small and hence, the effective hopping integral (t) was small. In this case there were two well-separated bands. In Figures 3.5(a)-(c) we plotted the density of states of the granular system at different values of the magnetic field. The Fermi level was at 0 eV. The valence band was completely filled and the occupation of the conduction band depended on the magnetic field. It was clear from Figures 3.5(b) and 3.5(c) that the bandwidths increased with the magnetic field. When the magnetic granules became charged, the shift of the electrostatic potential led to the shift of the density of states. According to the results of Figures 3.5(a)-(c), one could expect a transition from tunneling towards the ohmic regime depending on the charging status at small magnetic fields ($H = 0$ or $H = 0.1H_s$), while the system was in the ohmic regime at H_s, regardless of the charging level.

3.4.2 *Magnetic field dependent I-V characteristics*

In Figure 3.6, we show the *I-V* characteristics at different values of the magnetic field. We set the compliance current, which was a parameter in our model because higher currents can induce ionic motion. Taking the ionic motion at high voltages into account was beyond the scope of the calculations used. The switching voltage significantly decreased with an increase in the magnetic field. The range of measured currents was larger than the theoretical range because of the larger size of the electrodes. While the theory considers a 20 ×15 matrix of Co granules, in experiments we have millions of granules in between the huge contact ($80\times80\ \mu m^2$) pads.

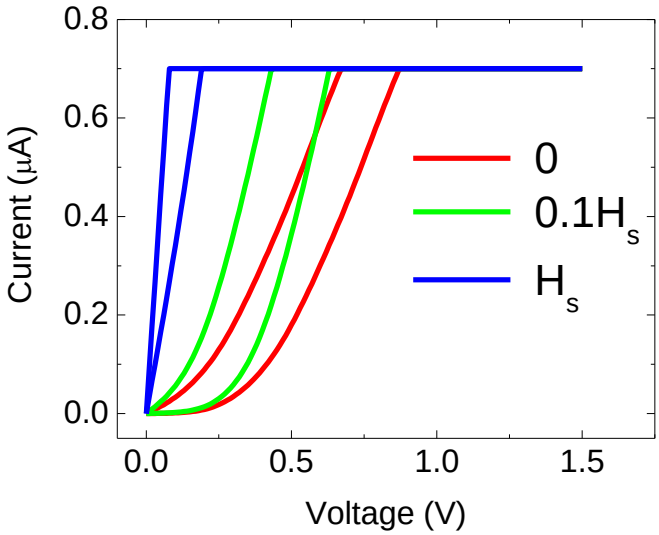

Figure 3.6 Calculated *I-V* characteristics of the RS system for different *H*. At a fixed magnetic field the system changes from a HRS to LRS when the voltage was swept from 0 to 1.5 V.

The underlying mechanism was the influence of the magnetic field on electron occupation of the conduction band. The conduction band of the system was almost empty without the magnetic field and the corresponding current at small voltages (< 0.1 V) was very small. When the voltage increased, the number of conduction electrons increased exponentially, which led to the rapid increase in the current. At higer voltages (> 0.5 V), the conduction band was occupied and the current dependence on the voltage was linear. At higher voltage, the granules became charged and the change in electrostatic potential switched the system from HRS to LRS. As the voltage across the system was reduced, the granules retained the charge and this led to hysteresis in the *I-V* curves. The *I-V* characteristic at $0.1H_s$ was similar to that one at zero field but since the cluster's bandwidth became larger, a smaller voltage was needed to occupy the conduction band and the transition to the ohmic regime occured at a lower voltage (~ 0.3 V). At the saturation magnetic field, the bandwidth was large enough and the conduction band was partially occupied even at zero voltage. The

corresponding *I-V* characteristic at H_s indicated that the system was in the ohmic regime, regardless of the charging level of the granules.

3.5 Discussion

The magnetic field induced transition from tunneling to the ohmic regime occurred if the bottom of the conduction band in the absence of the magnetic field was above the Fermi level while at high magnetic fields, it moved below the Fermi level. For the two-dimensional tight-binding model, the critical magnetic field H_c, at which this transition occured, could be defined from $U + J - 4\tilde{t}(H_c) = 0$, where $\tilde{t}$ was the average effective hopping integral between the nearest-neighbour granules. The value of $\tilde{t}$ depended on the applied magnetic field. If we assumed that the effective hopping integral between the nearest neighbor granules *i* and *j*, t_{ij}, was proportional to the tunneling probability of the conduction electron to tunnel between granules *i* and *j* and the spin polarization of granules was 100%, then the electron hopping could be written as $t_{ij} = t(1 + \cos\theta_{ij})/2$, where θ_{ij} was the angle between the magnetic moments of granules *i* and *j*.[53] At the saturation field, magnetic moments of all granules were aligned towards the direction of the field and $\tilde{t}(H_s) = t$. In the absence of an external magnetic field, the magnetic moments of granules were randomly oriented and $\tilde{t}(0) = t/2$. The value of $U + J$ and t were important parameters in our calculations. The system was always in the tunneling regime if $U + J > 4t$, and the system were always in the ohmic regime for $-2t < U + J < 2t$. Experimentally, it would be possible to control the $U + J$ parameter by choosing different oxides (different *U*) and different magnetic materials of granules (different *J*). The *t* parameter could be controlled by fabricating granular multilayers with different concentrations of magnetic granules. Larger values of *t* corresponded to granular multilayers with higher

granular concentrations. In order to prove the universality of our proposal, we tried a similar experiment in the [NiO (3 nm)/Co (0.5 nm)]$_{10}$ multilayer system and successfully controlled the switching voltages with an external magnetic field [Figure 3.7].

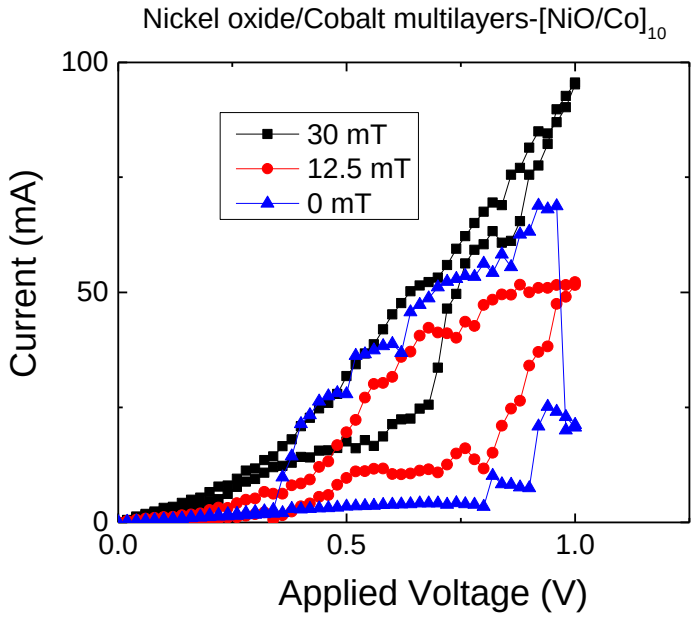

Figure 3.7 I-V characteristics of a NiO/Co granular multilayer system at different magnetic fields. At higher magnetic fields, the switching voltage could be reduced in this system as well.

3.6 Conclusion

In conclusion, we observed the hysteretic resistive switching behavior in Co/Al_2O_3 granular multilayers. The switching was attributed to electron accumulation in the Co granules and the switching voltage could be modulated with an external magnetic field. We proposed a theoretical model based on a self-trapped electrons mechanism to explain the magnetic field dependence of threshold resistive switching in the magnetic granular system. Our calculations showed that the switching voltage could be significantly decreased by increasing the magnetic field for a certain range of model parameters. In the next chapter, we will study how the electric field application changed the magnetization of the Co granules in the same system.

Chapter 4 : Electric field induced magnetization changes in Co/Al_2O_3 granular multilayers

4.1 Motivation

In the previous chapter we studied the electrical switching behavior in Co/Al_2O_3 granular systems with an external magnetic field. Whether the magnetic moment of the Co granules is affected during the switching process is a very pertinent question to investigate and answer. At the same time it becomes very interesting to explore the possibility of reversible magnetization switching or changes in this system with electric fields for energy-efficient magnetic data storage applications.

In this chapter, we have studied the effect of electric fields on the magnetization of Co/Al_2O_3 granular multilayers. We observed that the application of a large electric field induced oxygen migration from Al_2O_3 into the Co granules, which caused the granule magnetization to either increase or decrease irreversibly as a result of redistribution of both spins and charges, depending on the oxygen content. These observations were in line with self-consistent Hartree-Fock-based simulations of the different oxidation states of the Co granules. In the presence of a small in-situ electric field (in the SQUID system, during M-H measurement it was possible to apply in-plane electric field across the samples surface), the net magnetization was reduced in a reversible way with an increase in the field strength. Electric field changes the position of the Femi level relative to the majority and minority (3*d*) bands, which in turn changes the magnetization of the system.

4.2 Introduction

Electric field control of magnetism has aroused significant interest for future electronics as well as energy-efficient magnetic data storage.[91] Granular magnetic films provide interesting routes for novel physics and device applications by tailoring both the individual and collective properties of the nano-magnets.[92, 93] For example, incorporation of magnetic nanoparticles in the barrier of magnetic tunnel junctions has been theoretically predicted to demonstrate a very high magnetoresistance[54] and higher order tunneling effects have also been experimentally observed in similar systems.[85, 94] In terms of applications, resistive switching (RS) is an interesting phenomenon that is also observed in magnetic granular films.[95, 96] Typical RS systems involve a high voltage forming process in order to observe the switching effect. Such a high electric field during the forming process may affect the oxidation state, hence the magnetization of magnetic granules. There have been several recent studies on oxygen migration induced by high electric fields in thin film RS systems. While Yoshida et al. relate oxygen migration to the two resistance states in NiO films,[97] another recent study shows low-bias induced oxidation of Pt electrodes in HfO_2-based RS systems using X-ray photoelectron spectroscopy (XPS).[98] However, in a magnetic granule based system, the magnetization change due to electric fields has not been studied.

Here we have investigated the effect of electric fields on the magnetization of Co granules in the sputter deposited Co/Al_2O_3-based magnetic granular system. We have provided experimental and theoretical results to show changes in the magnetization of the granules as a result of oxygen migration induced by electric fields and this could lead to either enhancement or reduction in the saturation magnetization. We also showed systematic and reproducible changes in the net magnetic moment of the system using in-situ electric fields in a superconducting quantum interference

device (SQUID), which was due to changes in the relative occupancy of the majority and minority 3*d*-orbitals of Co granules.

4.3 Sample preparation

The Co/Al_2O_3 magnetic granular system was fabricated in an ultra-high vacuum (10^{-9} torr) magnetron sputtering chamber using dc and rf sources for Co and Al_2O_3, respectively. Ten layers of [Al_2O_3 (4 nm)/Co (0.5 nm)] were deposited on Si (100) substrates with a 400 nm thick thermally oxidized SiO_2 layer and the structure was subsequently capped by a 4 nm Al_2O_3 layer. Figure 4.1(a) shows the cross-sectional transmission electron microscope (TEM) image of Co/Al_2O_3 granular multilayers. The Co nanoparticles were clearly visible, embedded in an Al_2O_3 insulating matrix. The inset of Figure 4.1(a) is a schematic of the system used in this study. Electrical contact pads were formed by thermally evaporated Cr (5 nm)/Au (100 nm) and an electric field was applied between the pads. The sample size was ~ 5 mm × 5 mm. M-H loop measurements were carried using SQUID. A region where an electric field had been applied would be referred to as a formed region.

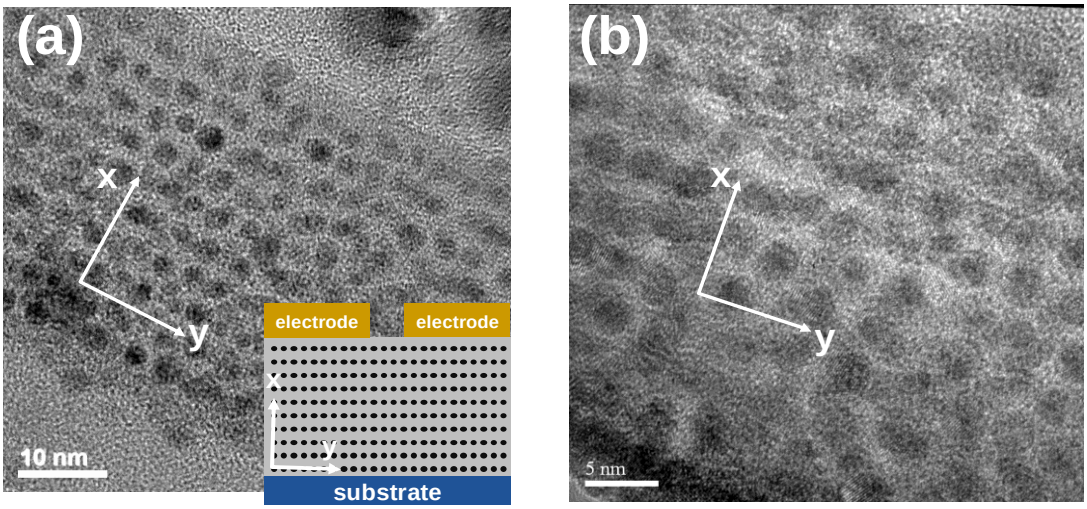

Figure 4.1 (a) Cross-sectional TEM image of the Co/Al_2O_3 multilayer system (as deposited). The dark spots are Co islands and the lighter region is the Al_2O_3 insulating matrix. A schematic representation of the multilayer system is shown in the inset. (b) TEM of the multilayers after applying a high electric field along the plane of the film.

4.4 M-H loop measurement (SQUID)

Figure 4.2 shows the M-H loop measurements of four different samples. As seen from Figure 4.2(a), the net saturation magnetic moment of the sample #1 was enhanced after the entire region was formed. However, sample #2 in Figure 4.2(b) showed a reduction in the net moment after forming the entire region. A 4.2 mV/nm electric field was applied for both the samples across Cr/Au contact pads deposited all over the sample. Figures 4.2(c) and 4.2(d) show the results for the samples for which SQUID analysis was done after forming four different regions of the sample. Initially, the M-H loop was measured as-deposited. The sample was then divided into four sections and SQUID measurements were performed after forming each of the four regions. It was observed that the magnetization fluctuated as different regions were formed, which can be observed in random changes of magnetization. SQUID has been reliably used by Chen et al. to demonstrate the possibility of magnetization enhancement of ~ 100% in α-Fe_2O_3-based oxide systems.[83] We also confirmed the

reliability of the SQUID results by carrying out repeated measurements on the same sample. The inset of Figure 4.2(d) shows the M-H loops for a sample, repeated four times without applying any bias voltage. For each measurement, the sample was taken out from the SQUID machine and remounted in the sample holder in order to check the alignment issue. The value of magnetic moment for this sample varied from 128.4 to 131.4 μemu when repeated, indicating a maximum change of 2.3%. On the other hand, changes in the saturation magnetic moment of the samples after the application of electric field was as high as 32%, as shown in Figure 4.2(b).

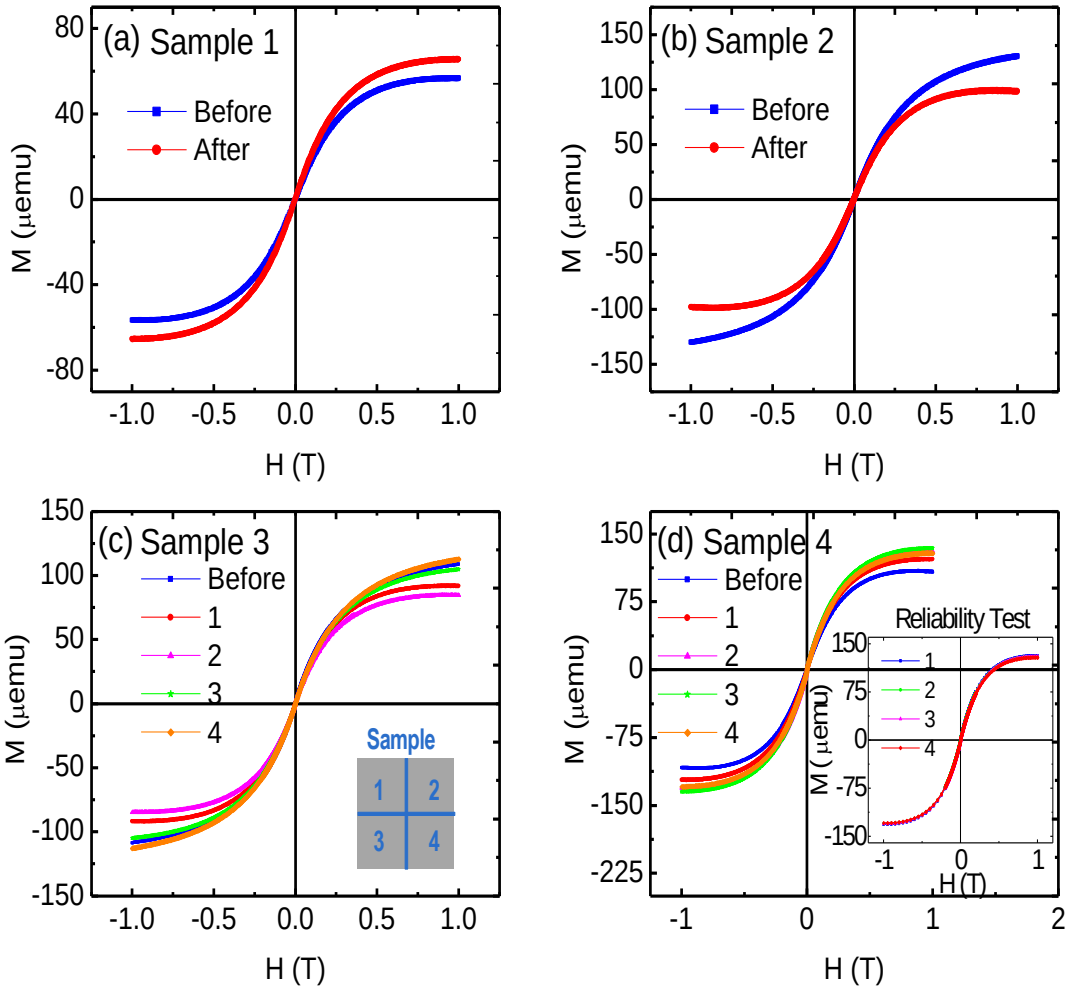

Figure 4.2 M-H loops using SQUID showing the changes in magnetization for different samples before and after application of electric field. (a) Net magnetic moment for the sample increased after bias application. (b) Net magnetic moment for the sample decreased after bias application. In (c) and (d), samples were divided into four regions and the M-H loop was measured after an electric field was applied to each region. The net magnetic moment of the samples fluctuated as the different regions were formed. The inset in (d) shows a reliability test of SQUID by repeating the measurement of the same sample for four times at zero bias. Note that the sample #1 had a smaller size than others.

4.5 Co granule oxidation state analysis using XPS

In order to understand the mechanism governing the changes in Co magnetization, we analyzed the oxidation state of Co granules before and after bias

application using XPS. Figure 4.3(a) illustrates the depth profiles of as-deposited Co-Al_2O_3 multilayers, showing clear alternate oscillations of Co_{2p} and O_{1s} peaks. Figures 4.3(b)-(d) show the O_{1s} spectrums for the Al_2O_3/Co multilayers at a depth corresponding to the first Co layer from the top surface. O_{1s} peaks have been used for the calculation of relative proportions of different species in various materials and systems, and the analysis of 2*p* spectra for transition metals is usually more complex.[99-102] We resolved the O_{1s} spectrum into Co-O and Al-O bonding peaks as their binding energies have been observed to be different in similar systems (Co-Al-O alloys) deposited by sputtering.[103] The experimental spectra was corrected by Shirley background and then deconvoluted using two Gaussian distributions corresponding to different O_{1s} states – one of the peaks came from Co-O bonding and the more dominant one was from Al-O bonding. The percentage contribution of each component was determined by integrating the associated Gaussian curve. The Al-O peak was at ~531.6 eV and the Co-O bonding peak was ~530.4 eV for the fits. The fitted curves obtained from the combination of the two Gaussian distributions matched well with the experimental results.

For the as-deposited structure, it was found that Al-O bonding contributed mainly to the O_{1s} peak. Similar analyses were also done for the same sample at two different regions corresponding to magnetization enhancement and magnetization reduction, as shown in Figures 4.3(c) and 4.3(d) respectively. After the bias application, the Co-O bonding contribution to the O_{1s} spectrum increased from an initial 10% to approximately 30-35%. The cross-sectional TEM of a formed region is shown in Figure 4.1(b). The relatively poor contrast of granules is ascribed to the oxidation of Co granules. A similar effect of bias-induced oxygen migration has been observed recently, where the metal electrode was oxidized at the metal/oxide interface

upon application of an electric field of a few mV/nm across HfO_2.[98] The electric field we applied was also of the same order ~ 4.2 mV/nm for 50 μm separated pads.

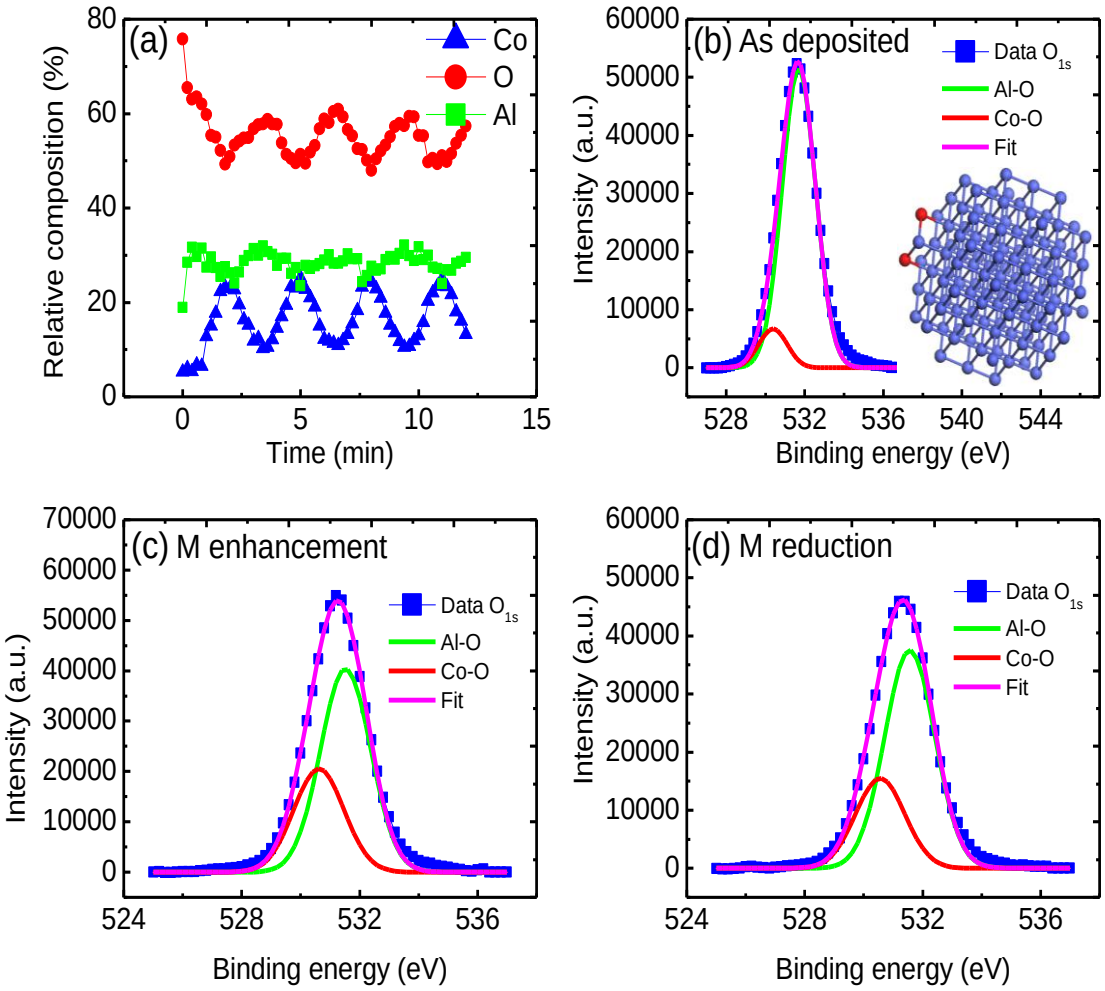

Figure 4.3 (a) XPS depth profiles of the multilayer system showing alternating oscillation peaks of Co_{2p} and O_{1s}. (b) O_{1s} spectra of the layers at the first Co layer from as-deposited sample. (c) Region with enhanced magnetization. (d) Region with reduced magnetization. The inset in (b) shows a Co granule with 2 O atoms used in the calculations. Co atoms are blue and O atoms are red.

Finite electric fields can add or remove O atoms from the Co surface, thus changing the oxidation state. Since the O is an acceptor of electrons, addition of O would remove electrons from the Co granule. This process is not monotonous, since the available electrons will be redistributed within the granule in order to minimize the

energy. The net effect could be either increasing or decreasing the magnetic moment of the granule.

4.6 Theoretical model

In order to understand the relationship between the oxygen content and the magnetic moment of a Co granule, we considered a theoretical model of Co granules with impurities attached to the surface. The Co granules were 1.5 nm in diameter (123 Co atoms) and a range of 0 to 9 O atoms were attached to the surface. For instance, a granule with 2 O atoms is shown in the inset of Figure 4.3(b). Both Co and O atoms were represented in a tight-binding single-orbital model, where the on-site energy of the Co atom represented the partially filled 3*d* states and the on-site energy on the O atoms represented the partially filled 2*p* states which served as electron acceptors. The atoms were on a simple cubic lattice and only the first nearest neighbors were considered.

The calculatons were based on the Hubbard model where we solved for the charge distribution and magnetic moment self-consistently within the Hartree-Fock approximation.[104] The Hamiltonian of a granule consists of three terms:

$$H = H_0 + H_{imp} + H_{cpl} \tag{4.1}$$

where the terms represent the Co granule, O impurities, and the coupling between them respectively. The Hamiltonian of Co atoms in a granule was:

$$H_0 = t_0 \sum_{i,j,\sigma} c_i^{\dagger\sigma} c_j^{\sigma} + \sum_{i,\sigma} (\varepsilon_0 + U_0 \langle n_i^{-\sigma} \rangle) n_i^{\sigma} \tag{4.2}$$

where $c_i^{\dagger\sigma}$ and c_i^{σ} were the creation and annihilation operators of electrons with spin σ, $n_i^{\sigma} = c_i^{\dagger\sigma} c_i^{\sigma}$ was the operator of number of electrons with spin σ, and $\langle n_i^{-\sigma} \rangle$ was the average number of electrons with spin $-\sigma$. The indices *i* and *j* run over the Co sites, t_0 was the electron hopping integrals between nearest neighbor Co atoms, U_0 was the

intersite Coulomb interaction, and ε_0 was the spin-independent part of the on-site energy used as a reference. The impurity Hamiltonian was $H_{imp} = \varepsilon \sum_{l,\sigma} n_l^{\sigma}$, where the indices l label O atoms. We neglected the Coulomb interaction at the impurity sites, thus the oxygen energy levels were lower than that in the Co granule. Finally, the last term H_{cpl} represented coupling between the Co and O atoms:

$$H_{cpl} = t_{cpl} \sum_{i,l,\sigma} (c_i^{+\sigma} c_l^{\sigma} + c_l^{+\sigma} c_i^{\sigma}), \tag{4.3}$$

where t was the electron hopping integrals between an O atom and its nearest neighbor Co atoms. The model parameters were chosen to be U_0 =10 eV, $t_0 = t$ =1 eV. For the onsite energy $\varepsilon = \varepsilon_0 = 0$, due to electron correlations, the energy states on the impurity were lower and served as acceptors. We considered 3/2 filling which approximately corresponded to the 3d filling in the Co atom. Since the O orbitals were unoccupied, the total number of electrons in a granule, $N_{el} = \frac{3}{2} N_{\mathrm{Co}} = 184$, was not changed when the O impurities were added. The magnetic moment of a granule is proportional to the difference between the average number of electrons with opposite spins:

$$M_0 = \mu_0 \sum_r \left(\langle n_r^{\uparrow} \rangle - \langle n_r^{\downarrow} \rangle \right) \tag{4.4}$$

which was found self-consistently. We performed the Hartree-Fock calculations at low temperature. We started with 200 different randomly distributed initial occupation numbers in order to ensure that we found the global minimum. At a moderately large U_0, the majority of electrons on the pristine Co granule were paired and the magnetic moment was $M_0 = 8$. Calculations with additional O impurities showed that the magnetic moment M_0 could be either increased or decreased, depending on the configuration. For certain configurations (e.g. 1 or 6 O atoms), the magnetic moment of a Co granule increased up to 10. For other configurations (e.g. 2 O atoms), it can

decrease down to two. The results are summarized in Table 4.1. The underlying mechanism of this magnetization change was the charge and spin redistribution on the granule due to the shifting of charge to the impurity. Due to hybridization between the O and Co atoms, O atoms could accommodate the charge from Co atoms, leading to spin redistribution in the granule. In the limit of infinite U_0, all spin-up levels would be occupied yielding $\langle N^{\uparrow} \rangle = 123$, $\langle N^{\downarrow} \rangle = 184 - 123 = 61 \Rightarrow M_0 = 62$ for the Co granule without impurities. Oxygen impurity would accommodate two electrons, thus the magnetic moment would be increased by $2N_{imp}$. If U_0 was finite, the mechanism would be more complicated. For our choice of parameters, $M_0 = 8$ which was much smaller than the maximum possible value of 62. In this case the charge redistribution due to impurities may lead to either an increase or decrease in the granule's magnetic moment, which was in agreement with the experimental data.

N_{imp}	0	1	2	3	4	5	6	7	8	9
M_0	8	10	2	4	4	4	10	4	8	8

Table 4.1 Magnetic moment (μ_B) of a cobalt granule for different number of oxygen impurities.

4.7 Magnetic moment with in-situ electric field in SQUID

The addition of O atoms to magnetic granules is an approach to change the occupancy of the 3*d* states and hence, the magnetic moment; however, it is an irreversible process. For device applications, a reversible approach based on electric field control of the 3*d* states has garnered widespread attention recently.[105, 106] In order to see the reversible magnetization changes in the presence of a small electric field, we also carried out SQUID measurements with a simultaneously applied bias voltage across the sample. There is a recent report of similar measurements with an in-situ

electric field.[107] The magnetization of the system was found to be reduced systematically and reproducibly, as the electrical field in-plane to the surface gradually increased. Figures 4.4(a) and (b) show the results for the two samples, where the value of the magnetic moment was averaged over a period of 200 s with a constant external field of 1 T. The measurement was repeated four times with increasing and decreasing electric fields (1st and 2nd sequence) as well as with negative values of electric fields (3rd and 4th sequence). For sample #5 the maximum electric field was around 0.4 mV/nm while for sample #6 it was around 0.1 mV/nm. In order to confirm the reliability of the measurements, a similar measurement was carried out for a sample with 20 nm Al_2O_3 and no voltage dependence was observed. The changes we observed (~2%) were comparable to changes predicted in thin films[105] for a similar applied level of electric field. The small change of 2% could be attributed to a small size of the formed region. Moreover, the magnitude of the applied electric field was also very small. Nevertheless, our experiment provided direct evidence to show that electric fields could change the magnetization of Co granules in an Al_2O_3 matrix, and the changes in the occupancy of the 3*d* orbitals in Co atoms due to the electric field was responsible for the observation.[105, 106] In this case, oxygen migration was not primarily involved due to a smaller electric field.[108, 109] Therefore, the change of the magnetization was reversible with the bias, as shown in Figure 4.4.

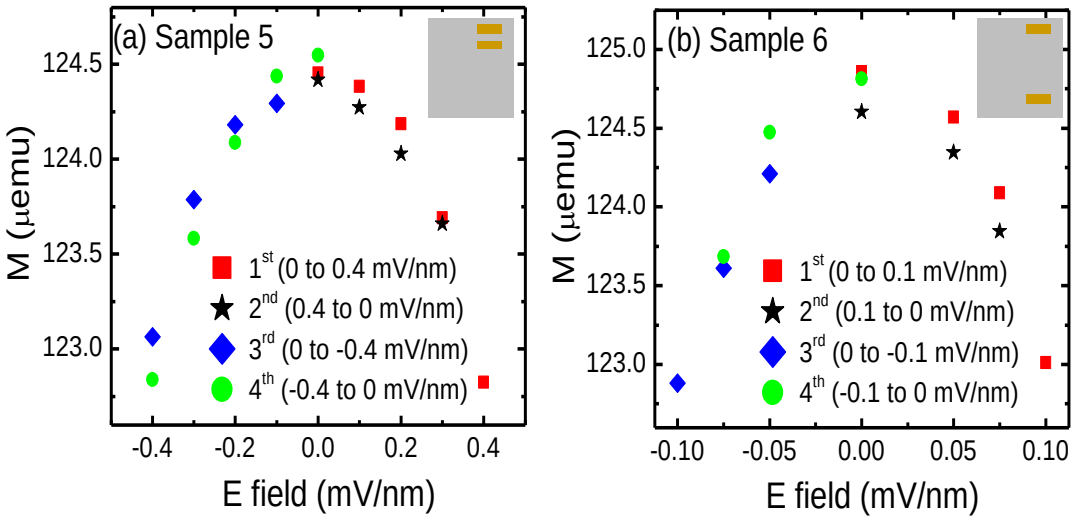

Figure 4.4 Magnetic moment versus applied electric field for two samples. The magnetic moment gradually reduces as the electric field increases, and the changes are reproducible (1^{st} to 4^{th} steps indicate the sequence of measurements). The contact pads are indicated in the insets.

4.8 Conclusion

In conclusion, we showed the effect of electric field on the magnetic moment of Co granules in an Al_2O_3 matrix. With a relatively large electrical field, the migration of O atoms into the Co granules could change the magnetic moment in an irreversible manner. The magnetization could increase or decrease, depending on the detailed bonding configuration between O and Co. On the other hand, the magnetic moment in the presence of a small in-situ electric field was systematically reduced as the field increased. This work opens up the possibility to control the magnetization by electrical fields in magnetic granular systems.

Two interesting effects have been studied in the magnetic granular system. The RS in this system provides a link between resistive and magnetic random access memories, though it requires further research and development. Electric field induced magnetization change in this system provides another example of energy-efficient magnetic data storage, which is fast becoming a popular research focus for many

memory enthusiasts. After studying the magnetic granular system, we explore another spin-dependent tunneling system that already has a valuable market position as well as academic research interest – the magnetic tunnel junction (MTJ).

Chapter 5 : Effect of substrate bias on structural and compositional properties of AlO_x-based magnetic tunnel junctions

5.1 Motivation

After investigating interesting effects in magnetic granular systems in the previous two chapters, we shift our focus to magnetic tunnel junctions (MTJs), which are used in the practical applications as the read heads of hard disc drives (HDD) and memory elements in magnetic random access memory (MRAM).[31, 110] Though MTJs have been commercialized, the mechanisms involved as well as the exact structural conditions required for a high tunnel magnetoresistance (TMR) value are not completely clear. Recently, TMR close to 1000% has been reported using MgO tunnel barriers.[37] Crystalline barriers such as MgO enable huge TMR through coherent tunneling of electrons even using conventional ferromagnetic (FM) elements and alloys. Interface properties such as stoichiometry as well as the crystallinity play a very important role and can be tuned to change the TMR significantly.[111, 112]

5.2 Introduction

Magnetron sputtering has developed rapidly over the last two decades to the point where it has become established as the process of choice for the deposition of a wide range of industrially important coatings, including MTJs and HDD media. Magnetrons make use of the fact that a magnetic field confined parallel to the target surface can constrain secondary electron motion to the vicinity of the target.[113] This

has helped to overcome limitations such as low deposition rates, low ionisation efficiencies in the plasma, and high substrate heating effects associated with the DC or RF sputtering process.

The application of substrate bias during deposition causes bombardment of ions on the growing film and variation of the bias voltage varies the energy of bombarding ions. The energy of ion bombardment during thin film growth strongly influences the microstructure of the coating. High energy ion bombardment induces coating densification but also results in an increase in residual compressive stress and hardness.[114] A recent paper shows the effect of substrate bias during MgO deposition on CoFeB/MgO-based MTJs.[115] The authors show an increase in TMR and a reduction in the resistance area (RA) product with the application of bias to the substrate, and explain the reason to be enhanced MgO (001) growth, which is required for high TMR. We studied the effect of substrate bias during the deposition on the properties of AlO_x-based MTJs by magnetron sputtering.

The aim of substrate bias application during deposition is to see the effect on the defect density in ultrathin tunnel barriers and the roughness at the FM/tunnel barrier interface that plays a very significant role in spin-dependent tunneling in an MTJ structure. Transport properties would help to understand the former while the TEM study would provide an idea of the latter. Effects on other properties like crystallinity as well as the composition of layers were also essential.

The effect of substrate bias during deposition on the properties of magnetron sputtered aluminium oxide-based magnetic tunnel junctions (MTJ) was investigated. Ge buffer layers (between substrate and MTJ structure) were used for MTJs. Transmission electron microscope (TEM) images clearly indicated that application of substrate bias during the deposition of MTJ layers [substrate/

buffer/IrMn/Co/AlO_x/NiFe/Cu] provided extremely smooth layers and flat interfaces (without annealing) in comparison to the layers deposited without bias. However, we hysteresis loops (magnetization v/s magnetic field M-H) obtained from an alternating gradient force magnetometer (AGFM) showed that IrMn deposited with a substrate bias was not effective in providing exchange bias. The reason was the change in the composition of IrMn with bias as shown by Rutherford backscattering (RBS) experiments. RBS for AlO_x showed a clear Ar peak with the application of substrate bias.

5.3 Deposition methods

The films were deposited in an ultra-high vacuum (10^{-9} Torr) sputter chamber. Atomic force microscopy was used to study the effect of substrate bias on film roughness and deposition rate. Germanium was deposited in a high vacuum (10^{-7} Torr) electron beam evaporator on Si/SiO_2 (thermally oxidized) substrates.

5.4 Effect on roughness and deposition rate for different layers in MTJ structure

As an initial study, the roughness and deposition rates for all the relevant layers in the structure were obtained. Atomic force microscopy was used to study the effect of substrate bias on film roughness and deposition rate. For most of the materials, both the parameters were reduced with the application of bias during deposition. The results were summarized in the table below. The deposition for all the materials was done on Si/SiO_2 substrates. The bias effect on the roughness of alloys, i.e. IrMn and NiFe, was of particular interest.

Material sputtered (deposition condition)	Substrate bias condition during deposition	RMS Roughness (nm)	Deposition rate (Å/s)
Cu (45 W, 3mT)	No bias	1.3	0.595
	20 W RF bias	1.3	0.542
IrMn (90 W, 3mT)	No bias	0.973	0.389
	20 W RF bias	0.473	0.138
NiFe (45 W, 3mT)	No bias	1.145	0.409
	20 W RF bias	0.928	0.366
Co (45 W, 3mT)	No bias	1.228	0.166
	20 W RF bias	0.390	0.147

Table 5.1 RMS roughness and deposition rates for different materials with and without substrate bias application during the deposition

5.5 Ge as an ultra-smooth buffer layer

Initially, due to the unavailability of ideal buffer layers such as Ta, several other options were tested. Electron beam evaporated Ge on Si/SiO_2 substrate was found to be extremely smooth. The RMS roughness was measured to be less than 3 Å. Ge buffer layers were tried for the MTJs in this study. The roughness of these films was characterized using an AFM while XPS was used for the chemical confirmation.

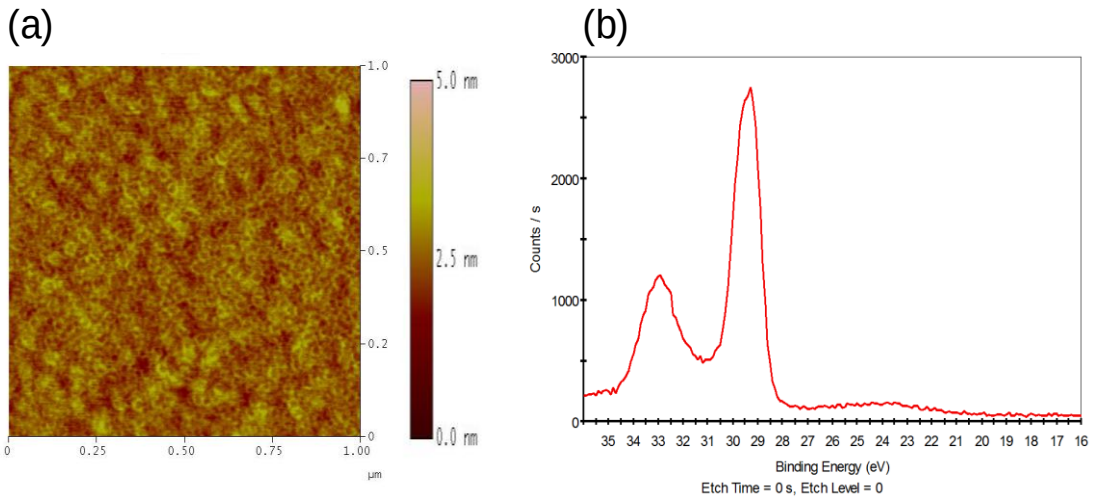

Figure 5.1 (a) AFM image of Ge on SiO_2 (RMS roughness 0.3 nm) and (b) XPS data showing the characteristic Ge peak with that of Ge oxide.

5.6 MTJ deposited and characterization methods

Two sets of the same structure were then deposited [Ge (40 nm)/IrMn (25 nm)/Co (3.5 nm)/AlO_x (3 nm)/Co (0.5 nm)/NiFe (5 nm)/Cu (2 nm)/Ge (5 nm)] – one with a 20 W RF bias applied to the substrate during the deposition for all the layers and no bias for any of the layers in the other. The aim of this study was mainly to investigate the effect of bias deposition on the properties of an MTJ (mainly the structure) and 20 W RF was the maximum bias power possible. Transmission electron microscope (TEM) was used to get the cross-sectional images of the two structures. The switching characteristics were obtained from an atomic force gradient magnetometer (AGFM). The effect of substrate bias on the composition of the antiferromagnetic IrMn and its crystal orientation was studied using Rutherford Backscattering (RBS) and X-ray diffraction (XRD) experiments, respectively. RBS was also used to study the AlO_x composition.

5.6.1 TEM analysis: structures deposited with and without bias

Cross-sectional TEM images for the two structures (without and with bias) are shown in Figure 5.2(a) and (b).

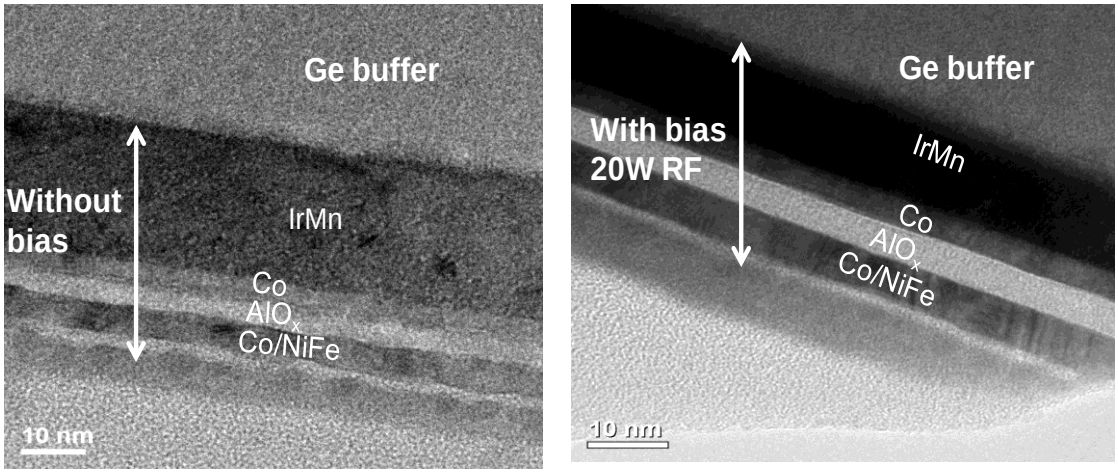

Figure 5.2 (a) Cross-sectional TEM image for MTJ [Ge (buffer) /IrMn/Co/AlO_x/Co/NiFe/Cu/Ge] without substrate bias. (b). Cross-sectional TEM image for MTJ with substrate bias

The effect of bias was to improve the uniformity of the layers and to ensure that the interfaces were flat. However, alternating gradient force magnetometer (AGFM) measurements for hysteresis loops (magnetization v/s magnetic field M-H) showed no switching for the layers deposited with a substrate bias of 20 W, while the layers deposited without any bias showed clear switching between the two magnetic layers.

5.6.2 TEM analysis: structures deposited with bias but different buffer layers

A Ge buffer layer was compared with a Cr/Au (40 nm with 0.6 nm RMS roughness) for the same structure deposited with a substrate bias. The structure with Ge buffer provides sharper interfaces compared to the one with Cr/Au buffer, as shown in Figure 5.3(a) and (b).

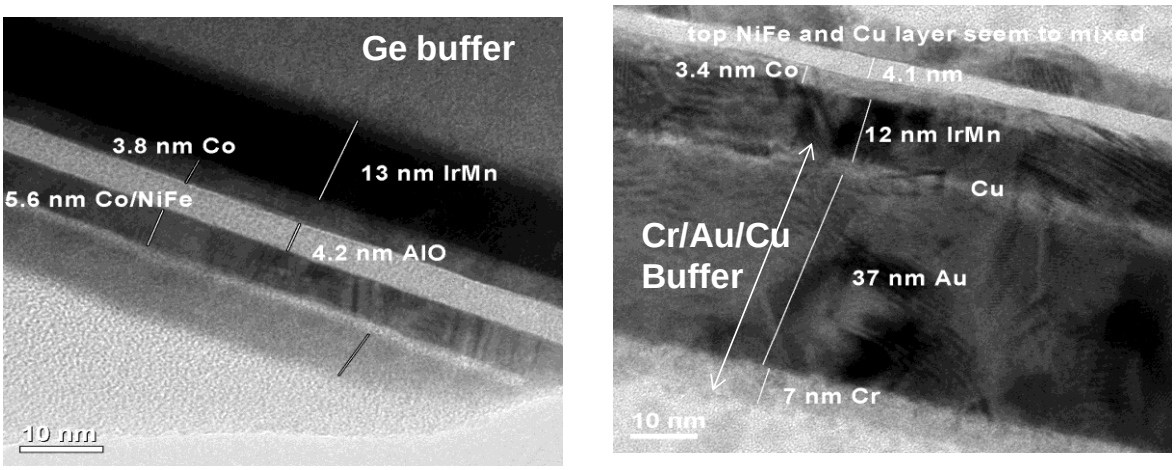

Figure 5.3 (a) Cross-sectional TEM image for MTJ [Ge (buffer) /IrMn/Co/AlO_x/Co/NiFe/Cu/Ge] with substrate bias. (b). Cross-sectional TEM image for MTJ [Cr/Au/Cu (buffer) /IrMn/Co/AlO_x/Co/NiFe /Cu/Ge] with substrate bias

5.6.3 Switching characteristics of the multilayers using M-H loops from AGFM

The M-H loops have been shown in Figure 5.4(a) and (b). It was clear from these loops that in layers deposited with a bias, there was no significant coercivity (H_c) difference between the FM layers to observe independent switching.

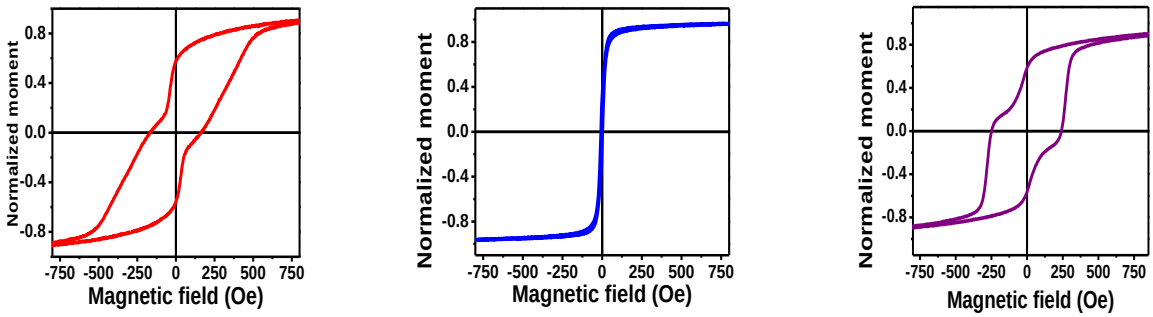

Figure 5.4 (a) AGFM M-H loops for the entire MTJ film structure when no bias is applied to any of the layers during deposition, (b) when bias is applied to each of the layers during deposition and (c) when bias is applied to all layers except IrMn.

The reason for the above observation was found to be the change in composition of the IrMn antiferromagnet layer. The compositional variation of a sputtered alloy with substrate bias had been studied elsewhere using both experiments and modelling.[116] Substrate bias has minimal effect on the coercivity of a Co-free

layer. A 5 nm Co layer had a coercivity of about 10 Oe, both with and without substrate bias during deposition. No unidirectional anisotropy was observed in Figure 5.4(a) since the deposition was done without an in-situ magnetic field.

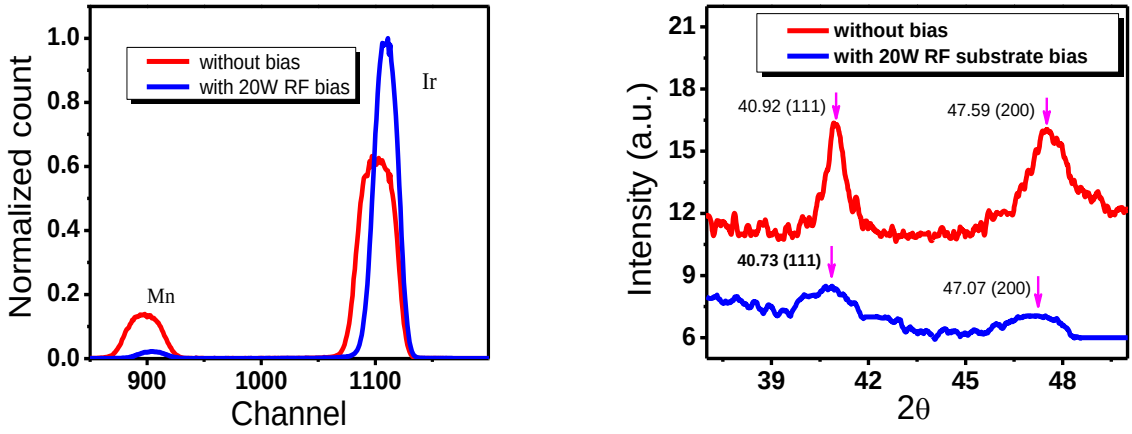

Figure 5.5 (a) RBS data for IrMn with and without substrate bias. (b) XRD signal for IrMn with and without substrate bias. Peaks broaden with bias.

5.6.4 IrMn properties

Although substrate bias improved the surface RMS roughness of IrMn by over 100% (from 9 Å to 4 Å) as observed from the AFM data, it turned out that its composition no longer made it an antiferromagnet to provide the exchange bias to the fixed layer in the MTJ. RBS experiments indicated that the IrMn composition changed from 34:66 to about 82:18 with substrate bias, indicating a preferential re-sputtering of Mn from the film (due to its lower atomic mass). The results are shown in Figure 5.5(a). XRD also showed a shift in the (111) peak of IrMn from 40.92˚ to 40.73˚, closer to the elemental Ir peak (40.044˚). At the same time, the IrMn (111) peak – which is critical to get a good exchange bias – was broadened with substrate bias as shown in Figure 5.5(b). A 5 nm film of Co, deposited (with an in-situ field) over IrMn deposited without substrate bias showed an exchange bias of about 150 Oe whereas, as shown in Figure 5.6(a) and (b), Co on IrMn deposited with substrate bias showed no exchange

bias. In order to observe the exchange bias effect, the composition of the IrMn is very critical.[117] The M-H loop for a structure with an applied bias for all layers except IrMn showed switching as shown in Figure 5.4(c).

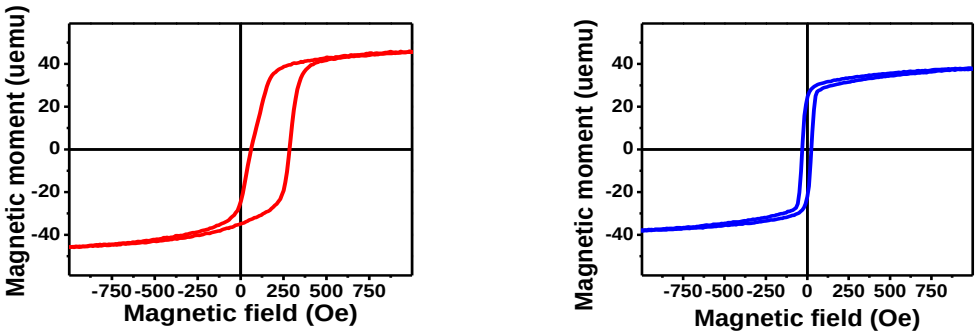

Figure 5.6 (a) AGFM signal showing a clear exchange bias (150 Oe) for IrMn/Co films when IrMn was deposited without bias. (b) AGFM signal showing loss of exchange bias in IrMn/Co structure when IrMn was deposited with substrate bias.

5.6.5 AlO_x properties

The RBS signal for AlO_x did not show any significant differences in the Al:O ratio (2:3) except a relatively higher Ar concentration with bias as shown in Figure 5.7(a) and (b). Even without a substrate bias, Ar was present in AlO_x and substrate bias provides an efficient way of tuning it. The presence of Ar and its role in ultrathin barrier layers in MTJ structures will be of special interest.

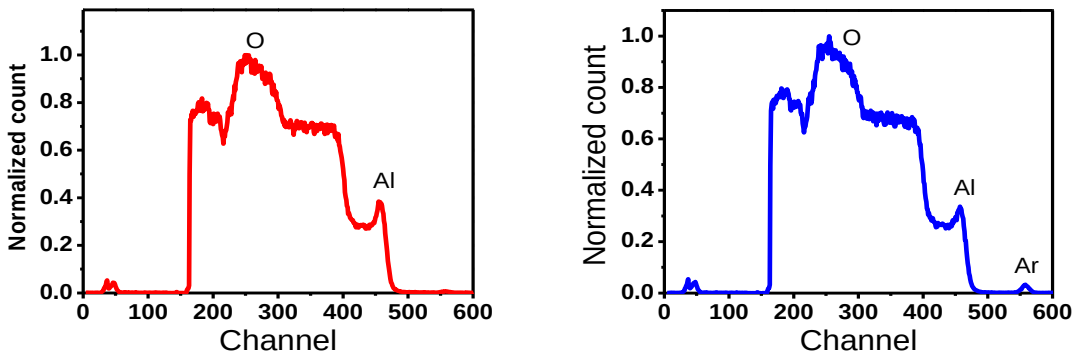

Figure 5.7 (a) RBS signal for AlO_x without substrate bias. (b) RBS signal for AlO_x with substrate bias. No difference except higher Ar concentration.

5.7 Conclusions and suggestions

The importance of process parameters on the physical structure of thin films and interfaces was demonstrated. Applying a substrate bias during the deposition of multilayers is a very effective way to get smooth layers and flat interfaces even without annealing. Post-deposition annealing may further improve the uniformity and crystallinity of the layers. But unwanted consequences when using substrate bias deposition such as changes in composition and deterioration of crystallinity need to be taken into consideration. A Ge buffer layer also provided a smooth surface for the layers to be grown on. In addition, studying the effect of substrate bias on the crystallinity and composition of layers other than IrMn and barrier in the MTJ structure is very important along with studying the effect on the transport properties. Such a study will help to develop a better understanding of MTJs. Furthermore, antiferromagnetic materials such as FeMn might be used with substrate bias without any significant changes in the composition as the Fe and Mn masses are similar, unlike Ir and Mn in IrMn.

The maximum TMR in Al_2O_3-based MTJs has been reported as 70%. In comparison, MgO (001) tunnel barriers provide a very high TMR (>600%). The study of alumina barriers provided understanding of the deposition of MTJ films as well as characterization. In the following chapters, we also explore MTJs based on MgO tunnel barriers. The next chapter will cover the details of the MTJ fabrication process that is carried out to achieve high TMR in MgO-based junctions.

Chapter 6 : Fabrication strategies for magnetic tunnel junctions

6.1 Basics of MTJ fabrication

In the previous chapter, the structural and magnetic properties of the entire MTJ stack were studied. However, the most relevant characterization for MTJs is the transport measurement. For experimental realization of high TMR values, it is important for the current to flow through the tunnel barrier and this requires a current perpendicular to plane (CPP) geometry. CPP geometry complicates the fabrication of the MTJs considerably because it is critical to ensure that the two FM layers in the MTJ structure are electrically insulated by the barrier layer and any other electrical conduction paths except quantum tunneling is prohibited. There are two basic approaches to fabricating MTJs in the CPP configuration. MTJs can be fabricated in a sputtering system with shadow masks to form cross-pattern junctions. The process includes three mask exchange steps for the bottom electrode, the tunnel barrier and finally the top electrode. In order to avoid edge effects, an additional intermediate step for thick insulation (SiO_2) becomes necessary before the top electrode deposition. The sample can be measured as soon as it is taken out of the chamber. This is the quickest way to fabricate a complete MTJ device without any break in vacuum or interaction with chemicals. Some limitations still exist, for example the smallest junctions one can make are around 80 μm,[118] and expensive and complicated mechanisms are required to ensure reliable pattern transfer.[119]

A lithography step needs to be included in the fabrication process to get smaller junction sizes- photolithography or electron beam lithography. The lithography method

is a very common and popular MTJ fabrication method as it is more easily accessible. Even while using lithography, different approaches can be adopted. The best way is to use an ion miller to etch off the layers in order to form a pattern. This is generally known as the subtractive method. Another approach is to simply use a four-step lithography process without using an ion miller. This is an additive approach and we will discuss it first.

6.2 Fabrication strategies

6.2.1 Additive approach

The following are the steps for the MTJ fabrication using the additive approach. Figure 6.1 provides the schematic of the additive process.

1. At first, patterned bottom electrodes were formed by the lift-off process. Different combinations were tried, for example: Cr/Au (thermally evaporated), Al_2O_3/Al/Cu (magnetron sputtered), and Ta/Cu and Ta/Ru multilayers.
2. The multilayer structure was then deposited and patterned using the lift-off process consisted of:

- AFM layer - IrMn. For exchange bias.
- FM layers - Co, NiFe, CoFe and CoFeB or bilayers.
- Tunnel barrier - Al_2O_3, MgO. Separates the two FM layers.
- Cap layer - Cu, Ta and Ru.

3. Insulation (encapsulation) layer - Al_2O_3 and SiO_2 openings were created using lift–off to contact the multilayer stack as well as the bottom electrode. This layer also prevents shorting between the top and bottom electrodes.
4. Finally, deposition of the top electrode provided four contacts for four-probe MR measurements.

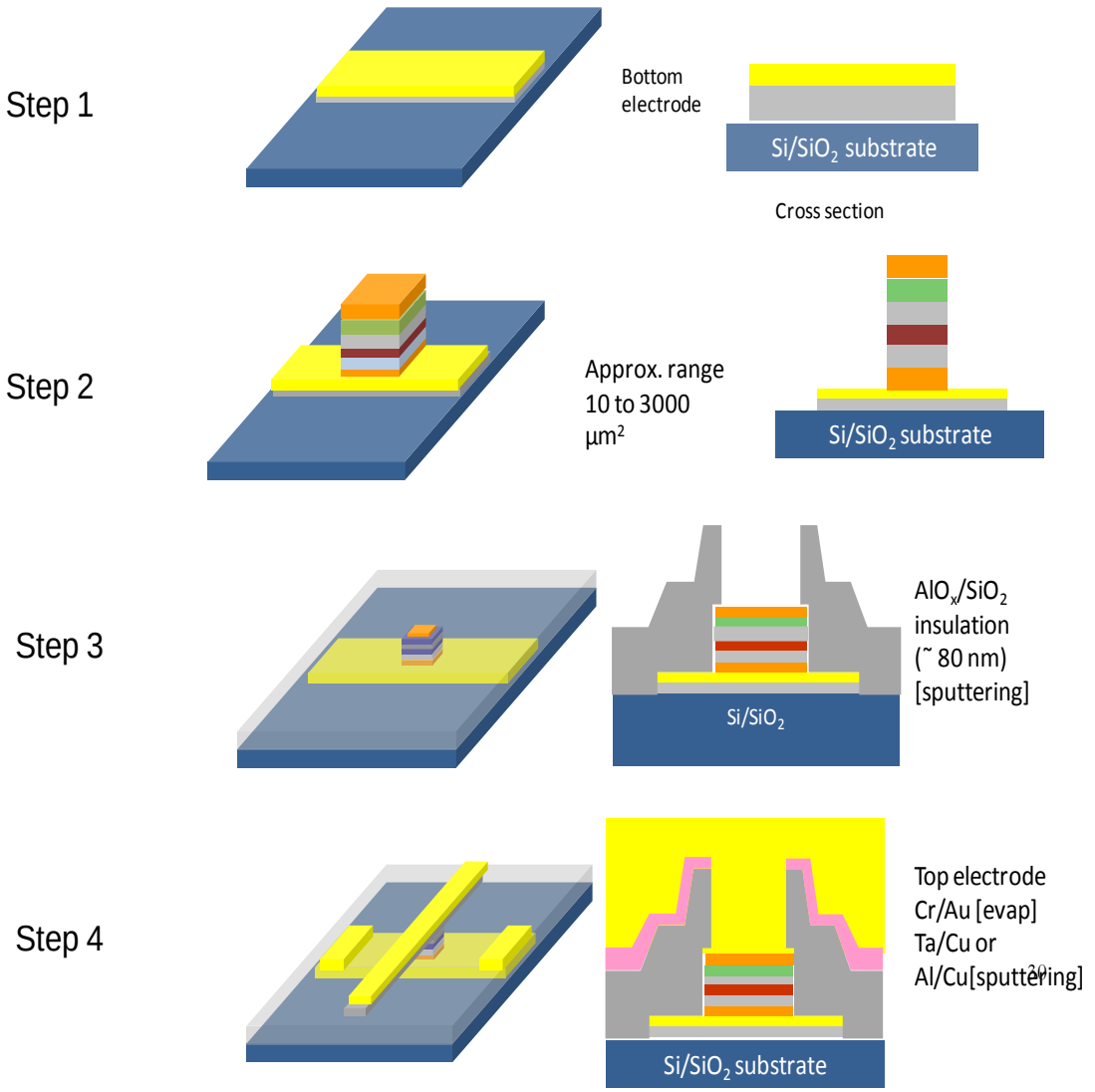

Figure 6.1 Schematic illustration of the steps involved in MTJ fabrication using additive approach (four-step lithography)

The problem with using the additive approach is that the quality of the device is compromised as sidewall shorting can occur as illustrated in Figure 6.2.

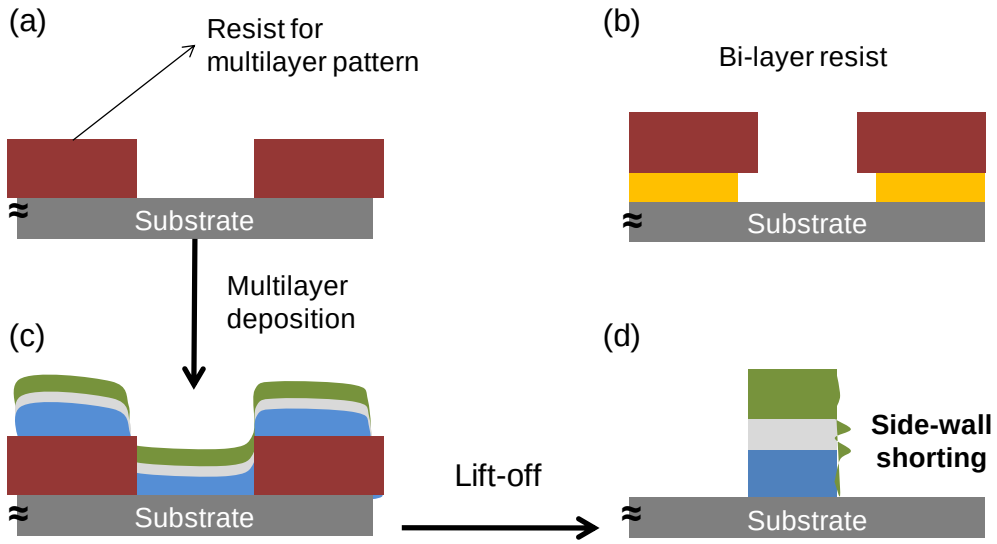

Figure 6.2 Schematic illustration of the additive steps (a, c) leading to sidewall shorting (d). Using a bi-layer resist (b) can be of some help though not the best choice.

6.2.2 Subtractive approach

1. Photo resist was patterned to define the junction region and the bottom contacts. The area of the bottom contacts should be more than 100 times that of the junction area for the latter to be dominant in MR measurements.
2. Ar ion-milling was used to etch the multilayer stack using an optimized recipe and SIMS detector to determine when to stop the milling process..
3. The etch step was followed by the deposition of SiO_2 dielectric to isolate the top and bottom electrodes, without breaking the vacuum.
4. Another lithography step was used to pattern the top electrode followed by top electrode deposition. The electrical contact area for the electrode was cleaned using Ar etching prior to the deposition of the electrode.
5. In the above two-step process, vias were opened using lift-off. Though the lift-off of oxides can be tricky, it saves time. On the other hand, another three-step process is possible whereby the opening is etched out. Here, there is a possibility of sidewall oxidation though it might be easier to etch the oxides off rather than lifting them off.[120]

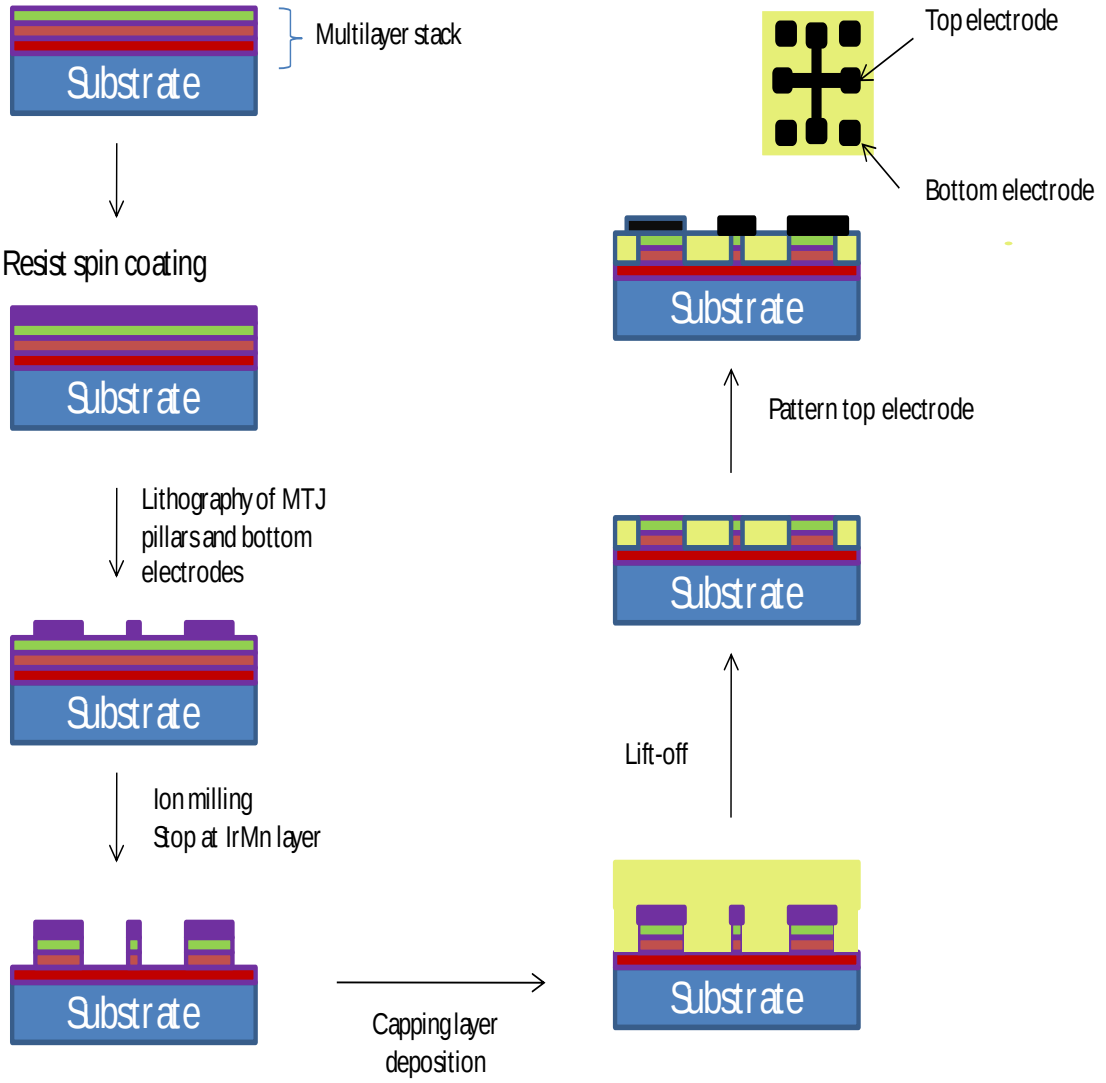

Figure 6.3 Schematic illustration of the different stages during the fabrication of MTJ device using the subtractive approach.

6.2.3 *GMR - experiments and results for spin valves*

A simple GMR structure shown below was deposited (with an in-situ-field). Current in-plane (CIP) measurement of GMR multilayers is an easy and quick way to check the quality of the films as well as the magnetic decoupling between the two FM layers and exchange bias. A high in-plane GMR signal (~10%) with a good exchange bias of 400 Oe was obtained. A schematic of the measurement configuration along with the GMR signal is shown in the Figure 6.4 below.

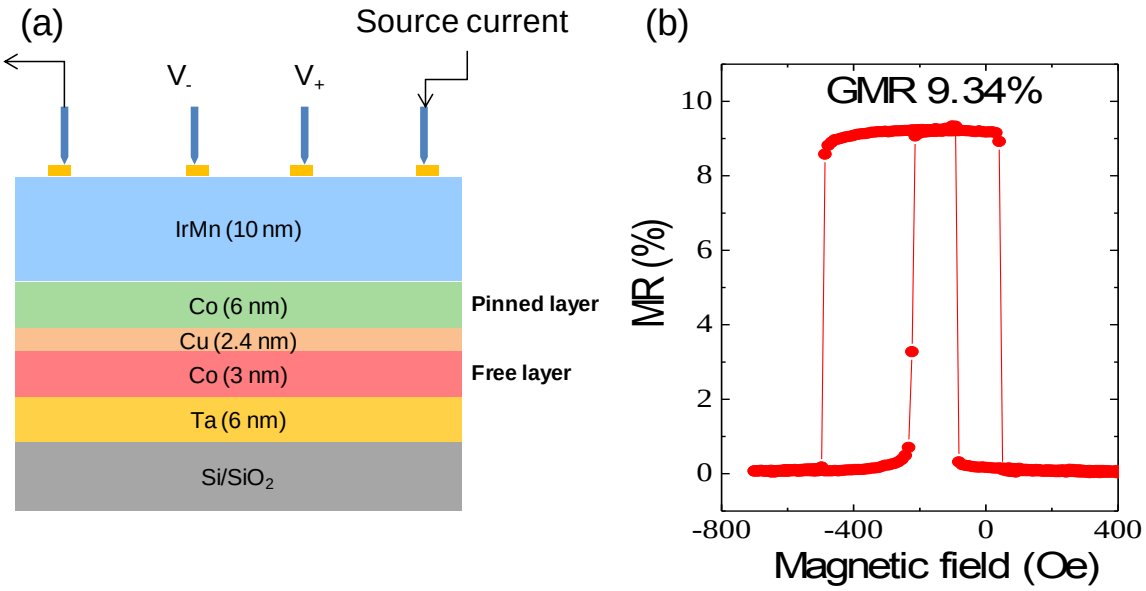

Figure 6.4 (a) GMR structure used for current in-plane (CIP) measurement (b) GMR signal from the device

6.3 MTJ - experiments and TMR result

The initial study was done using the additive approach and the barrier material used was Al_2O_3. All the films below were deposited in the dual chamber, 10-target AJA system. Though the MR obtained was not very large, with improvements in the fabrication process (subtractive method), better results were expected and attained. The main problem associated with the additive approach was probably the sidewall shorting, which reduced the overall junction resistance.

The substrates used were p-type Si (500 μm) with a thermally oxidized SiO_2 layer of about 300 nm. In order to measure the TMR, the MTJs were usually patterned into junction devices with two contact pads connecting to the bottom electrode and the other two contact pads to the top electrode so that a four-probe method could be used to measure the resistance of the junction and the contact resistance could be eliminated.

6.3.1 *RF sputtered Al_2O_3 barrier using additive approach*

An Al_2O_3 target was directly sputtered using an RF power supply to form the tunnel barrier (2 nm). The bottom electrode used was Ta/Cu/Ta, the thickness of each layer being 10 nm. The top electrode was formed by Ta (100 nm)/Cu (50 nm). The details of the MTJ stack and the TMR signals obtained are given below in Figure 6.5.

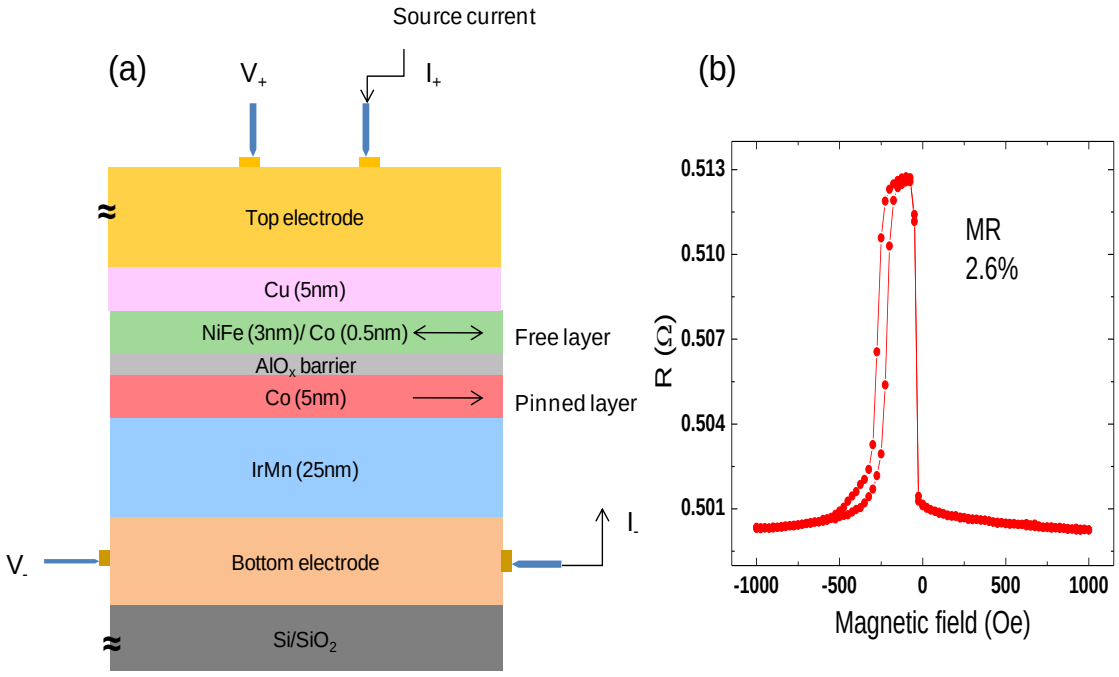

Figure 6.5 (a) MTJ structure used in CPP configuration (b) maximum MR of 2.6% obtained using Al_2O_3 tunnel barrier

The maximum MR obtained was around 2.6%. The measurement was done after annealing at 230 ˚C for 2 hours with a field of 2 Tesla. The signal was clear with a good exchange bias but the resistance was extremely small. The main reason for this was side-wall shorting. MTJs were also fabricated with reactive sputtered and naturally oxidized alumina barriers using the additive strategy but the TMR signal was extremely small (<<1%).

6.3.2 Subtractive approach with MgO tunnel barrier in a new system

1. The additive approach helped in getting adept with the basic fabrication process for MTJs and CPP measurements though the quality of devices was limited.
2. MgO was to be used as the barrier for future experiments in another AJA magnetron sputter system with 11 targets (single chamber) and a base pressure of 2×10^{-9} Torr.
3. Subtractive approach using ion-milling would be the key for the fabrication of high quality MTJs.

6.3.3 Underlayer roughness

Ta underlayers were deposited under different conditions and optimized for minimum RMS roughness. An optimized condition for MgO layer deposition was also achieved as it is the most critical layer in the MTJ stack. Although it is essential to optimize the deposition conditions of different layers for low roughness to ensure flat interfaces as well as to prevent shorting of the two FM layers, it is important to note that the roughness of the MgO layer is not as critical as the crystalline texture for giant tunneling magnetoresistance.

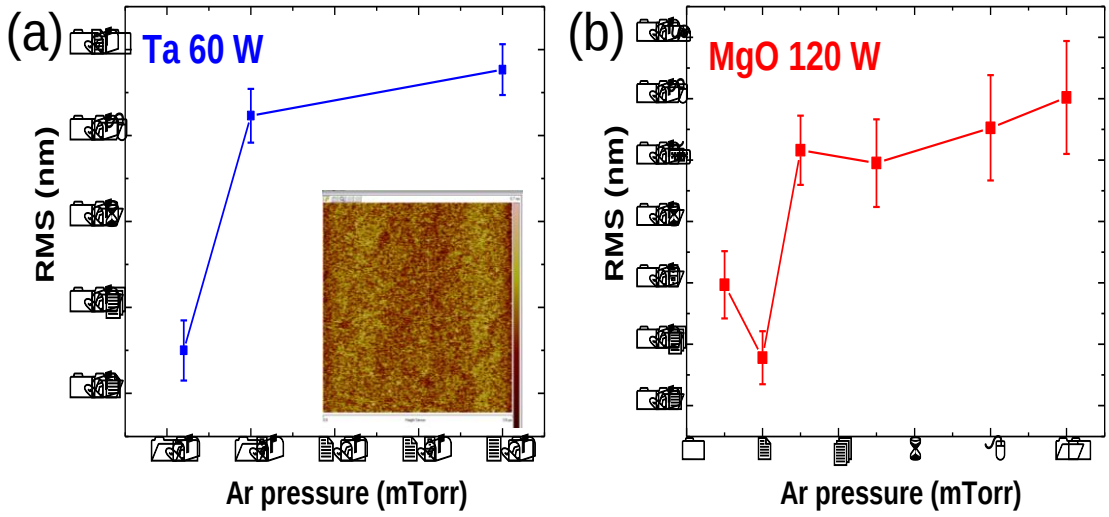

Figure 6.6 (a) RMS roughness of Ta layer deposited at 60 W dc power, inset shows the AFM image. (b) Optimization of MgO deposition pressure for minimum roughness.

CoFe composition was 70/30 throughout while for CoFeB, it was 40/40/20.[121] Ru is an ideal material to be used as a cap layer as RuO_2 is a good conductor, unlike TaO_2.[122] High quality MgO targets from Ube materials and Kojundo were used.[123]

6.4 TEM of MgO-based MTJs

The AFM and profilometer are generally used for the thickness calibration of different thin films to be used in the MTJ stack. However, for the MgO layer, calibration of a very high reliability is important as the tunnel current has an exponential dependence on the tunnel barrier thickness. Although sample preparation is tedious, cross-sectional TEM provides precise thickness values and critically important information on the crystalline quality of the MTJ stack. This is especially valuable in MgO-based MTJ structures..[39, 124, 125]

TEM analysis has been done for several MTJ configurations. The effects of different IrMn configurations i.e., top and bottom of the MTJ structure and its

roughness are shown in Figure 6.7. Even with IrMn on top, the structure was not very uniform, due to rough underlayers.

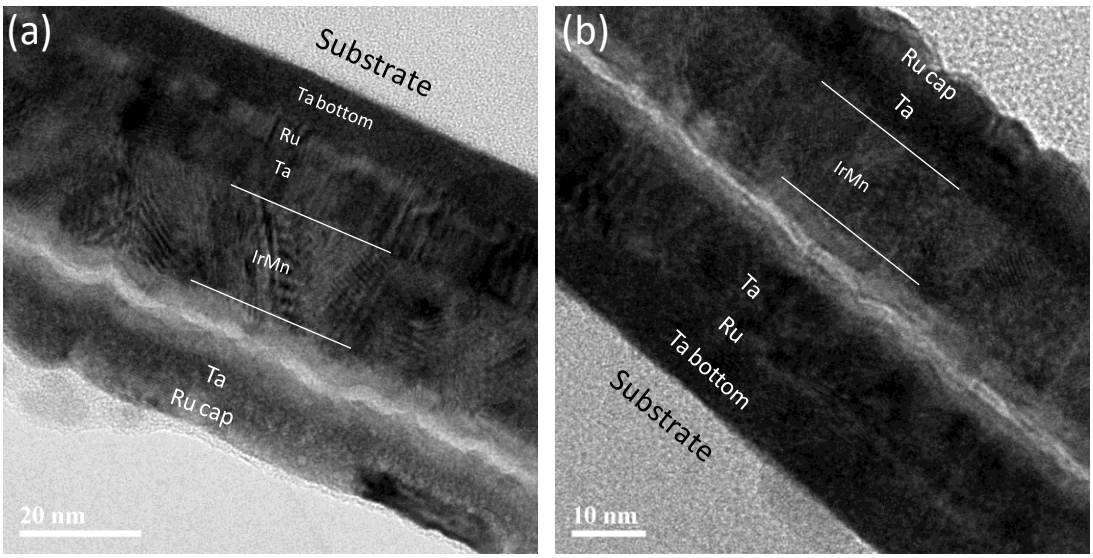

IrMn bottom
Ta (10nm)|Ru (5nm)|Ta (10nm)|IrMn (20nm)|
CoFe (4nm)|MgO (3nm Kojundo)|CoFe (1nm)|CoFeB (4nm)|
Ta (5nm)|Ru (10nm)

IrMn top
Ta (10nm)|Ru (5nm)|Ta (10nm)
CoFeB (4nm)| CoFe (1nm)| MgO (3nm Kojundo)|CoFe (4nm)|
|IrMn (20nm)|Ta (5nm)|Ru (10nm)

Figure 6.7 Cross-sectional TEM micrographs of MTJ structures with different IrMn configurations (a) bottom and (b) top

A thin layer of Ru was sandwiched between the Ta underlayers to improve the conductivity of the bottom electrode. Using an underlayer without Ru was observed to improve the surface roughness slightly. Figure 6.8 compares the same film structure with Ta and Ta/Ru/Ta underlayers. Nevertheless, we observed that IrMn deposited over a Ta underlayer has a good crystalline texture, which helps the CoFe – and hence the MgO – to have a good (001) texture [Figure 6.9].[35]

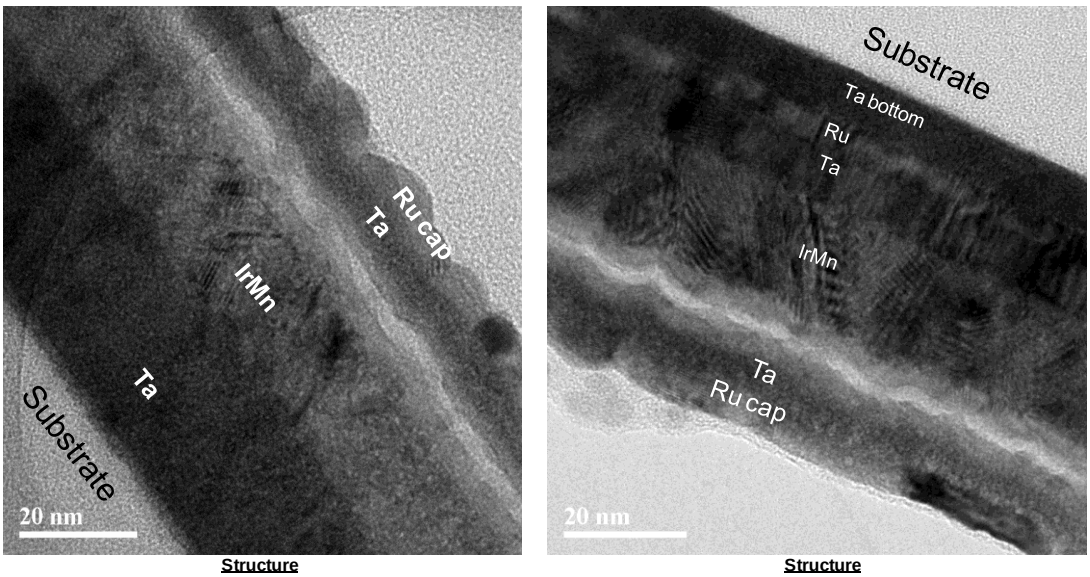

Structure
Ta (20nm)|IrMn (20nm)|
CoFe (4nm)|MgO (3nm)|CoFe (1nm)|CoFeB (4nm)|
Ta (5nm)|Ru (10nm)

Structure
Ta (10nm)|Ru (5nm)|Ta (10nm)|IrMn (20nm)|
CoFe (4nm)|MgO (3nm)|CoFe (1nm)|CoFeB (4nm)|
Ta (5nm)|Ru (10nm)

Figure 6.8 TEM images illustrating MTJ structures deposited with different underlayers (a) Ta and (b) Ta/Ru/Ta

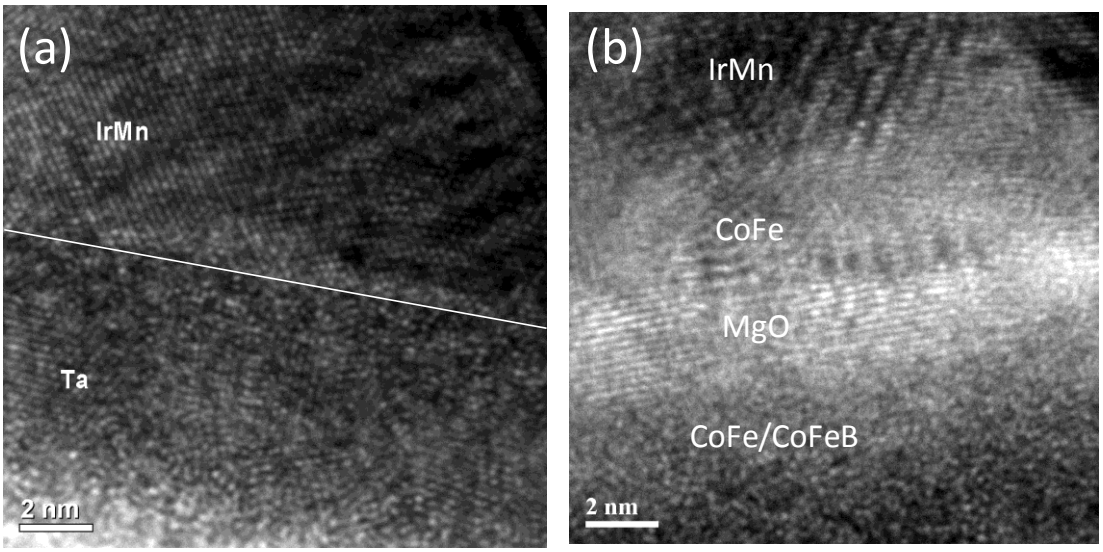

Figure 6.9 TEM images showing (a) Ta/IrMn interface with Ta providing a template for good IrMn texture (b) a good IrMn surface texture ensures the growth of CoFe and MgO with (001) orientation.

Over a period of time, the conditions for different layers especially the IrMn layer and the Ta underlayer were optimized. Different deposition rates (target power)

and working pressures were tested. Slow deposition rates at a lower working pressure (2 mT) gave the best results [Figure 6.10].

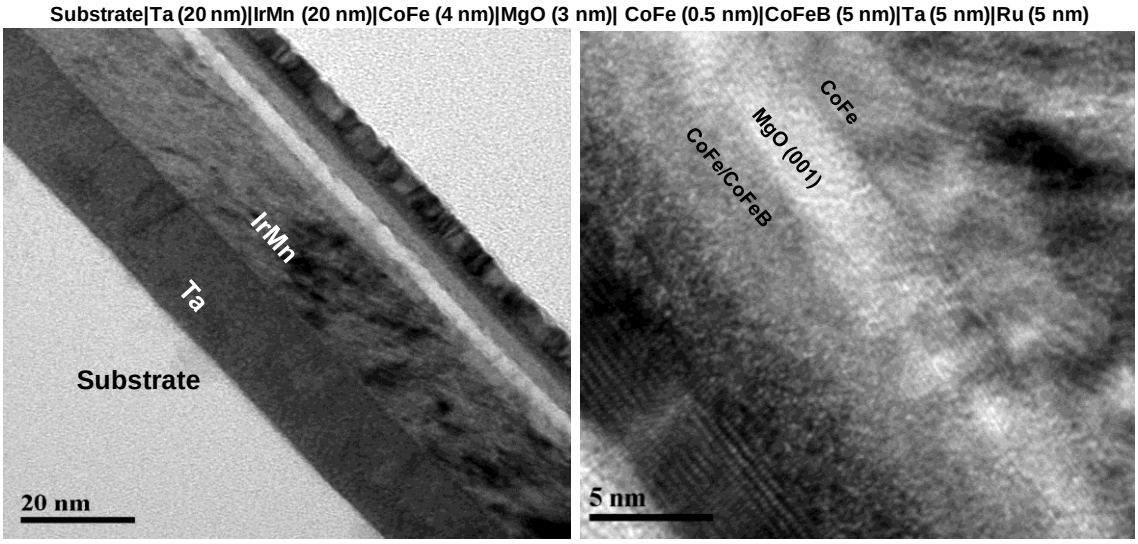

Figure 6.10 TEM images for the MTJ structures with (a) optimized IrMn conditions providing flatter interfaces and (b) good MgO (001) texture.

IrMn, an antiferromagnet (used for exchange bias), forms the thickest layer in the stack and induces roughness if the deposition conditions are not optimized.[126] It becomes important for the IrMn surface to have a favorable crystalline orientation in order to act as a flat template for the CoFe layer to be deposited. The roughness of the Ta underlayer, which forms the base of the structure, is equally critical.

6.5 Ion-milling process optimization for fabrication of MTJs

In order to fabricate the MTJ devices, the ion milling conditions had to be optimized with parameters, including the etching angle, rotation speed, beam current (Ar^+ ion beam) and etching time. The base pressure of the system used in this work was 9×10^{-8} Torr with a working pressure of 10^{-4} Torr.

6.5.1 SIMS profile for MTJs

The ion-milling system was equipped with SIMS with automatic end-point detection features. Using this feature, the etching could be stopped at any layer in the MTJ stack with nanometer accuracy. For our MTJ structures with MgO tunnel barrier, the Mg peak was very strong along with the Ru cap peak as shown in Figure 6.11.[122, 127] The vertical etching was stopped at the bottom IrMn layer in the beginning of the Ir peak, as shown in the SIMS profile of an etch process below [Figure 6.11]. After the vertical etch, it became important to remove any debris (from the etch process) attached to the sidewalls of the MTJ pillar which might act as a shorting path for the current during the device measurement. Hence, another etch step was carried out with the rotating substrate holder at an angle so as to clean the sidewall of the MTJ pillars. Different angles (between 45˚ to 70˚), etching times and etching rates were tried until a reasonably high TMR signal was obtained from the MTJ pillars.[128] An etching angle of around 45˚ and etching time of around one-third of the vertical etch time gave the best results. A beam current of 110 mA was selected for all the fabrications after optimization. A lower current of 45 mA took a long time and resulted in a lower MR while a higher current was more damaging to the device as well as the resist.

The ion miller had four magnetron sputter guns, allowing the in-situ deposition of the SiO_2 dielectric onto the etched MTJ pillars without breaking the vacuum. Deposition of SiO_2 is an important step as it ensures isolation between the top and bottom contacts. Hence, the insulation properties of the deposited SiO_2 should be good and the thickness should be optimum. An insulator layer of insufficient thickness will not cover the pillar completely whereas a very thick SiO_2 is hard to lift off. For our processes, we always ensured that there was an excess of 10 nm of SiO_2 surrounding the etched MTJ pillar. This combination of ion-milling and sputter deposition also

provided an additional option of cleaning the interfaces before the deposition of the electrical contact pads. A few seconds of etching prior to the electrode deposition ensured a cleaner surface with good adhesion as well as the removal of any native oxide of the topmost layer.[119]

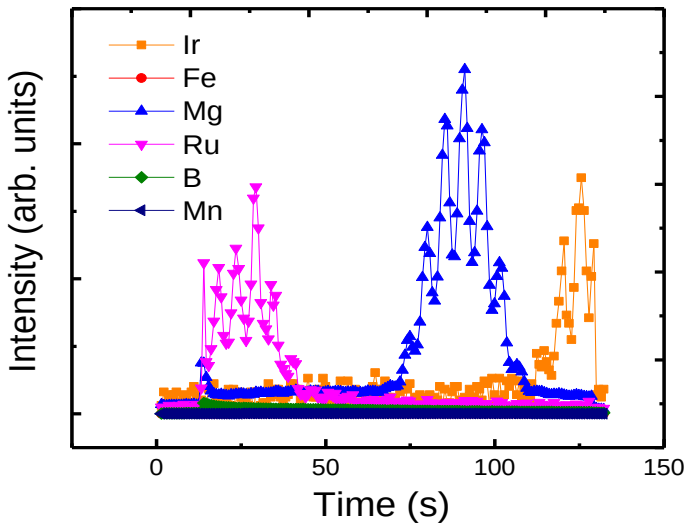

Figure 6.11 SIMS signal for an MTJ stack – Ru/Ta/CoFe/MgO/CoFe/IrMn/Ta/Sub – showing strong peaks of the Ru cap layer, the MgO tunnel barrier and the IrMn antiferromagnet layer used for etch stop.

With optimized conditions of the etching angle, etching time, beam current and rotation speed, high values of TMR were achieved successfully. The structure and the corresponding TMR values are discussed below.

6.5.2 TMR in pseudo-spin valve (PSV) and spin valve (SV) based MTJs

We fabricated a pseudo spin valve MTJ with the structure as used by Ikeda et al., renowned for the maximum value of TMR at room temperature-604%.[37] Although the junction damaged when annealed at temperatures >350˚C, for relatively milder conditions – 300˚C for 30 minutes – the TMR we obtained was much higher (262%) than that reported for the same temperature by Ikeda et al., [Figure 6.12(a)].

For as-deposited SV based MTJs, we obtained TMR in the range of 11-16% for junction areas lower than 100 μm^2. After magnetic field annealing at 350˚C, for around 30 minutes, the TMR increased to ~80%. Even with large bottom pads with junction area of 10^4 μm^2 gave a TMR of 42%, indicating a very uniform MgO tunnel barrier layer over a large area. For a tunnel barrier of 2 nm, the maximum TMR we achieved was 71% [Figure 6.12(b)].

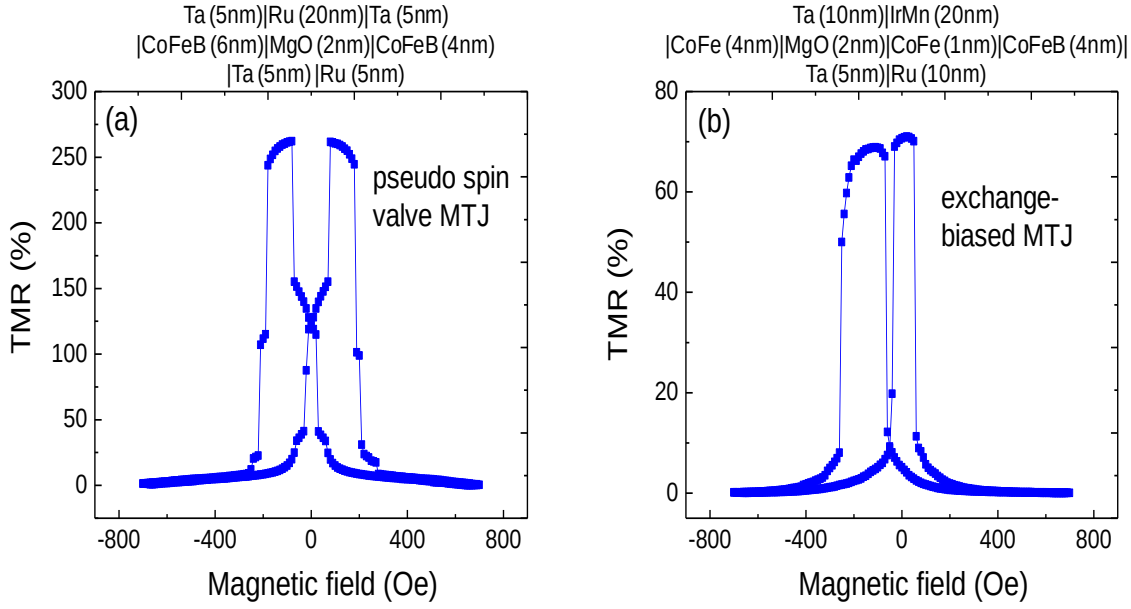

Figure 6.12 TMR loop data for (a) pseudo-spin valve MTJ with 262% TMR (b) exchange biased MTJ with 71% TMR– each with a 2 nm MgO tunnel barrier.

6.5.3 TMR in synthetic antiferromagnet (SAF)-based MTJs

We carried out a similar fabrication process for SAF based MTJ samples. Consistently high TMR was achieved on the devices fabricated. The maximum TMR at room temperature was around 115%, which rose to 146% at a lower temperature as shown in Figure 6.13(a). Furthermore, the temperature-dependent characteristics were typical of MTJs, TMR and R_{AP} increasing and R_P remaining almost constant with decreasing temperature [Figure 6.13(b)]. At the same time, the yield was very high with around 75% working devices [Figure 6.13(c)]. One difference here is that MgO

was deposited by reactive sputtering of Mg in an Ar-O_2 gas environment. These samples were annealed at 300˚C for 30 minutes under a 1 T field.[30] Even for a device with a 1 nm thick MgO barrier, a maximum TMR of 20% was achieved.

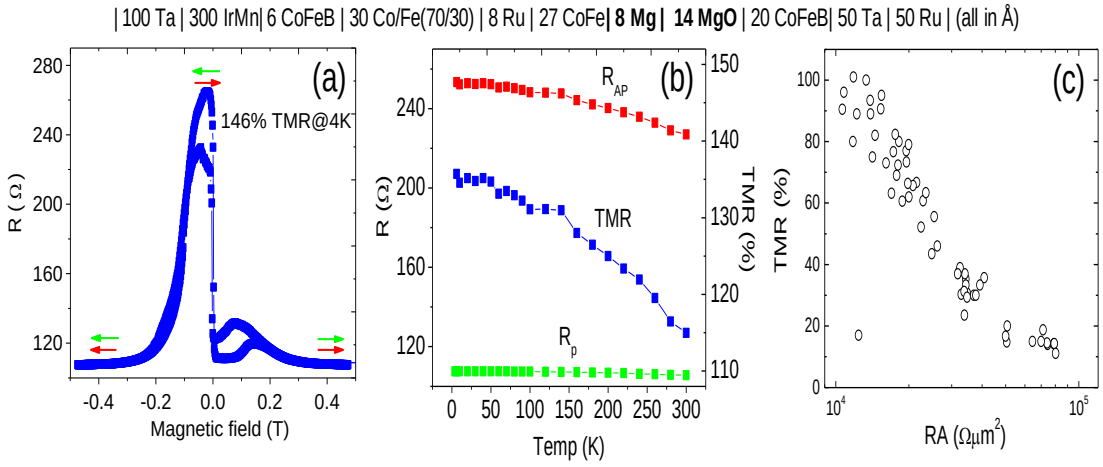

Figure 6.13 (a) MR curve for one of the MTJs (73 μm^2) at 4 K (b) temperature dependence (c) Plot of TMR versus RA product where each point corresponds to one device.

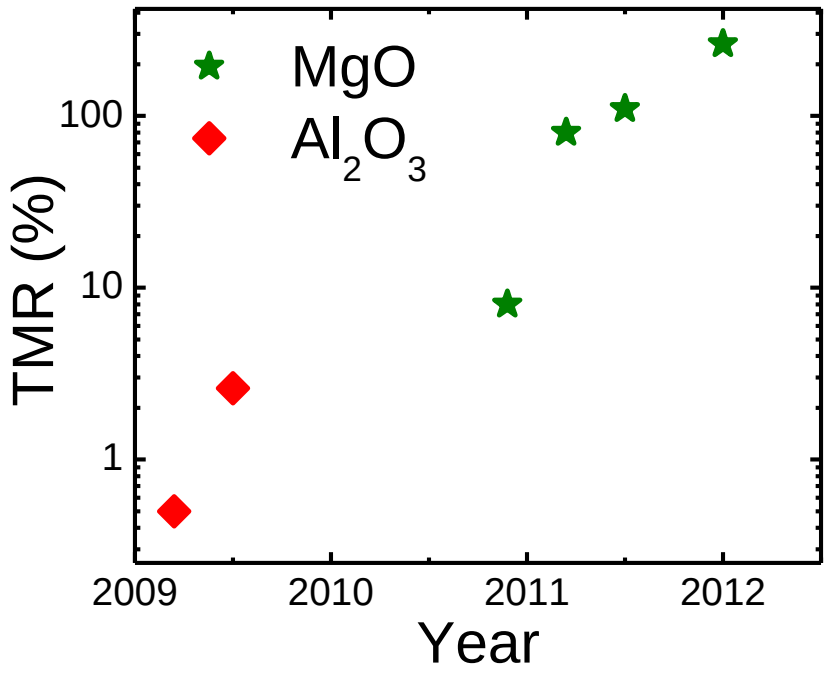

Figure 6.14 TMR ratio achieved over the past three years (during the PhD.).

The next chapters will study the different effects in MTJs such as strain and capacitance.

Chapter 7 : Biaxial strain effect of spin-dependent tunneling in MgO magnetic tunnel junctions

7.1 Motivation

With an optimized fabrication process for MTJs, it becomes possible to study the effects of different parameters on the performance of these devices. One of the main concerns in MTJs as read sensors in HDDs is their high resistance and the resulting compromise on the SNR. The industry is on an incessant pursuit of strategies to resolve this problem while still keeping the advantages, i.e. a high MR.

In this chapter, we have studied the effect of strain on magnetic tunnel junctions (MTJ) induced by a capping layer based on diamond-like carbon (DLC) film. The junction resistance as well as the tunnel magnetoresistance (TMR) was reduced with the DLC film. Non-equilibrium Green's function quantum transport calculations showed that the application of biaxial strain increased the conductance for both the parallel and anti-parallel configurations. However, the conductance for the minority channel and for the anti-parallel configuration was significantly more sensitive to strain, which drastically increased the transmission through an MgO tunnel barrier, thereby reducing the TMR ratio.

7.2 Introduction

The material and interface engineering of magnetic tunnel junctions (MTJ) is the key for the future of spin transfer torque-based random access memory (STT-RAM), one of the promising candidates for the next generation of storage technology.

A value of tunneling magnetoresistance (TMR), one of the most important attributes in MTJs, exceeding 1000% has been predicted[33, 34] and recently achieved in MTJs with single crystalline or textured MgO(001) tunnel barriers[35-37] through which the Δ_1 Bloch states (in Fe- and CoFe-based alloys) tunnel coherently. In this case, the crystalline property of the structure, especially that of the ferromagnet/MgO interface, plays a very critical role in the device performance[112, 129] and the presence of strain in the structure can change the properties of the device significantly.

Over the last decade, controlled strain has been used to improve performance and lifetime of semiconductor devices such as the low cost metal oxide semiconductor field effect transistors (MOSFETs).[130] For example, one of the approaches is to induce strain during growth in the SiGe layer on Si[131] and another approach is the use of external mechanical stress.[132] High-stress capping layers deposited on MOSFETs have been investigated as a technique to introduce stress into the channel and this approach is referred to as local mechanical stress control (LMC), first demonstrated using a SiN layer.[132] Recently a new line stressor based on diamond-like carbon (DLC) films has been proposed with very high intrinsic stress (few GPa) and high sp^3 content [Figure 7.1].[133, 134]

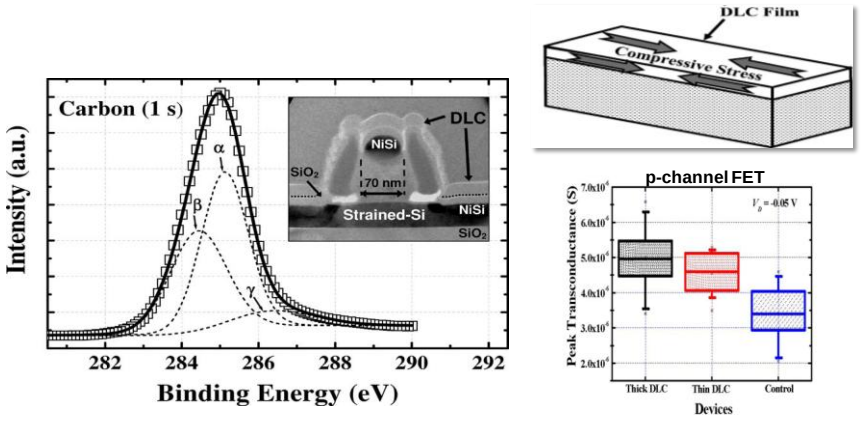

Figure 7.1 DLC films used in the CMOS research. Using DLC film there is enhancement in the transconductance of the p-channel FET.[133, 135]

For the case of MgO-based MTJs, the role of epitaxial strain has been discussed in several reports. Using *ab initio* electronic structure calculations, Park *et al*. showed the narrowing and broadening of the interfacial spin-majority bands (MJ) of an MgO/FeO/Fe(001) structure under the effects of tensile and compressive epitaxial strain respectively.[136] In contrast, Yeo *et al.* studied the interface states of a strained MgO/Fe(001) system and showed the position of the minority spin (MN) peak state near the Fermi energy shifts upwards in energy with respect to the Fermi energy for tensile strain, while it moves downwards for compressive strain.[137] A few experimental reports have also studied the effect of lattice mismatch on the transport properties in Fe/MgO/Fe(001) and related systems.[138-140] Miao *et al*. studied the strain relaxation at the top Fe/MgO interface with different MgO buffer thicknesses on a Si substrate and its effect on the TMR, which is reduced for a thicker MgO buffer (> 5 nm) as a result of increasing roughness,[138] while Herranz *et al*. observed a reduction in 1/f noise and enhancement in TMR as a result of alloying Fe electrodes with an optimized amount of V, reducing the MgO/Fe interface lattice mismatch.[140]

In this chapter, we have studied the effect of a high stressing DLC film on the tunneling behavior of MgO-based MTJs. With the deposition of DLC film over tunnel junctions, the TMR as well as the junction resistance were suppressed, demonstrating the effects of external mechanical strain on the transport properties of MTJs. Though the TMR was reduced with the application of strain, it was interesting to understand the physics behind it and, at the same time, strain-induced reduction in the junction resistance is encouraging for industries utilizing MTJs as read sensors in hard disk drives. To corroborate the experimental results, the effect of biaxial strain was evaluated using Non-equilibrium Green's function (NEGF) quantum transport calculations for a Fe(100)/MgO/Fe(100) tunneling junction. The calculations showed

that biaxial strain increases the conductance for both the parallel and anti-parallel configurations. However, a $k_{//}$-resolved transmission analysis demonstrated that the minority channels were more sensitive to strain. The minority and anti-parallel transmissions both increased more than the majority transmission, and biaxial compressive strain was calculated to decrease the TMR ratio, in agreement with the experiments.

7.3 Experimental methods

MTJs were grown using magnetron sputtering in an ultra-high vacuum chamber with the structure of 100 Ta/300 $Ir_{22}Mn_{78}$/6 $Co_{40}Fe_{40}B_{20}$/30 $Co_{70}Fe_{30}$/8 Ru/27 $Co_{70}Fe_{30}$/8 Mg/14 MgO/20 $Co_{40}Fe_{40}B_{20}$/50 Ta/50 Ru (all thickness in Å). The MgO barrier was formed by the reactive sputter deposition of Mg in Ar-O_2 plasma (~2% oxygen). The Mg layer prevented the oxidation of the underlying ferromagnetic electrode and became converted to MgO by reactive oxygen introduced into the sputter chamber during the deposition of the MgO layer. Samples were annealed at 300 ˚C for 30 minutes under a 1 T magnetic field and then the MTJs were fabricated in a current perpendicular-to-plane (CPP) configuration using a combination of Ar ion-milling and photolithography processes. A number of devices of different junction areas were measured after fabrication and a 40 nm DLC film was then deposited over the junction, exerting a compressive biaxial strain on the tunnel junction along the *x* and *z* axes.[133] Figure 7.2(a) shows a schematic diagram of the device configuration with the DLC layer on top, while Figure 7.2(b) shows a scanning electron microscope (SEM) image with a DLC film over one of the tunnel junctions.

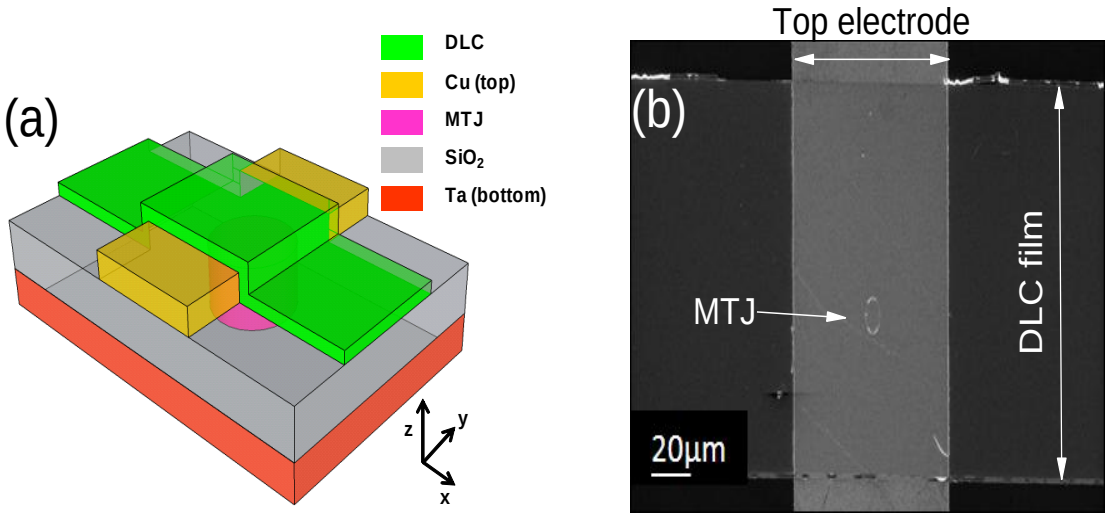

Figure 7.2 (a) Schematic of the device configuration with a DLC layer over the junction area. (b) A scanning electron microscope (SEM) image with a DLC film over the tunnel junction. The top electrode width was 80 μm while the DLC strip had a width of 150 μm.

DLC films were grown by filtered cathodic vacuum arc (FCVA) and a method used by Ehsan *et al.* was adopted that provides good adhesion along with high sp^3 content for enough strain.[141] Ion energy of about 100 eV was selected as it provides the highest fraction of sp^3 bonds with the maximum density and hardness.[142, 143]

7.4 DLC film properties

Figure 7.3 shows the X-ray photoelectron spectroscopy (XPS) spectra of the C_{1s} core level for the DLC film used in this work, which indicated a very high sp^3 proportion (65%) of the film as has been used for MOSFETs with compressive stress as high as 7.5 GPa.[133] A higher sp^3 fraction in the DLC film was important to induce sufficient strain. The C_{1s} spectra of the samples were adjusted by subtracting the Shirley Background,[144] and the adjusted spectra were subsequently deconvoluted with a set of Gaussian curves located at certain binding energies corresponding to one of the chemical states (C-C sp^1, C-C sp^2, C-C sp^3, C=O, and C-O) existing in the structure of

the film.[145] The atomic fraction of each component was obtained by integrating each of the associated Gaussian curves.

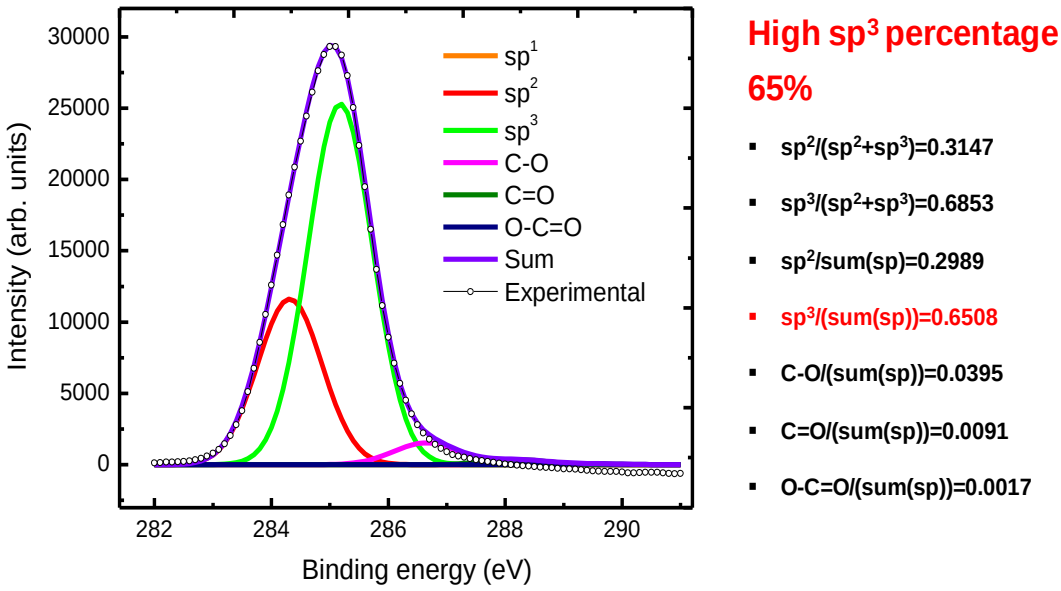

Figure 7.3 XPS spectra of the C_{1s} core level for the DLC film indicating a very high relative sp^3 proportion (65%) of the film.

7.5 Effect of DLC film on measured TMR and its voltage and temperature dependence

Figure 7.4 shows a plot of the TMR versus junction area for the MTJs before and after the deposition of DLC film at room temperature. The TMR ratio is defined by $(R_{AP}-R_P)/R_P$, where R_P and R_{AP} are the junction resistance in the parallel and anti-parallel alignment of the ferromagnetic electrodes, respectively. Before the deposition of the DLC film over the MTJs, it was observed that the TMR was gradually reduced as the junction area increased. The DLC film was then deposited over tunnel junctions of areas ranging from 50 to 10^4 μm^2. It was clearly observed that there was a suppression of TMR for junction areas below 500 μm^2, and that the TMR after the DLC deposition gradually reduced as the junction area decreased. The change due to

the DLC layer was bigger in the devices with smaller junction areas due to higher effective strain in a smaller junction.

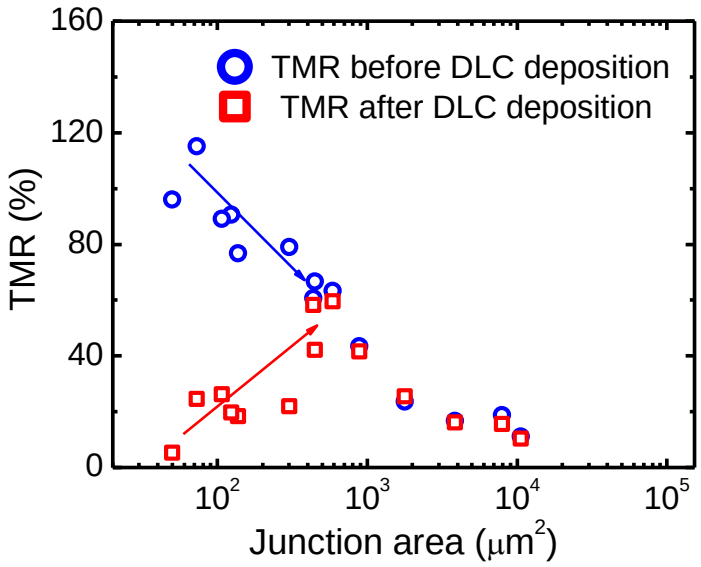

Figure 7.4 A plot of TMR versus junction area for the MTJs showing a reduction in the TMR of devices after the deposition of the DLC film below the junction area of 500 μm^2.

The loop data, before and after the DLC deposition, for a device with a junction area of 73 μm^2 at 300 K and 6 K are shown in Figure 7.5. Both the TMR as well as the junction resistance were reduced after the deposition of a highly stressed DLC layer. Coupling between the fixed and the free layer as a function of temperature can be used to understand the tunnel barrier properties.[146] For example, in the presence of pinholes in the tunnel barrier, Pong *et al*. observed an increase in the coupling of the free layer and the reference layer from the shift in the free layer loop. As shown in Figure 7.5, the free layer loop of the device before and after DLC deposition had no difference, therefore we ruled out any possibility of pinholes in our samples due to strain.

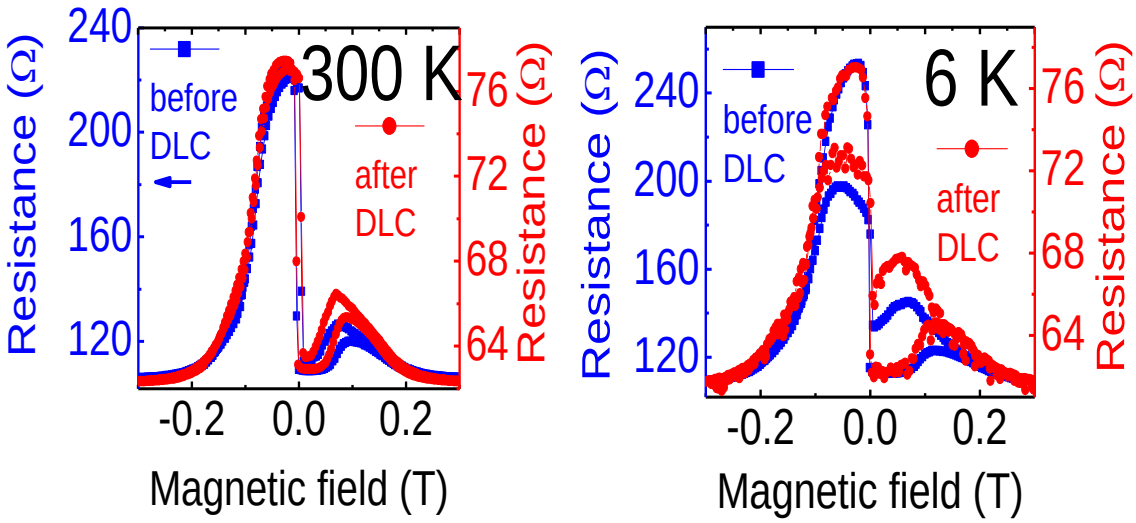

Figure 7.5 The loop curve for a device with the junction area of 73 μm^2 before and after DLC deposition at 300 K and 6 K.

We also did transport of ions in matter (TRIM) calculations for the energy of C ions used in this study. The maximum penetration depth of C in the Cu top electrode (100 nm thick) was only 5 nm with a peak at ~ 1 nm, which also supported the notion that the junction damage due to DLC deposition was negligible [Figure 7.6].

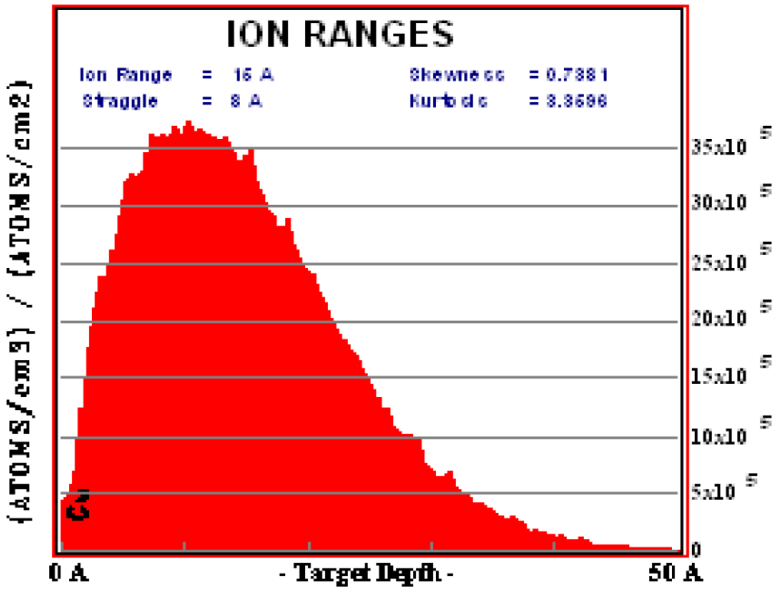

Figure 7.6 TRIM data for carbon penetration in Cu electrodes – maximum penetration depth 5 nm with a peak at 1 nm.

The voltage dependence of the TMR and junction resistance of the device showed a tunneling feature before DLC deposition as shown in Figure 7.7(a), such that the TMR decreased with increasing bias voltage and the parallel state resistance (R_p) was independent of bias voltage, as typically observed in MgO-based MTJs.[147] Figure 7.7(b) shows suppression in the voltage dependence of TMR after the deposition of the DLC film over the device. For the unstrained device, the relative reduction in TMR at 0.4 V was 43% with respect to the value at zero bias, while for the strained device the relative reduction was only 14%. We also carried out temperature-dependent studies.

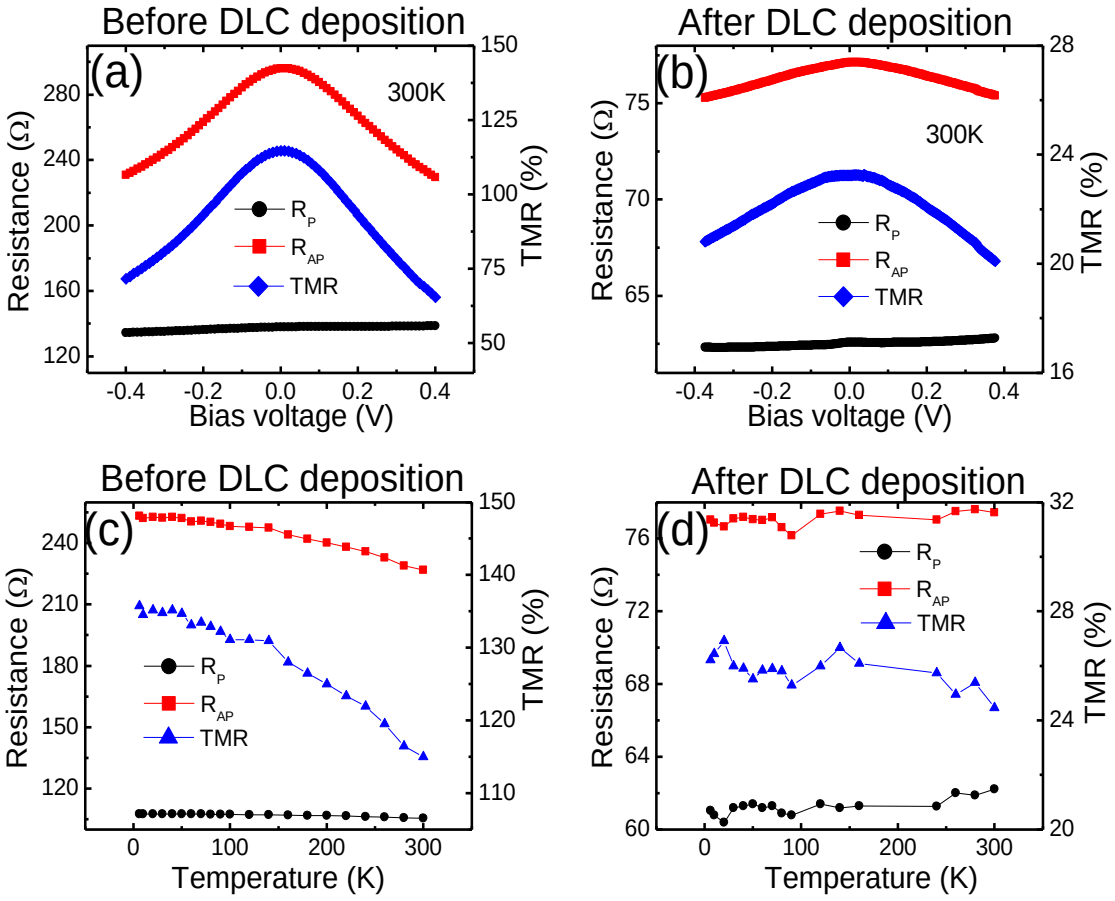

Figure 7.7 Bias voltage dependence of resistance in the parallel and anti-parallel states with TMR, for an MTJ before (a) and after (b) DLC deposition at 300 K. Temperature dependence of resistance in the parallel and anti-parallel states as well as TMR before (c) and after (d) DLC deposition for a device with the junction area of 73 μm^2.

For the unstrained device, R_p had little temperature dependence, while the anti-parallel state resistance (R_{ap}) increased as the temperature was reduced, as shown in Figure 7.7(c). On the other hand, when the same device was strained using the DLC film, in addition to reduction in the magnitudes of TMR and R_{ap}, their temperature dependence was also suppressed, as shown in Figure 7.7(d). This clearly indicates the effect of strain on the bias voltage and temperature dependence of an MTJ, which could be related to the changes in the tunneling probabilities as shown by our calculations.

7.6 Theoretical methods

Coherent tunneling transport in a Fe/MgO/Fe tunneling junction [Figure 7.8] was described by the NEGF formalism[148] as implemented in the Green program.[149, 150] The electronic structure of the tunneling junction was described by the Extended Hückel Molecular Orbital (EHMO) Hamiltonian,[151] using literature values for the Fe *spd*, Mg *spd*, and O *sp* parameters.[152] With these parameters, a bulk MgO band gap of 7.8 eV and a bulk Fe magnetic moment of 2.0 μ_B were calculated, in good agreement with the experimental data of 7.77 eV and 2.2 μ_B, respectively,[153, 154] and with the hybrid Density Functional Theory calculations using the HSE03 functional (DFT-HSE03).[155-157] Detailed DFT-HSE03 calculations for a four-layer MgO slab on a six-layer Fe(100) slab showed that the top of the MgO valence band edge was located about 4.0 eV below the Fermi level of the system. Therefore, a similar offset was used in our EHMO-based transport calculations. Note that the EHMO band gap for a six-layer MgO slab, 7.2 eV, was significantly larger than the DFT-HSE03 value of 3.7 eV. The effect of biaxial strain on the MgO band gap was, however, accurately described by EHMO, as discussed below.

Transport calculations were performed for MgO barriers of 4, 6, 8, 10, and 12 layers. For the unstrained transport calculations, the experimental Fe lattice constant of 2.87 Å was used for the Fe(100) contacts. The MgO(001) slab, rotated 45 degrees with respect to the Fe lattice, was then placed 2.16 Å over Fe (100) contacts so that the O atoms sit directly above the Fe atoms. In the experiments, strain was applied to the whole multilayer structure by a DLC film. It was assumed that biaxial stress in the range of 5 to 10 GPa leads to a compression of about 2.5 to 5%. Therefore, the effects of compression on the conductance and TMR ratio of the junction were evaluated for a compression of 5% along the *x* and *z* directions [as defined in Figure 7.8], and an

expansion of 2.3% in the *y* direction using the MgO Poisson ratio of 0.187.[158, 159] In reality, the compression was likely to be somewhat smaller than 5% due to the thick top electrode. To confirm that our results remain valid for different values of strain, transport calculations were also performed for a six-layer MgO junction and for compressive strains of 2.5%, 3.5% and 10%.

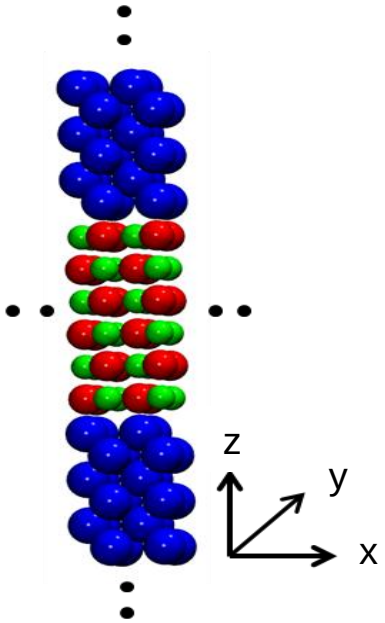

Figure 7.8 Central structure used to model the junction for six layers of MgO. The blue, green, and red circles correspond to Fe, Mg, and O atoms, respectively. In the calculations, both Fe(100) contacts extend to infinity. The x, y, and z directions are indicated.

We benchmarked our calculation for the unstrained MTJ with the results available in the literature. It is important to note that the exact TMR ratio and the current values are very sensitive to the details used in the calculation.[152] As a result it is difficult to match exactly the earlier reported values. However, our calculations show similar trend and the values are within the acceptable limit. For example, the conductance of the MTJ with different MgO thickness shows similar decay behavior and decay ratio. Similarly, the $K_{\parallel}$ resolved T(E) for the parallel and the anti-parallel

configuration show identical location of the hot-spots where there is a very high transmission coefficient [Figure 7.9].

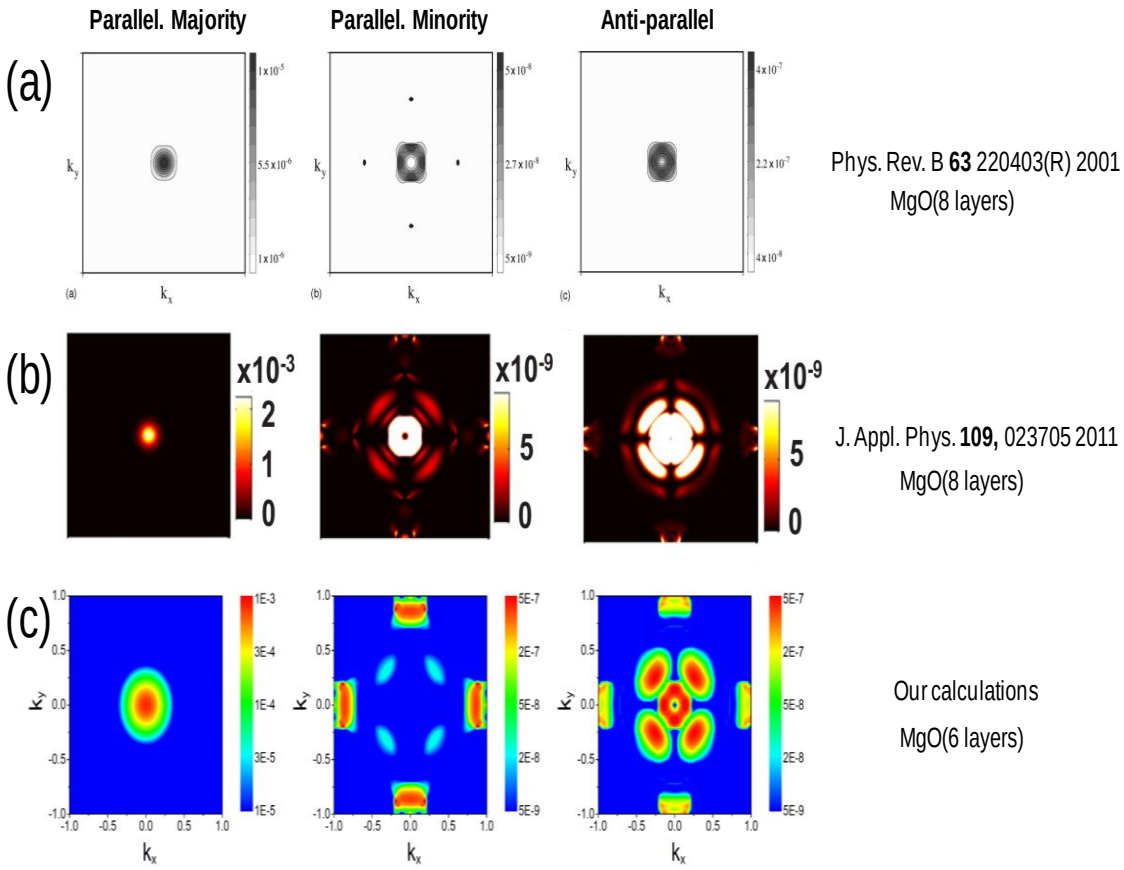

Figure 7.9 Benchmarking the calculation method by comparing with (a) one of the first results in the Fe/MgO/Fe structure (b) Very recent calculations using a similar approach (c) Our calculation results.[33, 152]

7.7 Effect of strain on the calculated TMR of Fe/MgO/Fe

The effect of 5% biaxial *xz*-strain on the junction conductance was calculated as shown in Figure 7.10(a) for different MgO barrier thicknesses. For the unstrained junction, both the parallel and anti-parallel conductance decreased exponentially with the number of MgO layers, as expected for tunneling transport. Though the conductance is sensitive to the details of the calculations,[152] our decay rate of 0.40 $Å^{-1}$ for the parallel configuration and 0.50 $Å^{-1}$ for the anti-parallel configuration agreed

well with the published values of 0.44 and 0.49 $Å^{-1}$, respectively.[152] Note that the faster decay rate for the anti-parallel configuration led to an increase in the TMR ratio with the number of layers, as shown in Figure 7.10(b). The different decay rate could be understood from the $k_{//}$-resolved transmission spectra in Figure 7.12. While majority-to-majority transport was dominated by states near the gamma point, no such states were available for minority-to-minority transport. The transmission spectrum for the minority states was dominated by a narrow circle around the gamma point, and by states at the edges of the Brillouin zone, in agreement with earlier calculations.[33] This could be understood from the Fe(100) surface spectral density at the Fermi energy [Figure 7.13] and from the complex band structure of MgO.[33] The complex MgO band structure showed that the decay rate was minimum in a small region around the gamma point and increased away from the gamma point.[33] Therefore, the decay rate in the MgO junction was higher for the minority states.

The application of 5% biaxial *xz*-strain increased the conductance for both the parallel and anti-parallel configurations [Figure 7.10(a)]. However, the increase was more pronounced for the anti-parallel configuration, and hence the TMR ratio decreased by a factor 10 to 30 depending on the MgO tunnel barrier thickness [Figure 7.10(b)]. Biaxial strain decreased the decay constants to 0.37 and 0.45 $Å^{-1}$ for the parallel and the anti-parallel configurations, respectively. In addition, the contact conductance — a measure of the number of active transport channels in the Fe(100) contacts and their coupling at the Fe(100)/MgO interface[160]— increased 10-fold for the minority channels, but only two-fold for the majority channels. The increase in the conductance by a factor of 1.3 to 3.7 and the decrease in decay rate for the parallel configuration could be attributed to a decrease in the MgO band gap. Indeed, the EHMO band gap for a six-layer MgO slab decreased from 7.29 eV to 7.02 eV, which

was comparable to the 0.11 eV decrease calculated by DFT-HSE03. The conductance for the anti-parallel configuration was more sensitive to biaxial strain, and increased by a factor of 7 for a four-layer MgO barrier and 5% strain, and by a factor of 61 for a 12-layer MgO barrier.

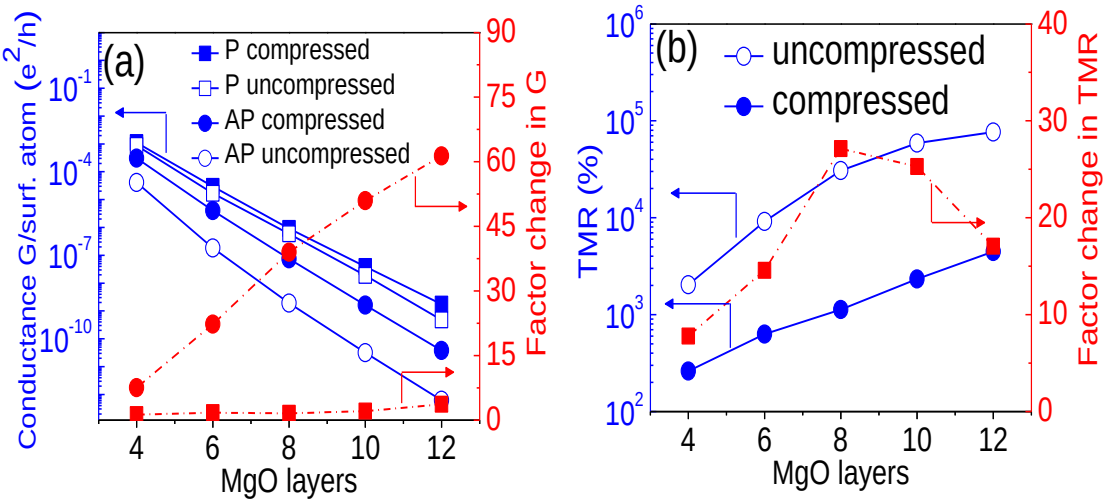

Figure 7.10 (a) Calculated conductance for a Fe(100)/MgO/Fe(100) tunneling junction as a function of the number of MgO layers. The conductance is shown for the parallel and the anti-parallel configurations for both the unstrained and the 5% biaxial *xz*-strain cases. The relative increase in the conductance after applying 5% biaxial *xz*-strain is also shown to facilitate comparison with the experimental data in Figure 7.7. For six MgO layers, the parallel conductance increases by a factor 1.74 from 0.65 to 1.14 nS, while the anti-parallel conductance increases by a factor 22.32 from 7 to 157 pS. (b) Optimistic TMR ratio $[(G_P-G_{AP})/G_{AP}$, where G_P and G_{AP} are the conductance of the parallel and the anti-parallel states, respectively] for the unstrained and the strained tunneling junctions as a function of the MgO thickness. To facilitate comparison with the experiments, the relative change in the TMR ratio is also shown and ranges from a factor of 7 to 27.

To compare the calculated changes in the TMR ratio and in the conductance with the experimental values, we have included the relative changes in Figure 7.10(b). The 22-fold increase in the anti-parallel conductance for 5% strain and for a six-layer (13 Å) MgO barrier was significantly larger than the experimental increase of 2.9 for a 20 Å MgO barrier. Furthermore, the 15-fold decrease in the calculated TMR ratio for a six-layer MgO barrier was larger than the experimental value of 4.8 for a 20 Å MgO

barrier. However, when the biaxial strain was reduced to 3.5% for the six-layer MgO junction, the agreement with the experiments improved [Figure 7.11]. The calculated increases in the parallel and anti-parallel conductance by factors 1.1 and 3.0, respectively could be compared with the experimentally measured increases by factors 1.7 and 2.9, respectively [Figure 7.7]. Also, the 2.7-fold decrease in the calculated TMR ratio matched the experimental value of 4.8 quite well. The qualitative implications were preserved even for smaller levels of biaxial strain in the MgO layer (2.5%).

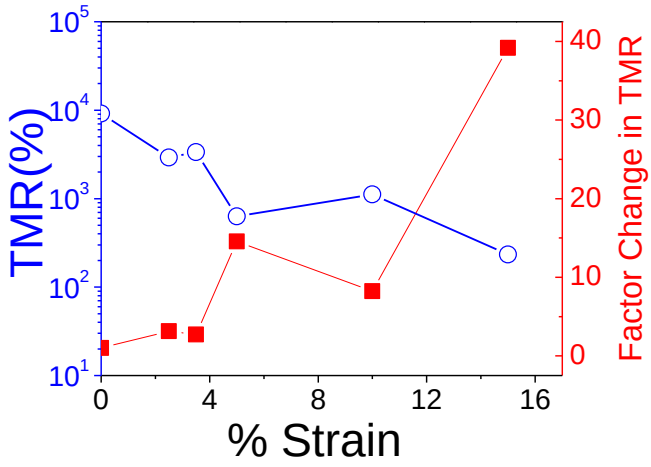

Figure 7.11 TMR and factor change in TMR for unstrained (0% strain) and different levels of strain in Fe/MgO/Fe with 6-layer MgO. For 3.5% strain, the relative change in TMR (right-axis) matches the experimental change in TMR.

7.7.1 Transmission spectra for strained and unstrained Fe/MgO/Fe

The more pronounced increase in the conductance for the minority channels and the anti-parallel configuration could be understood from the $k_{//}$-resolved transmission spectra, shown in Figure 7.12 for a six-layer MgO junction in the case of unstrained and a 3.5% biaxial strain. For the unstrained junction, majority transport was dominated by states near the gamma point. The $k_{//}$-resolved spectra for the

majority states were relatively unaffected by strain, except for a small broadening of the peak and an increase in the peak maximum from 0.846×10^{-3} to 0.853×10^{-3}.

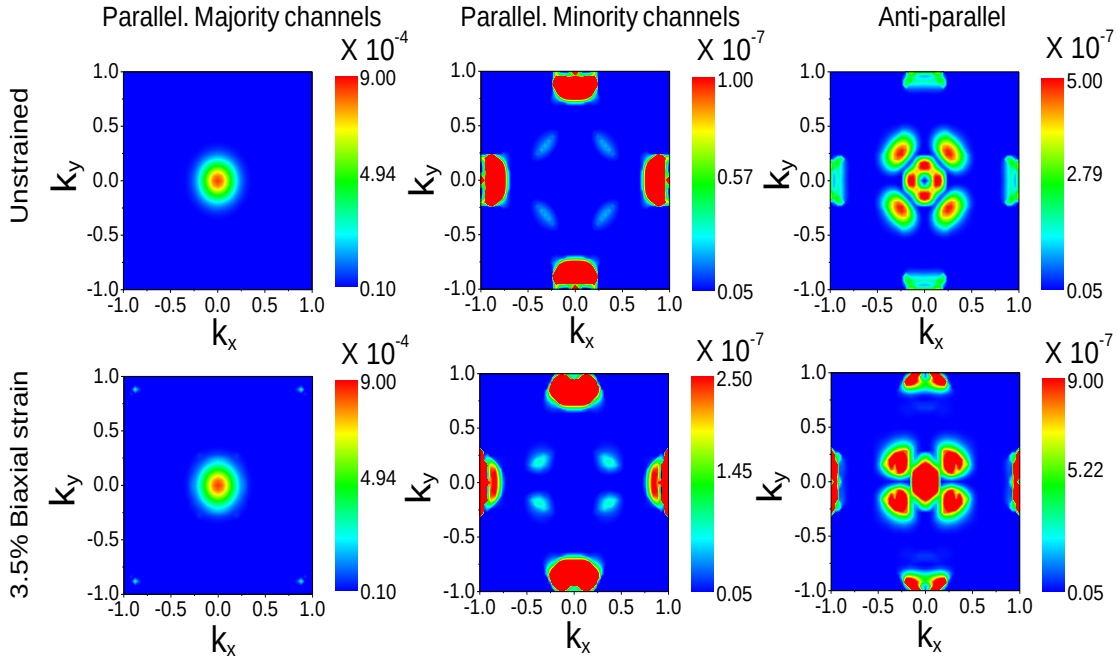

Figure 7.12 $k_{//}$-resolved transmission spectra for the various transport modes for a Fe(100)/MgO(6 layers)/Fe(100) junction. Biaxial strain decreases the lattice in the *x* and *z* directions by 3.5%, and expands the lattice in *y* direction by 1.6%. Transport for the majority channels is dominated by states near the gamma point, while states near the edge of the Brillouin zone dominate for the minority channels. Strain introduces transmission hot-spots near the k_y= 0 axis for the minority and the anti-parallel transmission spectra. Note the different scales for the various transmission spectra.

Minority transport, however, was dominated by a circle of states around the gamma point and by states near the Brillouin zone edge. Biaxial *xz*-strain broke the four-fold symmetry in the *xy* plane, and transmission hot-spots moved closer to the k_y= 0 axis. The change in the location of minority states at the Fermi energy is also illustrated by the Fe(100) spectral density in Figure 7.13. The minority states were concentrated in a narrow square region around the gamma point, with few states at the gamma point. In this region the decay constant for MgO was quite high. Biaxial strain increased the orbital overlap in the *x* direction and hence broadens the *d*-band. As can be seen in Figure 7.13, this moved minority states closer to the gamma point along the

k_x axis. The effect was even more pronounced in the transmission spectrum [Figure 7.12] and new hot-spots appeared near the k_y=0 axis. The change in the minority states was also reflected in a decrease in the Fe magnetic moment. For a six-layer Fe(100) slab, the EHMO magnetic moment per Fe decreased from 1.96 to 1.86 μ_B – again in good agreement with the 0.14 μ_B decrease calculated by DFT-HSE03.

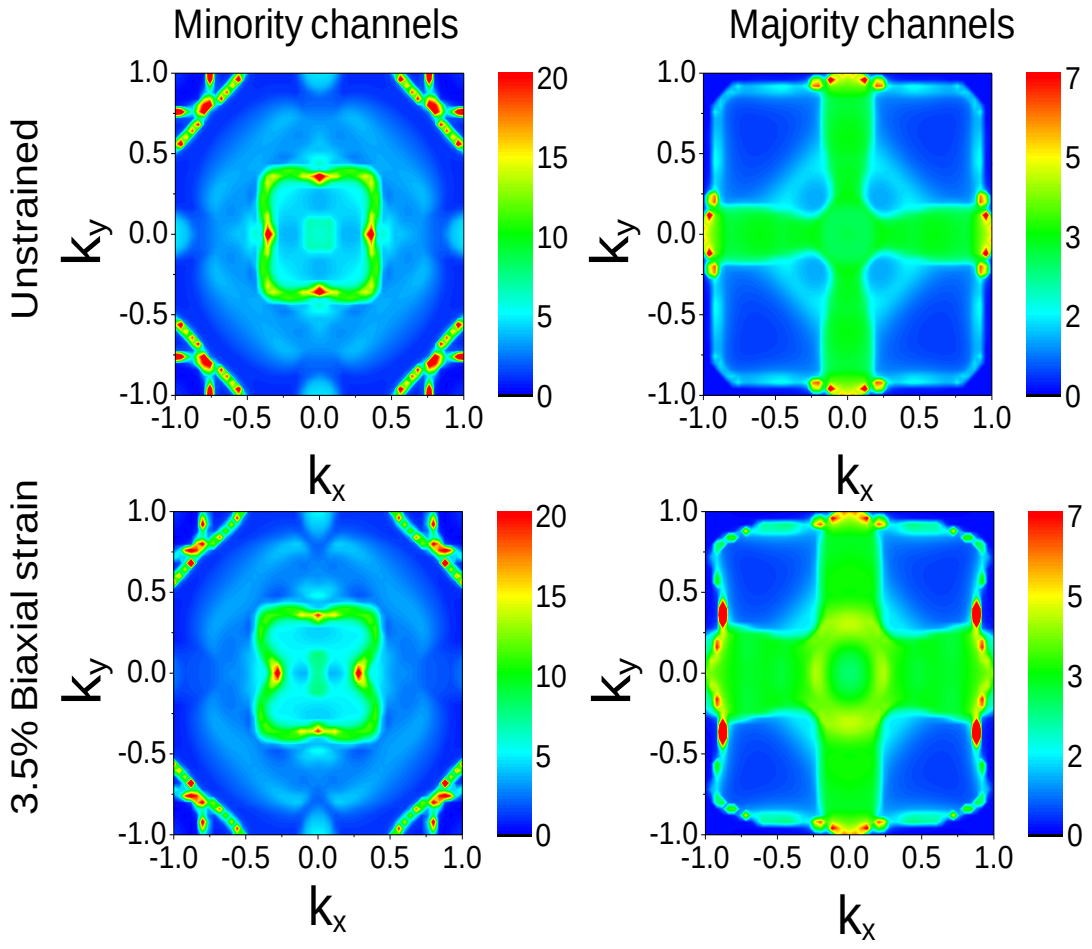

Figure 7.13 Effect of 3.5% biaxial *xz*-strain on the Fe(100) surface spectral density (number of states/eV/Å^2) at the Fermi energy for the minority and the majority states. While changes for the majority states are relatively minor, the minority states at (k_x, k_y)=(±0.4, 0.0) clearly moved closer to the gamma point. As explained in the text, this is consistent with a broadening of the minority band and a decrease in the spin polarization.

The above results also helped to explain the experimental voltage and temperature dependence of the TMR. It was reported that the transmission for the minority spin channel was sensitive at low biases; however, once the minority states

moved closer to the gamma point, the bias-dependent transmission was significantly suppressed at higher biases.[161] From our calculations we concluded that the biaxial strain moved the minority states closer to the gamma point. This, in turn, weakened the sensitivity of the minority states to the voltage and temperature, resulting in a diminished voltage and temperature dependence of R_{AP} and TMR.

7.8 Conclusions

We have demonstrated the effect of mechanical stress on the tunnelling properties of MTJs. The deposition of a DLC film with very high intrinsic stress over the junction reduced the TMR ratio as well as the junction resistance. The NEGF calculations reproduced both the increase in the conductances and the decrease in the TMR ratio when biaxial *xz*-strain was applied. The increase in the conductance for the parallel configuration could be attributed to a decrease in the MgO band gap by about 0.3 eV and the barrier thickness by 5%. The conductance for the anti-parallel configuration was significantly more sensitive to strain, and increased about 30 times faster than for the parallel configuration, decreasing the TMR ratio. The high sensitivity of the anti-parallel conductance to biaxial strain could be attributed to changes in the location of the Fe(100) minority states at the Femi level. When strain was applied, the *d*-band broadened and the minority states at the Fermi energy moved closer to the centre of the 2D Brillouin zone where transmission through the MgO barrier was higher. As a result, hot-spots appeared in the $k_{//}$-resolved transmission spectrum and the conductance for both the minority channel and the anti-parallel configuration increased rapidly. This study demonstrated the important effect of strain on the anti-parallel conductance, and suggested that strain engineering could further engineer MTJs. Specifically our proposed technique could reduce the resistance-area product for MgO-based read sensors with a sufficiently high TMR value.

The next chapter will study the tunnel magnetocapacitance (TMC) effect and the frequency-dependent TMR for different MTJs. Capacitance in MTJs is sensitive to interfacial charge accumulation and hence is very interesting to explore since interfacial properties are critical in determining MTJ performance.

Chapter 8 : Parallel-leaky capacitance equivalent circuit model for MgO based magnetic tunnel junctions

After studying the effect of strain on spin-dependent tunneling characteristics, we next look into the capacitance and its magnetic field dependence as well as the frequency dependence of TMR for several MTJs based on the MgO tunnel barrier.

8.1 Motivation

Magnetic tunnel junctions (MTJs) have played a key role in the development of hard disk drive (HDD) read heads as well as magnetic random access memories (MRAM).[110, 162, 163] For high speed applications, the product of resistance and capacitance (*RC* time constant) of MTJs plays an important role. Hence, capacitive measurements of MTJs become indispensable. Capacitance occurs when electrical conductors are separated by an insulator and its voltage dependence has been widely used to characterize a variety of physical properties. For example, properties such as the dielectric constant and loss of the insulating layer in metal-insulator-metal (MIM) structures are revealed by capacitance measurements. In order to characterize the density as well as the distribution of interface trap states at the oxide-semiconductor interface, capacitance-voltage (*C*-*V*) characterization methods have proven to be a very efficient technique.[164]

8.2 Introduction

With extremely thin dielectric materials (~20 Å) in MTJs, the capacitance is largely influenced by the interface properties of the structure as the electric field penetration becomes significant.[165] Since the interfaces are very critical in determining the tunneling magnetoresistance (TMR),[112, 129] which is one of the key attributes of MTJs, the study of capacitance can be a useful tool for a better understanding of MTJs. After theoretical predictions of spin-dependent capacitances in ferromagnetic systems,[166, 167] the tunneling magnetocapacitance (TMC) effect in Al_2O_3 based MTJs has been reported.[168-170] However, the experimental situation for the TMC effect in MgO based MTJs is less clear with one group suggesting the existence of the TMC effect and the other group showing the absence of TMC.[171, 172] The concept of negative interfacial capacitance is also controversial which has been introduced to account for the measured capacitance exceeding the geometric capacitance. For example, several reports in Al_2O_3 based systems have observed a positive interfacial capacitance.[170, 173, 174]

In this chapter we present the TMC measurements from MgO based MTJs and substantiate the magnetic field dependence of capacitance in MgO MTJs as observed for all our junctions consistently. A parallel-leaky capacitance (C_l)-based equivalent circuit has been proposed in large junction area MTJs in order to account for a larger value of measured capacitance than that of the geometric capacitance. In the modified equivalent circuit for MTJ, C_l is connected across the series combination of geometric and interfacial capacitance. The analysis of junctions with different levels of TMR suggested a higher C_l for low TMR junctions. The capacitance and frequency dependent characteristics of high TMR samples were compared with a low TMR sample having a highly leaky tunnel barrier. Using Cole-Cole plots it was shown that

the MTJ systems were capacitive, and impedance spectroscopy suggested that the experimental observations can be explained using an *RC* parallel network. Fitting was done with the Maxwell-Wagner capacitance model and the extracted field dependent parameters matched with the experimental values. The frequency and voltage dependence of TMR and TMC for the two junctions were also investigated.

8.3 Experimental methods

The MTJs with a structure of 100 Ta/300 $Ir_{22}Mn_{78}$/6 $Co_{40}Fe_{40}B_{20}$/30 $Co_{70}Fe_{30}$/8 Ru/27 $Co_{70}Fe_{30}$/8 Mg/14 MgO/20 $Co_{40}Fe_{40}B_{20}$/50 Ta/50 Ru (all thickness in Å) were grown using magnetron sputtering in an ultra-high vacuum chamber. The MgO barrier was formed by the reactive sputter deposition of Mg in Ar-O_2 plasma (~2% oxygen). The Mg layer prevents the oxidation of the underlying ferromagnetic electrode and is converted to MgO by reactive oxygen introduced into the sputter chamber during the deposition of the MgO layer.[35, 112] The samples were annealed at 300 ˚C for 30 minutes under 1 T magnetic field and then MTJs were fabricated in a current perpendicular-to-plane (CPP) configuration using a combination of Ar ion-milling and photolithography processes. The capacitance was measured using an Agilent E4980A Precision LCR meter in the frequency range between 100 Hz to 2 MHz and the temperature dependence was studied using a cryostat under high vacuum conditions (< 1×10^{-7} Torr). Prior to every measurement the effect of stray capacitances and inductances from the measurement probes and co-axial cables were compensated using standard open and short corrections.[175]

8.4 Negative TMC in MTJs

A typical TMC characterization is shown in Figure 8.1(a) along with a plot of the junction resistance as a function of magnetic field. All our MTJs showed a negative TMC value smaller than the TMR value as reported previously.[171] The negative TMC ratio indicated that a higher capacitance value for the parallel (P) state than that for the antiparallel (AP) state as predicted by the calculations.[176] Although some of the earlier reports suggest interfacial charge accumulation to be independent of the conduction process, a recent report has proposed spin dependent charge accumulation at the interfaces as a reason for the observation of magnetic field dependent capacitance or TMC in MTJs.[168] A simple qualitative way to understand the negative TMC is to consider that the capacitance follows the conductance.[175] For the P configuration the higher value of conductance results in a greater amount of charge accumulation and hence a capacitance value more than that of the AP state. Along with the magnetic field dependence, the voltage or temperature dependence of capacitance has also been observed to be in opposite sense to that of the resistance of the MTJs. It is clear that the TMC effect is correlated with the TMR effect from the fact that the switching fields in Figure 8.1(a) for resistance and capacitance match well. However, we did not observe any strong correlation between the TMR and the TMC values. Rather we found the *RC* time constant to be proportional to the TMR ratio as shown in Figure 8.1(c).

The *RC* time constant of the MTJs has similar magnetic field dependence to the TMR as shown in Figure 8.1(b), suggesting different switching speeds between the P and AP states. Figure 8.1(c) shows a plot of the relative change of the *RC* time constant for the P and AP states for various samples which is defined by:

$$TM_{RC} = \frac{(RC)_{AP} - (RC)_P}{(RC)_P} \times 100 \quad (8.1)$$

.

The value of TM_{RC} was higher for devices with a higher TMR, which indicated a larger asymmetry in the switching speed between the P and AP states for a high TMR sample. The synthetic antiferromagnet (SAF) part of the structure (CoFe/Ru/CoFe) also contributed to the change of the capacitance as can be seen between 0 and 0.2 T in Figure 8.1(a). In such a magnetic multilayer without any dielectric, only interfacial charge accumulation can lead to the field dependent capacitance.

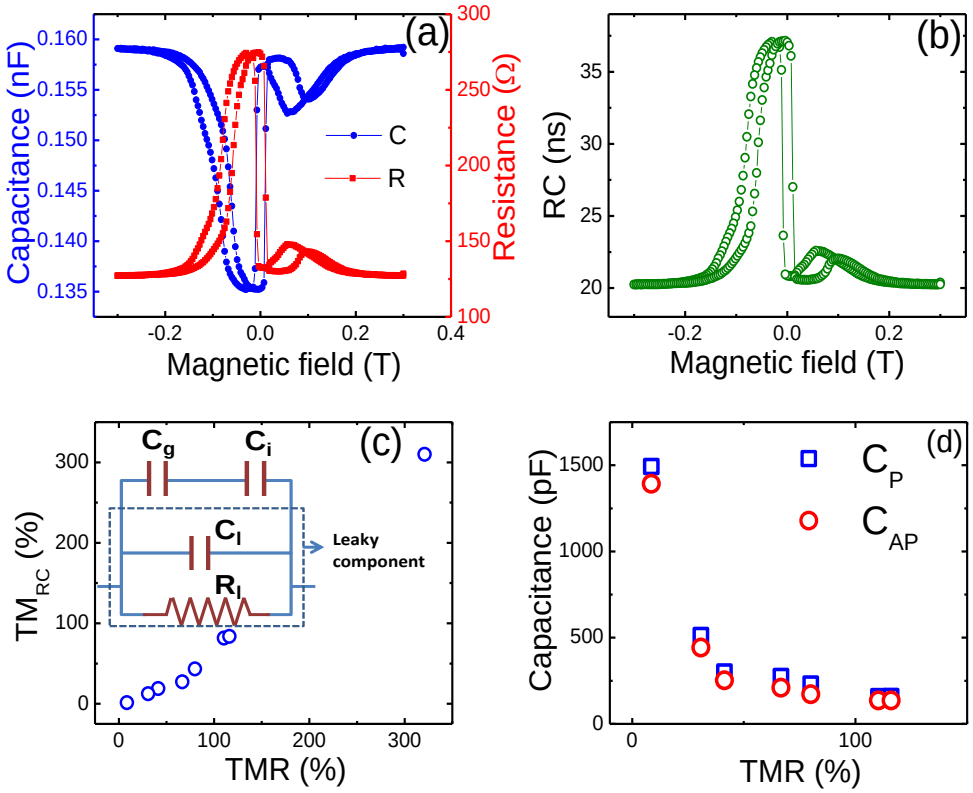

Figure 8.1 (a) The magnetic field dependence of resistance and capacitance of an MTJ with the junction area of ~70 μm^2. The TMR is 116%, while the TMC is 17% at 1 MHz. The TMR ratio is defined by $(R_{AP}-R_P)/R_P$, where R_P and R_{AP} are the junction resistance in the P and AP alignment, respectively. The TMC ratio is defined by $(C_P-C_{AP})/C_{AP}$, where C_P and C_{AP} are the junction capacitance in the P and AP alignment, respectively. (b) The magnetic field dependence of the *RC* time constant for the same device with a relative difference of 83% between the P and AP states. (c) The dependence of TM_{RC} on the TMR shows greater asymmetry in *RC* time constant for higher TMR devices. The equivalent circuit for the MTJ with a parallel leaky capacitor across the series combination of C_g and C_i is also shown in the inset. (d) The relationship between the capacitance and the TMR of the junctions. All data are from room temperature measurements.

8.5 Equivalent RC circuit for MTJs

The concept of negative interfacial capacitance for the MgO tunnel junctions was introduced in order to explain a larger effective capacitance than the geometrical capacitance.[171, 172] However, the physical origin of negative interfacial capacitance is not clear and several reports in Al_2O_3 based MTJs and MIM structures have consistently demonstrated a positive interfacial capacitance value.[170, 173, 174] There have been several reports of negative capacitance in Schottky barriers.[177-179] In these cases, however, at high bias voltage injected high energy carriers knock out charges trapped at interfaces resulting in the depletion of interfacial charges instead of accumulation similar to impact ionization. This leads to reduction in the measured capacitance with increasing bias voltage, and a negative capacitance value is induced when the bias voltage is sufficiently high. There has been no report showing such evidence in MTJs. Furthermore, if the geometric capacitance (C_g) and interfacial capacitance (C_i) are the only two capacitance components in MTJs, the observation of a positive capacitance value in the metallic pseudo-spin-valve[180] and nanowires[181] cannot be explained as the C_g is absent.

We propose an equivalent circuit for MTJs based on a parallel-leaky capacitance (C_l) in parallel to the series combination of C_g and C_i as shown in the inset of Figure 8.1(c). The MTJs are generally highly leaky capacitors with very high leakage currents. For MOS structures several time domain techniques have been proposed to extract accurate values of capacitance for highly leaky dielectrics.[182-184] However, those are out of the scope for the present work. Using this equivalent circuit, the total or the measured capacitance (C_m) for MTJs is given by

$$C_m = C_l + \frac{C_g C_i}{C_g + C_i} . \tag{8.2}$$

The value of C_l is similar to C_m, since the C_g is typically much smaller than C_m. The leaky components include C_l and a resistor R that promote a net flow of current through the MTJ. Because of large junction sizes ranging from 70 to 2100 μm^2, it is highly possible to have localized spots across the junction area in which there is more accumulation of charges, resulting in multiple effective capacitors connected in parallel. The multiple capacitances are represented by C_l in our model, which contributes most to the measure capacitance value because of parallel connections. More leaky MTJs with higher capacitance values tend to show less TMR values [Figure 8.1(d)] and demonstrate less bias voltage dependence of TMR/TMC, as will be discussed later. The higher capacitance can be attributed to the presence of additional leakage paths that reduce the TMR ratio. The above observation provides support that our model describes the MTJs correctly. The basic difference between the conductance (1/resistance) and the capacitance is that the former represents the delocalized states and the latter is more sensitive to the localized states. The observed low TMC values compared to the TMR ratios might suggest the presence of localized trap states in MTJs. The effective capacitor due to these localized states is in parallel to C_g and is represented by C_l.

8.6 Impedance spectroscopy

In order to validate our equivalent circuit, we compared the characteristics of a low and a high TMR junction using impedance measurements ($Z = R + jX$). Cole-Cole plots are usually used to represent the lossy term versus the storage term of a system as a function of frequency or time.[185] The Cole-Cole diagrams for the MTJs are plotted with the resistance (R) and the reactance (X) at different frequencies from 5 kHz to 2 MHz as shown in Figure 8.2. Both the low and high TMR junctions are capacitive in

the P and AP states, as the trajectory lies in the fourth quadrant. The data for the high TMR device can be fitted with a semi-circle; however, the fitting using a semi-circular function is not possible for the low TMR device (high C_l), indicating deviation from the ideal Maxwellian behavior of dielectric.[186]

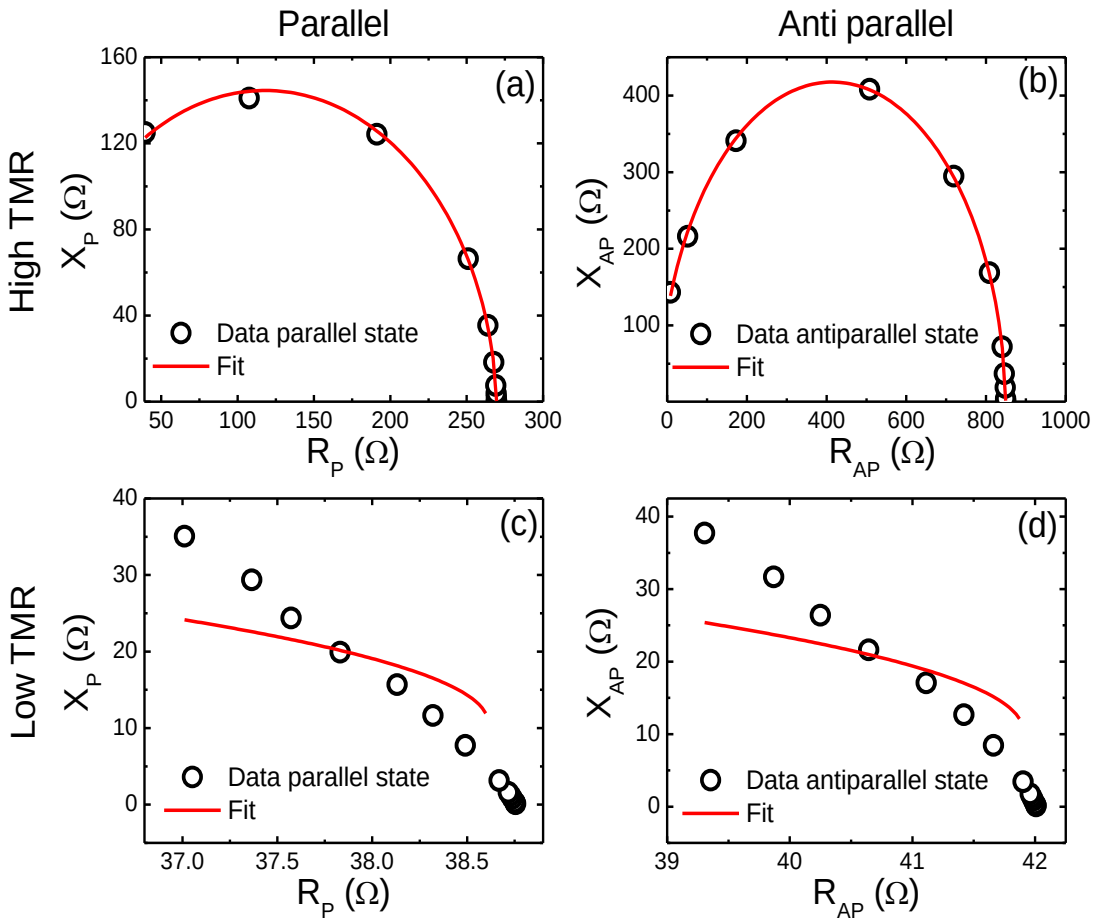

Figure 8.2 Cole-Cole plots for low and high TMR junctions (10 kHz to 2 MHz). For the high TMR (300%) junction with the junction area of ~70 μm^2 in (a) and (b), the semi-circular fits match well with the data, while for the low TMR (8%) junction with the junction area of ~70 μm^2, the data significantly deviates from semicircular fits in (c) and (d). All data are at 20 K.

The frequency dependence of the real and imaginary parts of the impedance is shown in Figure 8.3 for the high TMR [Figure 8.3(a)] and the low TMR [Figure 8.3(b)] devices. With both the MTJ systems equivalent to the *RC* parallel circuit, their frequency dependence plots can be fitted using the Maxwell-Wagner capacitance

model,[180, 181, 187, 188] in which two *RC* networks are connected in series with one part being magnetic field dependent and the other being field independent. The field independent part can be removed by taking the difference of the impedances in the P and AP states. The change of the impedance between the P and the AP states can be represented as $\Delta Z=\Delta R+j\Delta X$ where

$$\Delta R = \left(\frac{R_{AP}}{1+4\pi^2 f^2 R_{AP}{}^2 C_{AP}{}^2} - \frac{R_P}{1+4\pi^2 f^2 R_P{}^2 C_P{}^2} \right) \tag{8.3}$$

$$\Delta X = -2\pi f \left(\frac{C_{AP} R_{AP}{}^2}{1+4\pi^2 f^2 R_{AP}{}^2 C_{AP}{}^2} - \frac{C_P R_P{}^2}{1+4\pi^2 f^2 R_P{}^2 C_P{}^2} \right) \tag{8.4}$$

The extracted fitting parameters are very close to the experimentally obtained values as shown in Fig 8.3(c) and 8.3(d), which in turn supports the authenticity of the *RC* parallel network for MTJs with low as well as high TMR. The C_P and C_{AP} are equivalent to C_m at different fields, which is a combination of the three capacitors (C_g, C_l, and C_i). Since C_l is close to the C_m value, the extracted C_P and C_{AP} give an idea of the C_l in the MTJs.

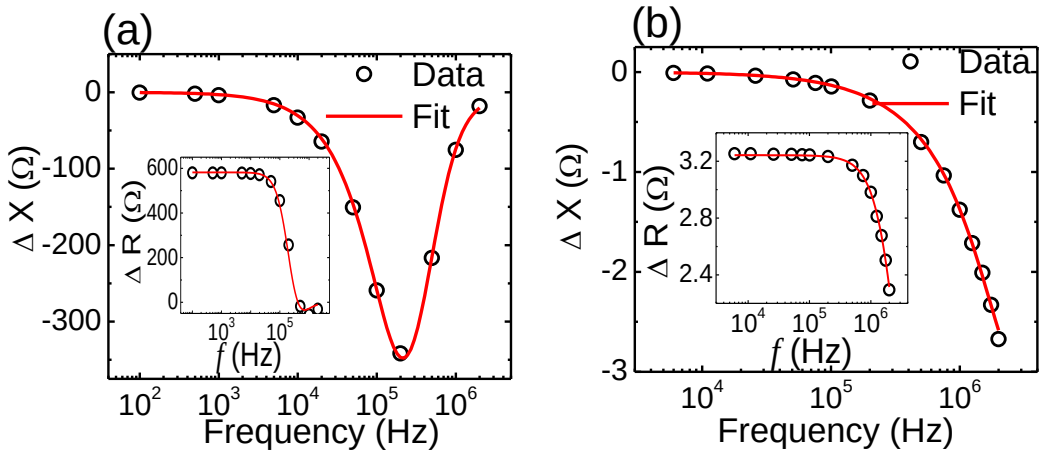

(c)

	Fitting parameters	Experimental data
C_P	0.847 nF	0.783 nF
C_{AP}	0.757 nF	0.765 nF
R_P	261.660 Ω	268.606 Ω
R_{AP}	848.479 Ω	835.944 Ω

(d)

	Fitting parameters	Experimental data
C_P	1.671 nF	1.745 nF
C_{AP}	1.356 nF	1.622 nF
R_P	37.995 Ω	38.756 Ω
R_{AP}	43.985 Ω	42.009 Ω

Figure 8.3 The ΔX (Ω) values for the high TMR (300%) and the low TMR (8%) junctions are shown in (a) and (b), respectively. ΔR (Ω) is shown in the insets. For both the junctions, the fitting parameters are close to the experimental values as shown in (c) and (d) below the corresponding figures. All data are at 20 K.

8.7 Frequency and bias dependence of TMR

Finally, the frequency and bias voltage dependence were carried out. Figure 8.4(a) reveals that the different MTJ devices with high TMR values have very little frequency dependence (at room temperature as well as at low temperature). However, for a leaky tunnel barrier we observed a sharp drop in the value of TMR at frequencies higher than 300 kHz, as shown in Figure 8.4(b) regardless of the temperature. A similar drop in TMR with frequency has been observed in thick tunnel barriers and attributed to capacitive leakage paths that overwhelms the spin dependent conduction process at higher frequencies.[171] The voltage dependence of the ratio of TMR and TMC is suppressed in the leaky tunnel barrier [Figure 8.4(d)] compared to that of a

high TMR junction in Figure 8.4(c). Another point to note is that the TMC curve overlaps the TMR curve for the low TMR junction in Figure 8.4(d), while the TMC is less sensitive to bias voltage than TMR for the high TMR device in Figure 8.4(c). Both effects can be attributed to the fact that the low TMR device closely resembles an ohmic-like junction with a very high leakage current compared to an ideal tunnel junction with a high TMR ratio.

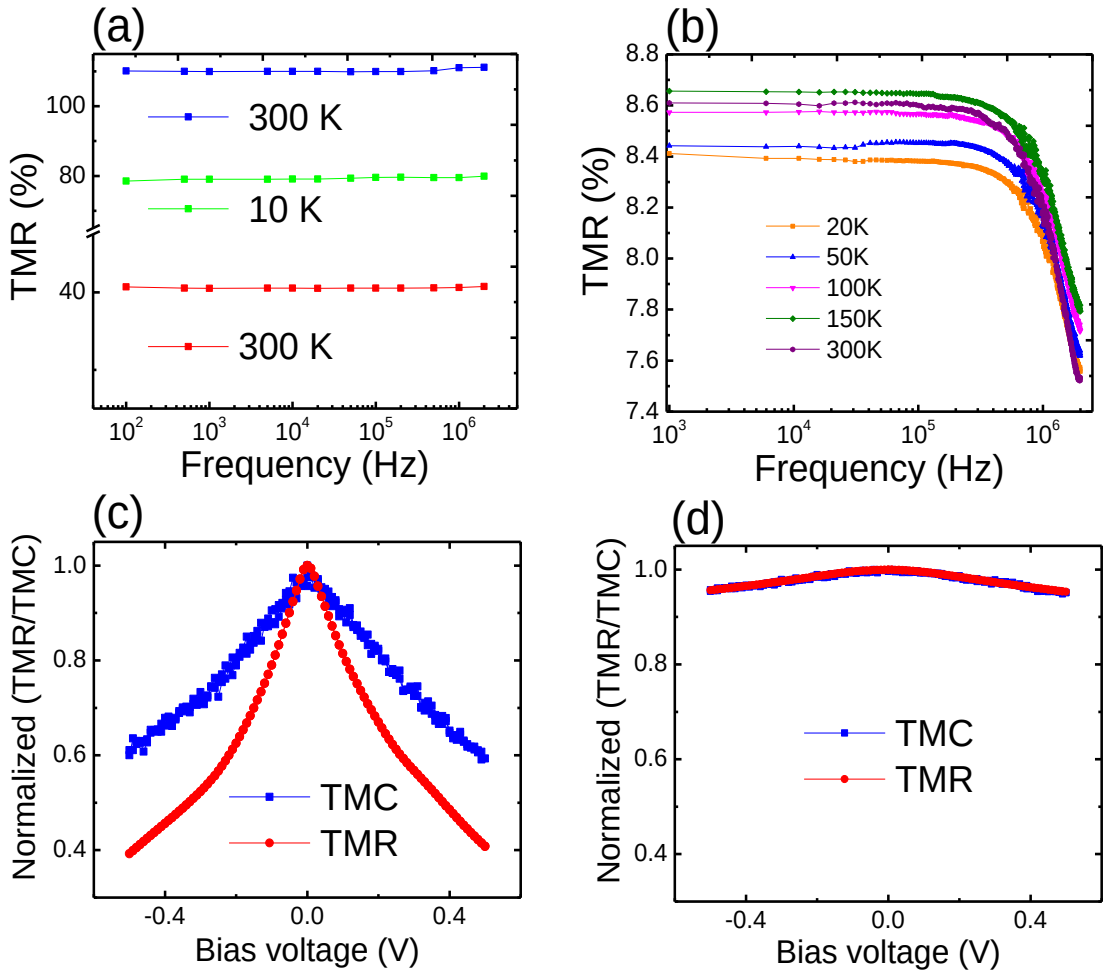

Figure 8.4 Frequency dependence of TMR for high TMR junctions (a) and a low TMR device (b). Normalized bias dependence of both TMC and TMR for the high TMR (300%) device (c) and the low TMR (8%) device (d) at 20 K.

In conclusion, our results clearly demonstrate the observation of TMC in MgO based MTJs. An equivalent MTJ circuit is proposed with an additional capacitance in

parallel with the series combination of interfacial and geometric capacitances, which can explain the measured capacitance values of different devices with various TMR ratios. Fitting using the Maxwell-Wagner capacitance model also validates the *RC* parallel circuit for the MTJs with extracted parameters close to the experimental values.

With this chapter we conclude the experimental part of this thesis. The next chapter will discuss all the goals achieved in this work and will also include suggestions and recommendations for future experiments.

Chapter 9 : Conclusions and recommendations for future work

In conclusion we have studied spin-dependent transport in magnetic tunneling systems and demonstrated interesting mechanisms for physics as well as applications.

Conclusions

Magnetic granular multilayers

In our work, we have shown the effect of magnetic field on electrical properties as well as the effect of electric field on magnetic properties. With magnetic fields, we were able to control the RS characteristics of Co/Al_2O_3 multilayers and the mechanism was explained using a theoretical model based on carrier injection. A high electric field was shown to decrease the granule magnetization along with a random exchange of oxygen atoms that could either reduce or enhance the net magnetic moment. The possibility of magnetization enhancement with oxygen impurities was supported with theoretical calculations. The electric field changes the *3d* orbital occupation of the Co granules which in turn changes the magnetization of the system.

Magnetic tunnel junctions

Substrate bias was shown as a very useful knob in magnetron sputtering for changing the interfacial structure as well as the film composition in Al_2O_3-based MTJs. However, changes in the film composition should be accounted for. The tunneling characteristics of MgO-based MTJs have been changed using highly stressed DLC films. The possibility of strain-induced reduction of the junction resistance in MgO-

based MTJs is encouraging for read sensor applications. High frequency TMR also provided interesting features in MTJs with leaky tunnel barriers. The TMR of a leaky MTJ drops sharply at higher frequencies.

Suggestions for future experiments

Magnetic granular multilayers

- Our work has used micro-dimensional systems to show these effects; however, studying systems with lateral dimensions in the nm range will be very interesting.
- Further optimization of the granular system and its magnetic field controlled switching will allow for multi-level data storage applications.
- Changes in the magnetization with electric field provide energy efficiency combination of MTJ and granular barrier and will be interesting to explore – both for magnetic fields as well as electric switching and capacitive measurements.

Magnetic tunnel junctions

- Strategies where the level of strain can be controlled are more promising to control spin transport as well as to study. The use of ferroelectric films such as PZT will provide a more flexible approach to tune the device properties.
- Atomic layer deposition is a thin-film deposition technique based on sequential, self-limiting surface reactions, providing the ability to accurately control numerous film properties such as thickness, morphology, crystallinity, conformality, and electrical properties. It will be quite interesting to compare the tunneling, reliability and structural properties of atomic layer deposition

(ALD) and physical vapour deposition produced barriers as well as all other layers. The response of ALD barriers to thermal annealing as well as diffusion of different elements will be new.

- For MgO films, the deposition rate was significantly reduced (a few Å in 15 minutes) with the application of substrate bias (RF), even with the minimum power possible. Using pulsed bias with very small duty cycles, it might be possible to tune MgO properties for improved MTJ reliability as well as tunneling characteristics.
- Though experimentally extremely challenging, application of gate bias using side gates in shadow mask based MTJs will be an interesting way to control the tunnel current using voltage. Such a device would resemble a three-terminal transistor and the possibility of gate control of the tunnel current.
- All the above studies could be performed for the Heusler alloys such as Co_2MnSi and Co_2MnAl which have generated a lot of interest due to their half-metallic properties.
- The above studies can also be performed in perpendicular magnetic anisotropy materials and devices which are attracting a lot of attention especially for applications like MRAM.

List of publications

Main contribution

1. Electric field induced magnetization changes in Co/Al_2O_3 granular multilayers Ajeesh M. Sahadevan, Alan Kalitsov, Kalon Gopinadhan, Charanjit S. Bhatia, Julian Velev and Hyunsoo Yang - *Physical Review B* (to be rebutted).
2. Parallel-leaky capacitance equivalent circuit model for MgO magnetic tunnel junctions- Ajeesh M. Sahadevan, Kalon Gopinadhan, Charanjit S. Bhatia, and Hyunsoo Yang – *Applied Physics Letters* **101**, 162404 (2012).
3. Biaxial strain effect of spin-dependent tunneling in MgO magnetic tunnel junctions- Ajeesh M. Sahadevan, Ravi K. Tiwari, Gopinadhan Kalon, Charanjit S. Bhatia, Mark Saeys, and Hyunsoo Yang - *Applied Physics Letters* **101**, 042407 (2012).
4. Magnetic field control of hysteretic switching in Co/Al_2O_3 multilayers by carrier injection- Alan Kalitsov, Ajeesh M. Sahadevan, S. Narayana Jammalamadaka, Gopinadhan Kalon, Charanjit S. Bhatia, Guangcheng Xiong, and Hyunsoo Yang - *AIP Advances* **1**, 042158 (2011).
5. Substrate bias effect on AlOx-based magnetic tunnel junctions- Ajeesh M Sahadevan, Jae S Son, Hyunsoo Yang, Aaron J Danner and Charanjit S Bhatia - *Journal of Physics: Conference Series* **266**, 012105 (2011).

List of conference presentations

Main contribution

1. "Evidence of inelastic tunneling in magnetic tunnel junctions via capacitance-voltage characteristics"- Ajeesh M. Sahadevan, Kalon Gopinadhan, Charanjit S. Bhatia, and Hyunsoo Yang- **19th International Conference on Magnetism**, Busan, Korea, July 8 – July 13, 2012.
2. "Biaxial strain effect of spin-dependent tunneling in MgO magnetic tunnel junctions."- Ajeesh M. Sahadevan, Ravi K. Tiwari, Gopinadhan Kalon, Charanjit S. Bhatia, Mark Saeys, and Hyunsoo Yang- **International Conference of Young Researchers on A**
3. **dvanced Materials, ICYRAM 2012,** Singapore, July 1- July 6, 2012- **Best Poster award.**
4. "Magnetization fluctuations in magnetic granular systems by electric field induced oxygen migration."- Ajeesh M. Sahadevan, Alan Kalitsov, Kalon Gopinadhan, Charanjit S. Bhatia and Hyunsoo Yang **International Magnetics Conference, INTERMAG 2012**, Vancouver, Canada, May 7 – May 11, 2012.
5. "Magnetic field controlled threshold resistive switching in magnetic granular systems."- Ajeesh M. Sahadevan, Alan Kalitsov, S. Narayana Jammalamadaka, Gopinadhan Kalon, Charanjit S. Bhatia, Guangcheng Xiong, and Hyunsoo Yang- **56th Conference on Magnetism and Magnetic Materials, Scottsdale, Arizona, USA, October 30 – November 3, 2011.**
6. "Substrate bias effect on AlOx-based magnetic tunnel junctions grown on Ge buffer layers."- Ajeesh M Sahadevan, Jae S Son, Hyunsoo Yang, Aaron J Danner and Charanjit S Bhatia- **2nd International Symposium on Advanced**

Magnetic Materials and Applications (ISAMMA 2010), Sendai, Japan, July 12 – July 16, 2010.

Awards and others presentations

1. Best poster award at the International Conference of Young Researchers on Advanced Materials (ICYRAM) - (Magnetic materials and spintronics session), Singapore, 2012.
2. Invitation for a talk at the 4th Worldwide University Network International Conference on Spintronics, Sydney Australia 2012.
3. IEEE magnetics summer scholar, Dresden, 2010 - organized by IEEE for graduate students doing research in magnetism across the world.
4. Student Travel Award for MMM, Arizona 2011 and ISAMMA, Sendai, 2010.

References:

[1] S. Loth, S. Baumann, C. P. Lutz, D. M. Eigler, and A. J. Heinrich, Science **335**, 196 (2012).

[2] E. Y. Tsymbal and I. Zutic, *Handbook of Spin Transport and Magnetism* (Chapman and Hall/CRC, 2011).

[3] M. Johnson, *Magnetoelectronics* (Elsevier, Oxford, 2004).

[4] G. W. Burr, B. N. Kurdi, J. C. Scott, C. H. Lam, K. Gopalakrishnan, and R. S. Shenoy, IBM J. Res. Dev. **52**, 449 (2008).

[5] G. Campardo, F. Tiziani, and M. Iaculo, *Memory Mass Storage* (Springer, 2011).

[6] http://www.ewh.ieee.org/r6/scv/mag/MtgSum/Meeting2010_05.html.

[7] *NAND Flash: Can It Meet the Growing Storage Capacity Demands of the Laptop PC Market?* (Seagate, 2011).

[8] www.imit.kth.se/info/SSD/KMF/IM2654/MRAM.ppt.

[9] M. Sarin, *An Analysis of MRAM Market* (VLSI Consultancy, 2006).

[10] B. Friedrich and D. Herschbach, Physics Today **56**, 53 (2003).

[11] N. F. Mott, Proc. R. Soc. London A **156**, 368 (1936).

[12] A. Fert and I. A. Campbell, Phys. Rev. Lett. **21**, 1190 (1968).

[13] P. Grünberg, R. Schreiber, Y. Pang, M. B. Brodsky, and H. Sowers, Phys. Rev. Lett. **57**, 2442 (1986).

[14] S. S. P. Parkin, Appl. Phys. Lett. **61**, 1358 (1992).

[15] W. P. McCray, Nat. Nanotechnol. **4**, 2 (2009).

[16] http://folk.uio.no/yurig/Nanotechnology/GMR/GMR.pdf.

[17] T. M. Nakatani, N. Hase, H. S. Goripati, Y. K. Takahashi, T. Furubayashi, and K. Hono, IEEE Trans. Magn. **48**, 1751 (2012).

[18] J. G. Simmons, J. Appl. Phys. **34**, 1793 (1963).

[19] E. R. Nowak, M. B. Weissman, and S. S. P. Parkin, Appl. Phys. Lett. **74**, 600 (1999).

[20] R. Meservey, D. Paraskevopoulos, and P. M. Tedrow, Phys. Rev. Lett. **37**, 858 (1976).

[21] R. Meservey, P. M. Tedrow, and P. Fulde, Phys. Rev. Lett. **25**, 1270 (1970).

[22] M. Julliere, Phys. Lett. A **54**, 225 (1975).

[23] T. Miyazaki and N. Tezuka, J. Magn. Magn. Mater. **139**, L231 (1995).

[24] J. S. Moodera, L. R. Kinder, T. M. Wong, and R. Meservey, Phys. Rev. Lett. **74**, 3273 (1995).

[25] M. B. Stearns, J. Magn. Magn. Mater. **5**, 167 (1977).

[26] I. I. Oleinik, E. Y. Tsymbal, and D. G. Pettifor, Phys. Rev. B **65**, 020401 (2001).

[27] J. M. De Teresa, A. Barthelemy, A. Fert, J. P. Contour, F. Montaigne, and P. Seneor, Science **286**, 507 (1999).

[28] S. Parkin, MRS Bulletin **31**, 389 (2006).

[29] S. S. P. Parkin, K. P. Roche, M. G. Samant, P. M. Rice, R. B. Beyers, R. E. Scheuerlein, E. J. O'Sullivan, S. L. Brown, J. Bucchigano, D. W. Abraham, Y. Lu, M. Rooks, P. L. Trouilloud, R. A. Wanner, and W. J. Gallagher, J. Appl. Phys. **85**, 5828 (1999).

[30] W. G. Wang, C. Ni, G. X. Miao, C. Weiland, L. R. Shah, X. Fan, P. Parson, J. Jordan-sweet, X. M. Kou, Y. P. Zhang, R. Stearrett, E. R. Nowak, R. Opila, J. S. Moodera, and J. Q. Xiao, Phys. Rev. B **81**, 144406 (2010).

[31] S. Yuasa and D. D. Djayaprawira, J. Phys. D: Appl. Phys. **40**, R337 (2007).

[32] D. X. Wang, C. Nordman, J. M. Daughton, Z. H. Qian, and J. Fink, IEEE Trans. Magn. **40**, 2269 (2004).

[33] J. Mathon and A. Umerski, Phys. Rev. B **63**, 220403 (2001).

[34] W. H. Butler, X. G. Zhang, T. C. Schulthess, and J. M. MacLaren, Phys. Rev. B **63**, 054416 (2001).

[35] S. S. P. Parkin, C. Kaiser, A. Panchula, P. M. Rice, B. Hughes, M. Samant, and S.-H. Yang, Nat. Mater. **3**, 862 (2004).

[36] S. Yuasa, T. Nagahama, A. Fukushima, Y. Suzuki, and K. Ando, Nat. Mater. **3**, 868 (2004).

[37] S. Ikeda, J. Hayakawa, Y. Ashizawa, Y. M. Lee, K. Miura, H. Hasegawa, M. Tsunoda, F. Matsukura, and H. Ohno, Appl. Phys. Lett. **93** (2008).

[38] J. J. Cha, J. C. Read, J. W. F. Egelhoff, P. Y. Huang, H. W. Tseng, Y. Li, R. A. Buhrman, and D. A. Muller, Appl. Phys. Lett. **95**, 032506 (2009).

[39] Y. Liu, A. N. Chiaramonti, D. K. Schreiber, H. Yang, S. S. P. Parkin, O. G. Heinonen, and A. K. Petford-Long, Phys. Rev. B **83**, 165413 (2011).

[40] S. Yuasa, Y. Suzuki, T. Katayama, and K. Ando, Appl. Phys. Lett. **87**, 242503 (2005).

[41] K. Kobayashi and H. Akimoto, FUJITSU SCIENTIFIC & TECHNICAL JOURNAL **42**, 139 (2006).

[42] S. Yuasa, A. Fukushima, H. Kubota, Y. Suzuki, and K. Ando, Appl. Phys. Lett. **89**, 042505 (2006).

[43] D. Mazumdar, Brown University, 2007.

[44] J. C. Slonczewski, Phys. Rev. B **39**, 6995 (1989).

[45] W. Thomson, Proc. R. Soc. London **8**, 546 (1856).

[46] M. N. Baibich, J. M. Broto, A. Fert, F. N. Vandau, F. Petroff, P. Eitenne, G. Creuzet, A. Friederich, and J. Chazelas, Phys. Rev. Lett. **61**, 2472 (1988).

[47] G. Binasch, P. Grunberg, F. Saurenbach, and W. Zinn, Phys. Rev. B **39**, 4828 (1989).

[48] J. C. Slonczewski, J. Magn. Magn. Mater. **159**, L1 (1996).

[49] L. Berger, Phys. Rev.B **54**, 9353 (1996).

[50] E. B. Myers, D. C. Ralph, J. A. Katine, R. N. Louie, and R. A. Buhrman, Science **285**, 867 (1999).

[51] S. I. Kiselev, J. C. Sankey, I. N. Krivorotov, N. C. Emley, R. J. Schoelkopf, R. A. Buhrman, and D. C. Ralph, Nature **425**, 380 (2003).

[52] A. Driskill-Smith and Y. Huai, (Grandis, 2007).

[53] J. Inoue and S. Maekawa, Phys. Rev. B **53**, 11927 (1996).

[54] X. G. Zhang, Z. C. Wen, H. X. Wei, and X. F. Han, Phys. Rev. B **81**, 155122 (2010).

[55] R. Waser and M. Aono, Nat. Mater. **6**, 833 (2007).

[56] H. Akinaga and H. Shima, Proc. IEEE **98**, 2237 (2010).

[57] A. Sawa, Mater. Today **11**, 28 (2008).

[58] P. M. Martin, *Handbook of deposition technologies for films and coatings* (Elsevier, 2009).

[59] L. I. Maissel and R. Glang, *Handbook of thin film technology* (McGraw-Hill, 1970).

[60] http://www.d2inlinesolutions.com/technology/sputtering.html.

[61] http://www.ajaint.com/.

[62] http://medicine.tamhsc.edu/basic-sciences/sbtm/afm/principles.php.

[63] http://www.cds.caltech.edu/~murray/amwiki/index.php/Atomic_force_microscope.

[64] R. L. Fagaly, Review of Scientific Instruments **77**, 101101 (2006).

[65] D. Speliotis, *Getting the most from your vibrating sample magnetometer*. .

[66] http://www.nobelprize.org/educational/physics/microscopes/tem/index.html.

[67] L. Reimer and H. Kohl, *Transmission Electron Microscopy: Physics of Image Formation* (Springer, 2008).

[68] http://www.globalsino.com/EM/page4554.html.

[69] *Karl Suss' MA6 Operations Spec*.

[70] http://www.microresist.de/products/negative_photoresists/overview_neg_en.htm.

[71] http://www.microchem.com/#.

[72] http://www.ionbeammilling.com/about_the_ion_milling_process.

[73] D. K. Schroder, *Semiconductor Material And Device Characterization* (John Wiley & Sons, 2006).

[74] D. H. Kwon, K. M. Kim, J. H. Jang, J. M. Jeon, M. H. Lee, G. H. Kim, X. S. Li, G. S. Park, B. Lee, S. Han, M. Kim, and C. S. Hwang, Nat. Nanotechnol. **5**, 148 (2010).

[75] G. S. Park, X. S. Li, D. C. Kim, R. J. Jung, M. J. Lee, and S. Seo, Appl. Phys. Lett. **91**, 222103 (2007).

[76] K. M. Kim, B. J. Choi, and C. S. Hwang, Appl. Phys. Lett. **90**, 242906 (2007).

[77] J. S. Lee, S. B. Lee, S. H. Chang, L. G. Gao, B. S. Kang, M. J. Lee, C. J. Kim, T. W. Noh, and B. Kahng, Phys. Rev. Lett. **105**, 205701 (2010).

[78] J. H. Hur, M. J. Lee, C. B. Lee, Y. B. Kim, and C. J. Kim, Phys. Rev. B **82**, 155321 (2010).

[79] M. J. Rozenberg, M. J. Sanchez, R. Weht, C. Acha, F. Gomez-Marlasca, and P. Levy, *Phys. Rev.* B **81**, 115101 (2010).

[80] M. Quintero, P. Levy, A. G. Leyva, and M. J. Rozenberg, Phys. Rev. Lett. **98**, 116601 (2007).

[81] D. M. Ramo, A. L. Shluger, J. L. Gavartin, and G. Bersuker, Phys. Rev. Lett. **99**, 155504 (2007).

[82] Y. S. Chen, L. P. Chen, G. J. Lian, and G. C. Xiong, J. Appl. Phys. **106**, 023708 (2009).

[83] Y. S. Chen, G. J. Lian, G. C. Xiong, and T. Venkatesan, Appl. Phys. Lett. **98**, 232513 (2011).

[84] R. Brucas, M. Hanson, P. Apell, P. Nordblad, R. Gunnarsson, and B. Hjorvarsson, Phys. Rev. B **81**, 224437 (2010).

[85] H. Yang, S.-H. Yang, and S. S. P. Parkin, Nano Lett. **8**, 340 (2008).

[86] S. H. Chang, J. S. Lee, S. C. Chae, S. B. Lee, C. Liu, B. Kahng, D. W. Kim, and T. W. Noh, Phys. Rev. Lett. **102**, 026801 (2009).

[87] C. Gould, A. Slobodskyy, D. Supp, T. Slobodskyy, P. Grabs, P. Hawrylak, F. Qu, G. Schmidt, and L. W. Molenkamp, Phys. Rev. Lett. **97**, 017202 (2006).

[88] D. G. Austing, S. Tarucha, P. C. Main, M. Henini, S. T. Stoddart, and L. Eaves, Appl. Phys. Lett. **75**, 671 (1999).

[89] S. Das, S. Majumdar, and S. Giri, J. Phys. Chem. C **114**, 6671 (2010).

[90] Y. Meir and N. S. Wingreen, Phys. Rev. Lett. **68**, 2512 (1992).

[91] E. Y. Tsymbal, Nature Mater. **11**, 12 (2012).

[92] I. S. Beloborodov, A. V. Lopatin, V. M. Vinokur, and K. B. Efetov, Rev. Mod. Phys. **79**, 469 (2007).

[93] M. Knobel, W. C. Nunes, L. M. Socolovsky, E. De Biasi, J. M. Vargas, and J. C. Denardin, J. Nanosci. Nanotechnol. **8**, 2836 (2008).

[94] H. Yang, S.-H. Yang, G. Ilnicki, J. Martinek, and S. S. P. Parkin, Phys. Rev. B **83**, 174437 (2011).

[95] A. Kalitsov, A. M. Sahadevan, S. N. Jammalamadaka, G. Kalon, C. S. Bhatia, G. Xiong, and H. Yang, AIP Adv. **1**, 042158 (2011).

[96] H. Silva, H. L. Gomes, Y. G. Pogorelov, P. Stallinga, D. M. de Leeuw, J. P. Araujo, J. B. Sousa, S. C. J. Meskers, G. Kakazei, S. Cardoso, and P. P. Freitas, Appl. Phys. Lett. **94**, 202107 (2009).

[97] C. Yoshida, K. Kinoshita, T. Yamasaki, and Y. Sugiyama, Appl. Phys. Lett. **93**, 042106 (2008).

[98] T. Nagata, M. Haemori, Y. Yamashita, H. Yoshikawa, Y. Iwashita, K. Kobayashi, and T. Chikyow, Appl. Phys. Lett. **97**, 082902 (2010).

[99] M. C. Biesinger, L. W. M. Lau, A. R. Gerson, and R. S. C. Smart, Appl. Surf. Sci. **257**, 887 (2010).

[100] M. R. Alexander, G. E. Thompson, and G. Beamson, Surf. Interface Anal. **29**, 468 (2000).

[101] J. Y. Bae, W. C. Lim, H. J. Kim, T. D. Lee, K. W. Kim, and T. W. Kim, J. Appl. Phys. **99**, 08T316 (2006).

[102] H. Ogasawara, B. Brena, D. Nordlund, M. Nyberg, A. Pelmenschikov, L. G. M. Pettersson, and A. Nilsson, Phys. Rev. Lett. **89**, 276102 (2002).

[103] K. Asami, S. Mitani, H. Fujimori, S. Ohnuma, and T. Masumoto, Surf. Interface Anal. **28**, 250 (1999).

[104] J. Hubbard, Proc. R. Soc. Lond. A **276**, 238 (1963).

[105] M. K. Niranjan, C.-G. Duan, S. S. Jaswal, and E. Y. Tsymbal, Appl. Phys. Lett. **96**, 222504 (2010).

[106] T. Maruyama, Y. Shiota, T. Nozaki, K. Ohta, N. Toda, M. Mizuguchi, A. A. Tulapurkar, T. Shinjo, M. Shiraishi, S. Mizukami, Y. Ando, and Y. Suzuki, Nat. Nanotechnol. **4**, 158 (2009).

[107] S. Zhang, Y. G. Zhao, P. S. Li, J. J. Yang, S. Rizwan, J. X. Zhang, J. Seidel, T. L. Qu, Y. J. Yang, Z. L. Luo, Q. He, T. Zou, Q. P. Chen, J. W. Wang, L. F. Yang, Y. Sun, Y. Z. Wu, X. Xiao, X. F. Jin, J. Huang, C. Gao, X. F. Han, and R. Ramesh, Phys. Rev. Lett. **108**, 137203 (2012).

[108] S. K. R. S. Sankaranarayanan, E. Kaxiras, and S. Ramanathan, Energy Environ. Sci. **2**, 1196 (2009).

[109] S. K. R. S. Sankaranarayanan and S. Ramanathan, J. Phys. Chem. C **114**, 6631 (2010).

[110] S. Parkin, J. Xin, C. Kaiser, A. Panchula, K. Roche, and M. Samant, Proc. IEEE **91**, 661 (2003).

[111] J. P. Velev, P. A. Dowben, E. Y. Tsymbal, S. J. Jenkins, and A. N. Caruso, *Surface Science Reports* **63**, 400 (2008).

[112] H. Yang, S.-H. Yang, and S. Parkin, AIP Advances **2**, 012150 (2012).

[113] P. J. Kelly and R. D. Arnell, Vacuum **56**, 159 (2000).

[114] G. Safran, C. Reinhard, A. P. Ehiasarian, P. B. Barna, L. Szekely, O. Geszti, and P. E. Hovsepian, J. Vac. Sci. Technol A **27**, 174 (2009).

[115] G. M. Choi, K. H. Shin, S. A. Seo, S. O. Kim, W. C. Lim, and T. D. Lee, IEEE Trans. Magn. **45**, 2371 (2009).

[116] M. Sinder, G. Sade, and J. Pelleg, MRS Spring Meeting **529**, 145 (1998).

[117] A. J. Devasahayam, P. J. Sides, and M. H. Kryder, *Journal of Applied Physics* **83**, 7216 (1998).

[118] H. Yang, Stanford University, 2006.

[119] P. W. T. Pong and J. W. F. Egelhoff, Proc. SPIE **6645**, 66451V (2007).

[120] X. Peng, Z. Wang, Y. Lu, B. Lafferty, T. McLaughlin, and M. Ostrowski, Vacuum **84**, 1075 (2010).

[121] Y. M. Lee, J. Hayakawa, S. Ikeda, F. Matsukura, and H. Ohno, Appl. Phys. Lett. **90**, 212507 (2007).

[122] D. W. Abraham, P. L. Trouilloud, and D. C. Worledge, IBM J. Res. Dev. **50**, 55 (2006).

[123] S. Isogami, M. Tsunoda, K. Komagaki, K. Sunaga, Y. Uehara, M. Sato, T. Miyajima, and M. Takahashi, Appl. Phys. Lett. **93** (2008).

[124] V. Harnchana, A. P. Brown, R. M. Brydson, J. P. Harrington, A. T. Hindmarch, C. H. Marrows, and B. J. Hickey, in *EMAG: Electron Microscopy and Analysis Group Conference* (Journal of Physics Conference Series, 2008).

[125] A. K. Petford-Long and A. N. Chiaramonti, Annu. Rev. Mater. Res. **38**, 559 (2008).

[126] J. Kanak, T. Stobiecki, V. Drewello, J. Schmalhorst, and G. Reiss, Physica Status Solidi A **204**, 3942 (2007).

[127] K. Mizunuma, S. Ikeda, H. Sato, M. Yamanouchi, H. D. Gan, K. Miura, H. Yamamoto, J. Hayakawa, F. Matsukura, and H. Ohno, J. Appl. Phys. **109** (2011).

[128] *Discussions with other groups – IBM Spintronics group and Cornell University*.

[129] H. Yang, S.-H. Yang, D.-C. Qi, A. Rusydi, H. Kawai, M. Saeys, T. Leo, D. J. Smith, and S. S. P. Parkin, Phys. Rev. Lett. **106**, 167201 (2011).

[130] M. Chu, Y. Sun, U. Aghoram, and S. E. Thompson, Annu. Rev. Mater. Sci. **39**, 203 (2009).

[131] M. L. Lee, E. A. Fitzgerald, M. T. Bulsara, M. T. Currie, and A. Lochtefeld, J. Appl. Phys. **97**, 011101 (2005).

[132] A. Shimizu, K. Hachimine, N. Ohki, H. Ohta, M. Koguchi, Y. Nonaka, H. Sato, and F. Ootsuka, in *Tech. Dig. - Int. Electron Devices Meet.* , (2001), p. 19.4.1.

[133] K. M. Tan, M. Zhu, W. W. Fang, M. Yang, T. Y. Liow, R. T. P. Lee, K. M. Hoe, C. H. Tung, N. Balasubramanian, G. S. Samudra, and Y. C. Yeo, IEEE Electron Device Lett. **29**, 192 (2008).

[134] X. K. Liu, B. Liu, E. K. F. Low, W. Liu, M. C. Yang, L. S. Tan, K. L. Teo, and Y. C. Yeo, Appl. Phys. Lett. **98**, 183502 (2011).

[135] K. M. Tan, M. C. Yang, T. Y. Liow, R. T. P. Lee, and Y. C. Yeo, IEEE Trans. Electron Devices **56**, 1277 (2009).

[136] J. Park and B. D. Yu, Phys. Rev. B **83**, 144431 (2011).

[137] J. N. Yeo, G. M. Jee, B. D. Yu, and B. C. Choi, J. Korean Phys. Soc. **52**, 1938 (2008).

[138] G. X. Miao, J. Y. Chang, M. J. van Veenhuizen, K. Thiel, M. Seibt, G. Eilers, M. Münzenberg, and J. S. Moodera, Appl. Phys. Lett. **93**, 142511 (2008).

[139] F. Bonell, S. Andrieu, C. Tiusan, F. Montaigne, E. Snoeck, B. Belhadji, L. Calmels, F. Bertran, P. Le Fèvre, and A. Taleb-Ibrahimi, Phys. Rev. B **82**, 092405 (2010).

[140] D. Herranz, F. Bonell, A. Gomez-Ibarlucea, S. Andrieu, F. Montaigne, R. Villar, C. Tiusan, and F. G. Aliev, Appl. Phys. Lett. **96**, 202501 (2010).

[141] E. Rismani, S. K. Sinha, S. Tripathy, H. Yang, and C. S. Bhatia, J. Phys. D: Appl. Phys. **44**, 115502 (2011).

[142] J. Robertson, Tribol. Int. **36**, 405 (2003).

[143] G. M. Pharr, D. L. Callahan, S. D. McAdams, T. Y. Tsui, S. Anders, A. Anders, J. W. Ager, I. G. Brown, C. S. Bhatia, S. R. P. Silva, and J. Robertson, Appl. Phys. Lett. **68**, 779 (1996).

[144] D. A. Shirley, Phys. Rev. B **5**, 4709 (1972).

[145] W. Lu, K. Komvopoulos, and S. Yeh, J. Appl. Phys. **89**, 2422 (2001).

[146] P. W. T. Pong, C. L. Dennis, A. Castillo, A. Chen, and J. W. F. Egelhoff, J. Appl. Phys. **103**, 07A902 (2008).

[147] A. A. Khan, J. Schmalhorst, G. Reiss, G. Eilers, M. Münzenberg, H. Schuhmann, and M. Seibt, Phys. Rev. B **82**, 064416 (2010).

[148] M. C. Munoz, V. R. Velasco, and F. Garcia-Moliner, Prog. Surf. Sci. **26**, 117 (1987).

[149] J. Cerdá, M. A. Van Hove, P. Sautet, and M. Salmeron, Phys. Rev. B **56**, 15885 (1997).

[150] J. Cerdá, A. Yoon, M. A. Van Hove, P. Sautet, M. Salmeron, and G. A. Somorjai, Phys. Rev. B **56**, 15900 (1997).

[151] R. Hoffmann, J. Chem. Phys. **39**, 1397 (1963).

[152] T. Z. Raza, J. I. Cerdá, and H. Raza, J. Appl. Phys. **109**, 023705 (2011).

[153] D. M. Roessler and W. C. Walker, Phys. Rev. **159**, 733 (1967).

[154] M. Acet, H. Zähres, E. F. Wassermann, and W. Pepperhoff, Phys. Rev. B **49**, 6012 (1994).

[155] G. Kresse and J. Furthmüller, Phys. Rev. B **54**, 11169 (1996).

[156] G. Kresse and J. Furthmüller, Comput. Mat. Sci. **6**, 15 (1996).

[157] J. Heyd, G. E. Scuseria, and M. Ernzerhof, J. Chem. Phys. **118**, 8207 (2003).

[158] O. Madelung, U. Rössler, and M. Schulz, in *SpringerMaterials - The Landolt-Börnstein Database* (Springer, 1999), Vol. 41B.

[159] C.-S. Zha, H.-k. Mao, and R. J. Hemley, Proc. Natl Acad. Sci. USA **97**, 13494 (2000).

[160] K. S. Yong, D. M. Otalvaro, I. Duchemin, M. Saeys, and C. Joachim, Phys. Rev. B **77**, 205429 (2008).

[161] C. Zhang, X. G. Zhang, P. S. Krstić, H.-p. Cheng, W. H. Butler, and J. M. MacLaren, Phys. Rev. B **69**, 134406 (2004).

[162] S. A. Wolf, D. D. Awschalom, R. A. Buhrman, J. M. Daughton, S. von Molnár, M. L. Roukes, A. Y. Chtchelkanova, and D. M. Treger, Science **294**, 1488 (2001).

[163] S. Tehrani, J. M. Slaughter, M. Deherrera, B. N. Engel, N. D. Rizzo, J. Salter, M. Durlam, R. W. Dave, J. Janesky, B. Butcher, K. Smith, and G. Grynkewich, Proc. IEEE **91**, 703 (2003).

[164] G. Brammertz, K. Martens, S. Sioncke, A. Delabie, M. Caymax, M. Meuris, and M. Heyns, Appl. Phys. Lett. **91**, 133510 (2007).

[165] K. T. McCarthy, A. F. Hebard, and S. B. Arnason, Phys. Rev. Lett. **90**, 117201 (2003).

[166] S. Zhang, Phys. Rev. Lett. **83**, 640 (1999).

[167] S. T. Chui and L. Hu, Appl. Phys. Lett. **80**, 273 (2002).

[168] Y.-M. Chang, K.-S. Li, H. Huang, M.-J. Tung, S.-Y. Tong, and M.-T. Lin, J. Appl. Phys. **107**, 093904 (2010).

[169] H. Kaiju, S. Fujita, T. Morozumi, and K. Shiiki, J. Appl. Phys. **91**, 7430 (2002).

[170] G. Landry, Y. Dong, J. Du, X. Xiang, and J. Q. Xiao, Appl. Phys. Lett. **78**, 501 (2001).

[171] P. Padhan, P. LeClair, A. Gupta, K. Tsunekawa, and D. D. Djayaprawira, Appl. Phys. Lett. **90**, 142105 (2007).

[172] S. Ingvarsson, M. Arikan, M. Carter, W. Shen, and G. Xiao, Appl. Phys. Lett. **96**, 232506 (2010).

[173] J. C. A. Huang and C. Y. Hsu, J. Appl. Phys. **98**, 064901 (2005).

[174] T. W. Hickmott, J. Appl. Phys. **93**, 3461 (2003).

[175] G. Kalon, Y. J. Shin, V. G. Truong, A. Kalitsov, and H. Yang, Appl. Phys. Lett. **99**, 083109 (2011).

[176] B. A. Ravan, A. A. Shokri, and A. Yazdani, J. Appl. Phys. **109**, 07C734 (2011).

[177] S. Altindal and H. Uslu, J. Appl. Phys. **109**, 074503 (2011).

[178] D. Korucu, S. Altindal, T. S. Mammadov, and S. Ozcelik, J. Optoelectron. Adv. Mater. **11**, 192 (2009).

[179] X. Wu, E. S. Yang, and H. L. Evans, J. Appl. Phys. **68**, 2845 (1990).

[180] W.-C. Chien, Y.-D. Yao, J.-K. Wu, C.-K. Lo, R.-F. Hung, M. D. Lan, and P. Lin, J. Appl. Phys. **105**, 033915 (2009).

[181] K. Narayanapillai, M. Jamali, and H. Yang, Appl. Phys. Lett. **101**, 052401 (2012).

[182] Y. Wang, C. Kin Ping, R. Choi, and B. H. Lee, IEEE Trans. Electron Devices **55**, 2429 (2008).

[183] Y. Wang, K. P. Cheung, R. Choi, and B. H. Lee, IEEE Trans. Electron Devices **55**, 2437 (2008).

[184] D. W. Barlage, J. T. O'Keeffe, J. T. Kavalieros, M. M. Nguyen, and R. S. Chau, IEEE Electron Device Lett. **21**, 454 (2000).

[185] L. H. Sperling, *Introduction to Physical Polymer Science* (Wiley-Interscience, 2005).

[186] T. G. Mezger, *The rheology handbook : for users of rotational and oscillatory rheometers* (Vincentz, Hannover, 2006).

[187] W. C. Chien, T. Y. Peng, L. C. Hsieh, C. K. Lo, and Y. D. Yao, IEEE Trans. Magn. **42**, 2624 (2006).

[188] G. Catalan, Appl. Phys. Lett. **88**, 102902 (2006).

Appendix A: Transport calculation method

A.1 Introduction

The development of the Landauer formula, which links electron transmission probability to current flow, is one of the most important theoretical achievements in the field of quantum transport. By relating the current to the transmission probability, the Landauer formula provides a conceptual framework to study ballistic conductance in atom scale structures which greatly simplifies computations [1]. As a result, the Landauer formula is increasingly being applied to study current flow in a variety of atom scale devices. For example, current flow in Scanning Tunnelling Microscope (STM) , Magnetic Tunnel Junction (MTJ) as well as Giant Magneto-Resistance (GMR) devices have been studied with the Landauer formula [2–5].

This section expounds the methodologies used for the calculations in Chapter 7. First, the motion of a quantum particle in the presence of a square barrier is described to illustrate the tunneling behavior and concept of transmission probability. Thereafter, the Landauer formula for current calculations is explained in detail. Subsequently, the transfer matrix technique [6] and the green function [2] are described which are used to calculate the transmission probability for realistic systems. Finally, the extended Huckel method which is used in the construction of the Hamiltonian matrix is illustrated.

A.2 Quantum Mechanical Tunneling

In classical mechanics, a particle can cross a potential barrier only when its total energy is greater than the height of the potential barrier. However, quantum particles have a finite probability of crossing a potential barrier even when their total energy is less than the height of the potential barrier. This phenomenon of particles overcoming a classically insurmountable barrier is referred to as quantum mechanical tunneling. The tunneling behaviour of electrons leads to the tunneling current which forms the basis of operation for various atom scale devices such as STM and MTJ. In STM, the image of a surface is formed from the tunneling current between the STM tip and the surface when the tip is scanned over the surface. In a TMR device, the change in the tunneling current when the relative magnetization of electrodes is reversed forms the basis of its operation.

Because of its technological importance, various methods have been proposed to calculate the tunneling probability. The transfer matrix technique [7] and the green function technique [2] are two widely used methods which have been employed to study tunneling in various systems. In this thesis, the transfer matrix technique is employed for STM image calculations for CO/Cu(111) and for the Mo_2S_3 surface, while the green function is employed for the calculation of the tunneling current in MTJ.

A.3 Tunneling probability through a square barrier

In this section the analytical solution of a quantum mechanical particle when it encounters a rectangular potential barrier is obtained by solving the Schrodinger equation of the system. The particle wave with unity amplitude encounters the potential barrier of height V_0 and width a at $x = 0$ as shown in Figure A.1. As a result,

a part of the incoming wave is reflected with amplitude r, while the rest is transmitted with amplitude t. The transmission probability for the particle, the ratio of the square of the amplitude of the transmitted wave to the incident wave, is calculated by solving the Schrodinger equation of the system:

$$\left[-\frac{\hbar}{2m}\frac{d^2}{dx^2}+V(x)\right]\Psi(x)=E\Psi(x) \tag{A.1}$$

where $\hbar$ is the reduced Planck's constant, m is mass, E is energy of the particle and $V(x)$ is the barrier potential which is V_0 for $0 \le x \le a$ and 0 for all other values of x. Since the potential within a given region remains constant, the wave function in each region is expressed as a free particle wave:

$$\begin{aligned}
&\psi_L(x) = e^{ik_0x} + re^{-ik_0x}, x<0\\
&\psi_C(x) = B_r e^{ik_1x} + B_l e^{-k_1x}, 0<x<a,\\
&\psi_R(x) = te^{ik_0x}, x>a
\end{aligned} \tag{A.2}$$

where B_l and B_r represent the transmitted and the reflected amplitude at the left barrier. The transmission probability, when the energy is less than the barrier height, $E < V_0$ is given by:

$$T=|t|^2=\frac{1}{1+\dfrac{V_0^{\,2}Sinh^2(k_1a)}{4E(V_0-E)}} \tag{A.3}$$

Thus it is clear from the above expression that there is a finite transmission probability when the particle energy is less than the height of the potential barrier. The transmission probabilities for both the quantum mechanical and classical particles are plotted in Figure A.2. For classical particles, the probability is zero (one) when the barrier height is more (less) than the particle energy. However, in the quantum case there is a finite probability for the particle transmission, even when the particle energy is less than the barrier height. Interestingly when the particle energy is more than the

barrier height, the transmission probability becomes one only for certain particle energies called the resonance energies.

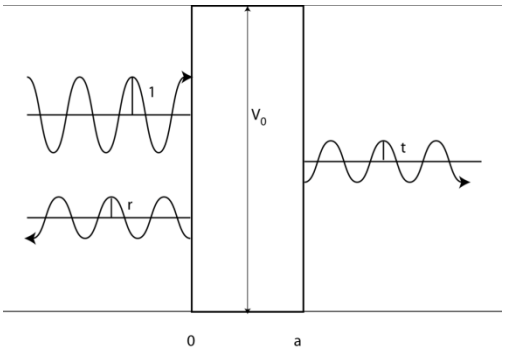

Figure A.1. A particle wave of unit amplitude encounters a potential barrier at X=0 with height V_0 and width a. A part of it is reflected with amplitude $\boldsymbol{r}$ while the rest is transmitted with amplitude $\boldsymbol{t}$.

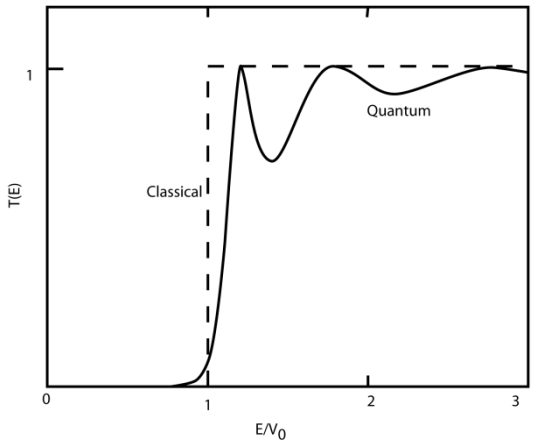

Figure A.2. Transmission probability for a finite potential barrier for $\sqrt{\mathbf{2mV_0a}/\hbar} = \mathbf{7}$. Classical results have been shown by dashed line and quantum mechanical results have been shown by solid line. Adapted from [8].

A.4 Landauer-Buttiker formula for current calculation

The origin of the Landauer formula can be understood by considering the current flow between two reservoirs connected by a thin wire through two leads at their ends, as shown in Figure A.3. When a small bias voltage (V) is applied, the Fermi level of the reservoirs shifts such that E_{f1}-E_{f2} = eV.

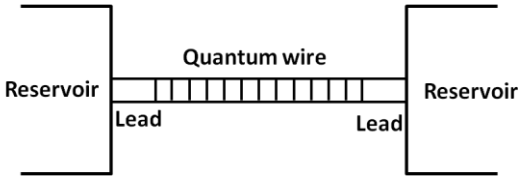

Figure A.3. Schematic diagram of a 1D system used in the derivation of the Landauer formula showing a quantum wire connecting two reservoirs through two leads.

As a result of the potential imbalance, a current flow is established through the wire whose magnitude is proportional to the number of electrons in the given energy window (eV) multiplied by their respective velocity(v). For small bias, the number of electrons participating in the current flow is given by density of states times the difference in the Fermi levels of the two reservoirs. For such a case, the expression for the current becomes:

$$I = e[n_{1D}(E)eV]v(E) \tag{A.4}$$

The velocity $v(E)$ appearing in the above equation can be calculated from the knowledge of the electronic structure of the leads. For that electronic wave packets, which are formed from the superposition of the waves with nearly identical wave vectors, are considered as given below:

$$\psi(x,t) \propto \int_{k-\frac{\Delta k}{2}}^{k+\frac{\Delta k}{2}} c(k)e^{i[kx-\omega t]}\,dk \tag{A.5}$$

Such electronic wave packets travel with group velocity v_g which is given by:

$$v_g = \frac{\partial \omega}{\partial k} \tag{A.6}$$

For the 1d case the group velocity is given by:

$$v_g = \frac{2}{\pi \hbar n_{1D}} \tag{A.7}$$

Putting the above value of the group velocity in Equation A.5, we get the expression for the current:

$$I = \frac{2e^2}{h} V \tag{A.8}$$

In the above expression it is assumed that the wire does not provide any resistance and all the electrons coming from the left reservoir are transmitted to the right reservoir. In practice, however, a part of the electrons are reflected at the interface. To account for that in the current calculation, the current value in the above equation is multiplied by the transmission coefficient $T(E)$ and the current for such a case is given by:

$$I = \frac{2e^2}{h} T(E) V \tag{A.9}$$

The current, when the leads have more than one channel as shown in Figure A.4, can be calculated by summing up the contribution due to each of those channels. It is important to note that a given channel (j) on the right receives an electron from a channel i on the left with a probability T_{ij}. The total current for this case is given by summing up the contribution due to each channel j on the left which, in turn, receives contribution from every channel i on the right, resulting in the double summation as given below:

$$I = \frac{2e^2}{h} \sum_{i,j} T_{ij}\,(E_F)\, V \tag{A.10}$$

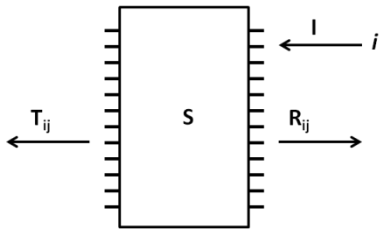

Figure A.4. A multichannel system S. A unit current in channel i is transmitted into j with probability T_{ij} and reflected into channel j with probability R_{ij}. Both indices i and j run from 1 to N. Adapted from [9].

When a finite bias voltage is applied, the energy levels shift as shown in Figure A.5. To account for that, the current I is calculated by integrating in the applied bias range. This gives the following:

$$I(V) = \frac{e}{h}\int_0^{-eV} \sum_{ij} T_{ij}\left(E + E_f\right)dE \tag{A.11}$$

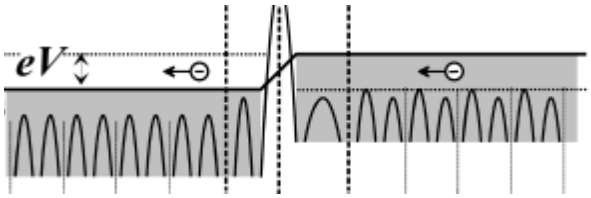

Figure A.5. Shift in the chemical potential of the left and the right lead channels upon the application of a bias voltage V. Adapted from [2].

In the next two sections, methods for the calculation of the transmission probability appearing in the Landauer formula are described in detail.

A.5 Green function approach for the transmission probability

The Green function for a system with Schrodinger equation $H|\psi\rangle = E|\psi\rangle$ is given by:

$$(E - H + i\eta)G(E) = I \tag{A.12}$$

where $G(E)$ is the Green function of the system and η is an infinitesimally small number. For a given system, two Green functions exist, depending on whether a

positive or negative value of η is used in the calculation of the Green function. For positive η, the Green function is termed the retarded Green function (G), while for negative η, the Green function is termed as the advanced Green function $(G^{\dagger})$.

Knowledge of the Green function for a given system allows us to find its response under a constant perturbation $|v\rangle$.

$$H|\psi\rangle = E|\psi\rangle + |v\rangle \tag{A.13}$$

The response to perturbation $|v\rangle$ is:

$$\begin{aligned}(E - H)|\psi\rangle = -|v\rangle \rightarrow \\ |\psi\rangle = -G(E)|v\rangle\end{aligned} \tag{A.14}$$

Thus, from the above equation, it is evident that the wave function of a given system under the influence of a perturbation $|v\rangle$ is given by the Green function of the unperturbed system $G(E)$ multiplied by the perturbation $|v\rangle$. It is also possible to calculate the wave function of an unperturbed system $(|\psi\rangle)$ from the knowledge of the advanced and retarded green function under any perturbation $|v\rangle$.

$$|\psi\rangle = A|v\rangle \tag{A.15}$$

where A is called the spectral function and is defined as:

$$A = i(G - G^{\dagger}) \tag{A.16}$$

This becomes evident when we consider the two solutions of the Schrodinger equation, $|\psi^R\rangle$ and $|\psi^A\rangle$, obtained from the advanced and retarded Green function upon the application of a perturbation $|v\rangle$.

$$|\psi^R\rangle = -G|v\rangle \tag{A.17}$$

$$|\psi^A\rangle = -G^{\dagger}|v\rangle \tag{A.18}$$

By operating $A|v\rangle$ on the Hamiltonian $(E-H)$ we find:

$$(E-H)A|v\rangle = (E-H)(G-G^{\dagger})|v\rangle = (I-I)|v\rangle = 0 \tag{A.19}$$

The real advantage of the Green function method lies in the study of large systems. Such systems can be studied by dividing them into smaller subsystems, resulting in large savings in the computational costs. For example, to study the current flow in a STM tunnel junction or a MTJ, the system is divided into three subsystems: the left periodic part, the defect part, and the right periodic part. The current is then determined from the modified Green function of the defect. The modified Green function takes into account the effect due to the presence of the left and the right periodic part. The origin of the modified green function can be understood by considering the Green function of the whole system.

$$\begin{pmatrix} E-H_1 & -\tau_1 & 0 \\ -\tau_1^{\dagger} & E-H_d & -\tau_2^{\dagger} \\ 0 & -\tau_2 & E-H_2 \end{pmatrix} \begin{pmatrix} G_1 & G_{1d} & G_{12} \\ G_{da} & G_d & G_{d2} \\ G_{21} & G_{2d} & G_2 \end{pmatrix} = \begin{pmatrix} I & 0 & 0 \\ 0 & I & 0 \\ 0 & 0 & I \end{pmatrix} \tag{A.20}$$

where G denotes the full Green's function and G_{ij} denotes the Green's function of its sub-matrices, H_1, H_2 and H_d represents the Hamiltonian of the left periodic part, right periodic part, and the defect, respectively while τ_1 and τ_2 represent the interaction between the left periodic part and the defect, and right periodic part and the defect, respectively.

To find the Green function of the defect, the three equations in the second column are selected:

$$(E - H_1)G_{1d} - \tau_1 G_d = 0 \tag{A.21}$$

$$-\tau_1^\dagger G_{1d} + (E - H_d)G_d - \tau_2^\dagger G_{2d} = I \tag{A.22}$$

$$(E - H_2)G_{2d} - \tau_2 G_d = 0 \tag{A.23}$$

From Equation A.21 and A.23, G_{1d} and G_{2d} are calculated to have the following form:

$$G_{1d} = g_1 \tau_1 G_d \tag{A.24}$$

$$G_{2d} = g_2 \tau_2 G_d \tag{A.25}$$

where g_i's are the green function of the isolated contacts, e.g., $(E - H_i)g_i = I$. Substituting the values of G_{1d} and G_{2d} in Equation A.22 and solving for G_d we obtain:

$$G_d = (E - H_d - \Sigma_1 - \Sigma_2)^{-1} \tag{A.26}$$

where $\Sigma_1 = \tau_1^\dagger g_1 \tau_1$ and $\Sigma_2 = \tau_2^\dagger g_2 \tau_2$ are called the self energies, which take into account the effect of the left and right periodic parts on the defect green function.

The self energies Σ_i appearing in the above equation can be expressed as a sum of the real and imaginary parts. For Σ_1 the values are given by:

$$\Sigma_{H1}(E) = \frac{1}{2}\left[\Sigma_1(E) + \Sigma_1^\dagger(E)\right] \tag{A.27}$$

$$\Gamma_1(E) = i[\Sigma_1(E) - \Sigma_1^\dagger(E)] \tag{A.28}$$

Physically, Σ_H and Γ_1 represents the correction to the Hamiltonian (shift in the energy level) and the broadening of the levels due to the presence of contacts.

Once the values of A_i and Γ_i are known, the transmission probability is calculated from the relation [10]:

$$T(E) = Trace(\Gamma_1 A_2) = Trace(\Gamma_2 A_1) \tag{A.29}$$

References for Appendix

[1] R. Landauer, IBM Journal of Research and Development 32, 306-316 (1988).

[2] J. Cerdá, M. A. Van Hove, P. Sautet, and M. Salmeron, Physical Review B 56, 15885-15899 (1997).

[3] P. Sautet and C. Joachim, Chemical Physics Letters 185, 23-30 (1991).

[4] J. Mathon and A. Umerski, Physical Review B 63, 220403 (2001).

[5] J. Mathon, A. Umerski, and M. Villeret, Physical Review B 55, 14378-14386 (1997).

[6] P. Sautet and C. Joachim, Physical Review B 38, 12238-12247 (1988).

[7] P. Sautet and C. Joachim, Physical Review B 38, 12238 (1988).

[8] D. J. Griffiths, *Introduction to Quantum Mechanics*, 2nd ed. (Benjamin Cummings, 2004).

[9] M. Büttiker, Y. Imry, R. Landauer, and S. Pinhas, Physical Review B 31, 6207-6215 (1985).

[10] S. Datta, *Quantum Transport: Atom to Transistor*, 2nd ed. (Cambridge University Press, 2005).

Appendix B: List of symbols, abbreviations and acronyms

NM- Non-magnetic

FM- Ferromagnet

SC- Superconductor

P- Parallel

AP- Anti-parallel

MR- Magnetoresistance

GMR- Giant magnetoresistance

AMR- Anisotropic magnetoresistance

TMR- Tunneling magnetoresistance

MTJ- Magnetic tunnel junction

MgO- Magnesium oxide

Al_2O_3- Aluminium oxide

IrMn- Iridium manganese

H_c- Coercivity or coercive field

Co- Cobalt

Fe- Iron

Ni- Nickel

B- Boron

Cr- Chromium

Ar- Argon

Au- Gold

Si- Silicon

Ta- Tantalum

CPP- Current perpendicular to plane

RA- resistance area product

HDD- Hard disk drive

MRAM- Magnetic random access memory

TMC- Tunnel magnetocapacitance

RC- resistance capacitance product (time constant)

ReRAM- Resistive random access memory

MBE- Molecular beam Epitaxy

SQUID- Superconducting quantum interference device

SCM- Storage class memory

MPMS- Magnetic property measurement system

CMOS- complementary metal–oxide–semiconductor

SSD- Solid state drive

NAND- Not AND

RAM- Random access memory

DRAM- dynamic random access memory

SRAM- static random access memory

STT- Spin transfer torque

NaOH- Sodium hydroxide

TMAH- Tetramethylammonium hydroxide

SPM- Scanning probe microscope

Pt- Platinum

LSMO- Lanthanum strontium manganite

DOS- Density of states

PZT- Lead zirconate titanate

DLC- Diamond like carbon

MIM- Metal insulator metal

DC- direct current

AC- alternating current

RF- radio frequency

RGA- residual gas analyzer

AFM- Atomic force microscope

RMS- root mean square

AGFM- alternating gradient force magnetometer

TEM- transmission electron microscope

CCD- charge-coupled device

IPA- Isopropanol

MA6- mask aligner

SIMS- secondary ion mass spectrometer

Oe- Oersted

T- Tesla

RS- resistive switching

XPS- X-ray photoelectron spectroscopy